LUDWIG-MAXIMILIANS-UNIVERSITÄT MÜNCHEN

FAKULTÄT FÜR GEOWISSENSCHAFTEN

DEPARTMENT FÜR GEOGRAPHIE

MASTERARBEIT

Umweltsysteme und Nachhaltigkeit
Monitoring, Modellierung und Management

Assessment of the Suitability of PlanetScope SuperDove Imagery for Aquatic Remote Sensing at Lake Junin in Central Peru

Bewertung der Eignung von PlanetScope SuperDove Satelliten Daten für die Aquatische Fernerkundung am Junin-See in Zentralperu

Wissenschaftliche Arbeit zur Erlangung des akademischen Grades Master of Science

Verfasser:
Name: Patrick Ferdinand Klotz
Anschrift: Geisloherweg 24d, 89312 Günzburg
E-Mail: patrick.klotz@web.de

Betreuer:
Prof. Dr. Lukas Lehnert
Mitbetreuung:
Dr. Peter Gege

Datum: 22.01.2024

Acknowledgements

I wish to express my appreciation for the support and guidance provided by Prof. Dr. Lukas Lehnert, my supervisor at the LMU Munich. I extend special thanks to Dr. Peter Gege as my supervisor at the German Aerospace Center. His expertise and encouragement have been instrumental in shaping the direction of my research. Because of him, I am motivated to explore further opportunities in the exciting field of aquatic remote sensing.

Additionally, I would like to acknowledge the insightful contributions from Stefan Plattner and Dr. Ian Somlai Schweiger, who provided invaluable feedback and support every week. Special thanks are also due to Sonja Schmid, my fellow master student, for her assistance at various stages of the project and the associated field campaign.

The opportunity to travel to Peru and collaborate with an experienced team of researchers was truly invaluable, and I am grateful for the unforgettable experience. My gratitude extends to the German Aerospace Center for providing students unique opportunities in the field of remote sensing and environmental monitoring. Finally, I want to thank to our project partners at the *Autoridad Nacional de Agua* in Peru for providing essential equipment and expertise during the field campaign.

Table of Contents

List of Figures

List of Tables

List of Abbreviations

6SV	*Second Simulation of the Sattelite Signal in the Solar Spectrum*
ANA	*Autorida Nacional de Agua*
API	*Application Programming Interface*
BOA	*Bottom of Atmosphere*
BRDF	*Bi-directional Reflectance Distribution Function*
CDOM	*Colored Dissolved Organic Matter*
CZCS	*Coastal Zone Color Scanner*
DEM	*Digital Elevation Model*
DLR	*German Aerospace Center*
DN	*Digital Number*
DSF	*Dark Spectrum Fitting*
FWHM	*Full Width At Halve Maximum*
GIS	*Geographic information system*
GIZ	*German Development Cooperation*
GUI	*Graphical User Interface*
IMARPE	*Instituto del Mar del Perú Laboratory*
IOP	*Inherent Optical Properties*
IWRM	*Integrated Water Resource Management*
LUT	*Look Up Table*
MAE	*Mean Average Error*
MOD1	*Continental Aerosol Model from 6SV*
MOD2	*Maritime Aerosol Model from 6SV*
MODIS	*Moderate Resolution Imaging Spectroradiometer*
MODTRAN	*Moderate Resolution Atmospheric Transmission*
MSI	*Multispectral Instrument*
NAP	*Non Algal Particles*
NDCI	*Normalized Difference Chlorophyll Index*
NDWI	*Normalized Difference Water Index*
NIR	*Near Infrared*
OBRA	*Optimal Band Ratio Analysis*
OCTS	*Ocen Color and Temperature Scanner*
OLI	*Operational Land Imager*
PANTHYR	*Pan- and Tilt Hyperspectral Radiometer*
PICS	*Pseudo Invariate Calibration Site*
RadCalNet	*Radiometric Calibration Network*
RBINS	*Royal Belgian Institue of Natural Sciences*
RGB	*Red Green Blue*
RMSE	*Root Mean Square Error*
ROI	*Region Of Interest*
RRS	*Remote Sensing Reflectance*
SAG	*Servicios Analitico Generales Laboratory*
SNR	*Signal To Noise Ratio*
SRF	*Spectral Response Function*
TOA	*Top of Atmosphere*
TSM	*Total Suspended Matter*
USV	*Unmanned Surface Vehicle*

Abstract

This thesis evaluates the suitability of multispectral PlanetScope SuperDove satellite-data for physics-based bathymetry and determination of chlorophyll-a concentrations for a high-altitude lake in Peru. A field campaign was conducted in June 2023 to obtain in-situ data for regional adaptation of the processing methodology and for validation purposes. The collection and analysis of in-situ measurements is presented, accompanied by an analysis of their uncertainties. A validation dataset for bathymetry was obtained using two different methods for in-situ water depth measurements. From this, a historical data set from a lake bathymetry survey in 2006 was adapted, and an up-to-date validation raster was derived (Mean average error was 0.39 m between raster pixels and in-situ measurements). Chlorophyll-a concentration was determined from water samples by two different laboratories and from inverse modelling of in-situ water spectra in the software WASI. A good agreement was found for water depth above 2 m (mean average error: 0.8 µg/l). Three SuperDove images from consecutive days during the field campaign were investigated regarding image noise, sensitivity to atmospheric correction parametrization and consistency in consecutive overpasses. Results are summarized for two areas of interest in optically deep and shallow water. Here it was shown that the band specific reflectance between images were inconsistent, especially so in optically deep water with up to 45% difference in the derived remote sensing reflectance. Additionally, initialization in the software ACOLITE for atmospheric correction showed high sensitivity to the extent of the provided image scene, which impacted estimated parameters for the atmospheric correction. Here, errors over 10% were observed for all spectral bands. Reflectance spectra from three SuperDove images were compared with in-situ measurements from 21 field stations. Excluding the near-infrared band, the coefficient of determination for a linear regression model was 0.73, 0.91 and 0.91 for the three satellite images. Finally, outcomes from processing SuperDove imagery in WASI fell below the desired threshold for a deep water and shallow water model as water spectra derived from SuperDove imagery were distorted. As a result of the study, SuperDove proved to be unsuitable for determining water depth and chlorophyll-a in Lake Junin.

1. Introduction

Integrated Water Resource Management (IWRM) is a holistic approach aimed at sustainable and equitable utilization of water resources. It involves the coordinated development and management of water, land, and related resources to optimize economic and social welfare while preserving ecosystems. IWRM recognizes the interconnectedness of various water uses, such as agriculture, industry, and domestic consumption, and seeks to balance competing demands through efficient allocation, conservation, and protection of water sources. By considering both quantity and quality aspects, this approach promotes community engagement, stakeholder collaboration, and adaptive strategies to address challenges like climate change and population growth. Ultimately, IWRM strives to ensure the long-term availability and resilience of water resources for present and future generations. However, communities that are essential to include in IWRM often do not have the necessary resources or institutional support to adequately participate in decision making processes (Apostolaki et al., 2019). Ideally, the inclusion of farmers and pastoralists, who are directly affected by water quality and water availability, plays a central role in the holistic decision making (German et al., 2007; Berkes, 2010).

In 2009, the Peruvian government committed to an IWRM approach with their implementation of a *Water Resource Law* (Ley de Recursos Hidricos). As a result, the *National Water Authority* (ANA, Autoridad Nacional de Agua) was founded, and regional and local watershed management decisions were operated on a much smaller scale than before. As Peru is a country severely affected by climate change, this new delegation of resource management in light of changing watersheds was a necessary step towards adaptation and mitigation strategies (Correa et al., 2016; Mark et al., 2017; Popovici et al., 2021). For three districts in the Peruvian Caylloma Province, it has been shown that community-level management responsibilities are often not feasible. Instead, resources should focus on strengthening governmental institutions on a regional scale (Popovici et al. 2021). To support the Peruvian institutions in their management and decision making, the *ProGIRH* project was launched in 2022. This multisectoral collaboration funded by the *German Development Cooperation* (GIZ, Deutsche Gesellschaft für internationale Zusammenarbeit) aims to improve the integrated and climate sensitive management of water resources in the Mantaro river basin in Peru (Giz, 2023). Within this project, the *German Aerospace Center* (DLR, Deutsches Zentrum für Luft- und Raumfahrt) was asked to provide technical guidance and capacity building for the regional project partners at the ANA. The overlying objective of this is to establish a self-dependent and locally managed monitoring of water quality and availability. More precisely, remote sensing of inland water bodies and determination of water quality parameters should be improved, validated, and lastly taught, so that a long-term monitoring system could eventually be operated independently.

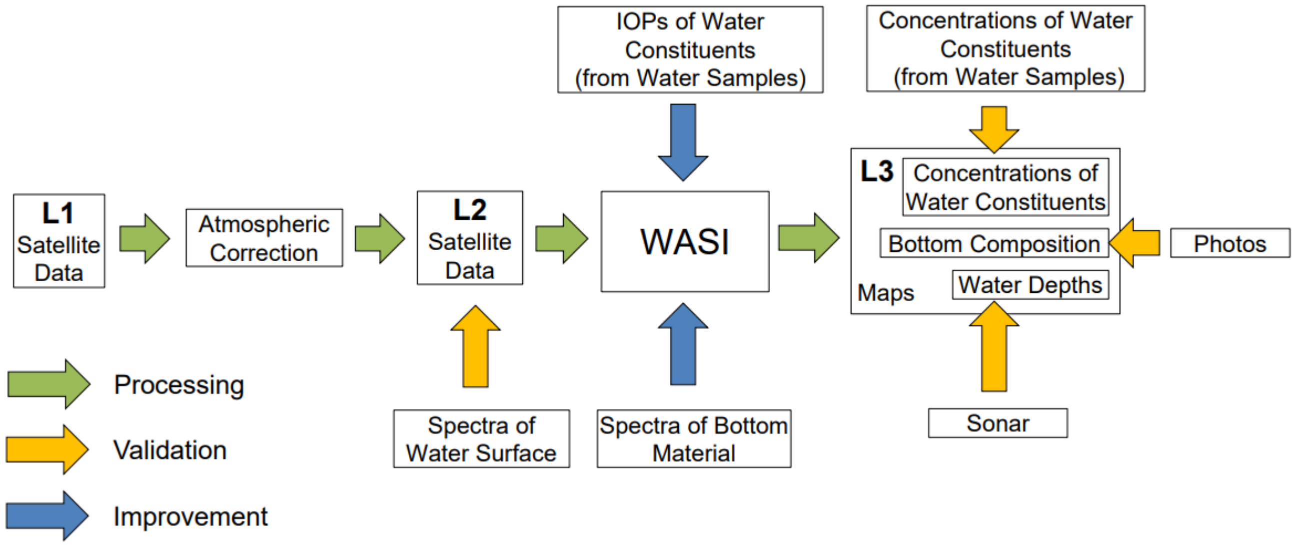

Figure 1: Process chain from Level-1 Data to Level-3 Data. Improvements can be achieved through regional parametrization in WASI. Level-2 and Level-3 Data can be validated from field-measurements.

1.1. Thesis Objective and Structure

The objective of this master's thesis is to evaluate the suitability of PlanetScope SuperDove imagery for physics-based bathymetry and determination of water quality parameters. The potential for aquatic remote sensing from SuperDoves imagery, promising high temporal and spatial resolution, remains largely unexplored. This research thus seeks to establish a comprehensive methodology, incorporating this image product in a physics-based model, to derive accurate and reliable water depth and chlorophyll-a concentrations. These parameters can be validated from in-situ measurement, and systematic collection of in-situ measurements at two test sites in Peru were carried out as part of this thesis. Field measurements are accompanied by an analysis of their uncertainties with the aim to improve and validate the determined parameters from the model. Figure 1 illustrates the process chain to determine water depth and chlorophyll-a concentration from satellite imagery: Based on the output parameters from satellite derived reflectance, an assessment of the uncertainties between in-situ data and determined parameters from the model can be made. However, this step is not included in the analysis as SuperDove imagery was rejected as a high-quality image input. This is due to anomalous spectral signatures and inconsistency between individual images and high image noise. Instead, the challenges that led to the assessment as an unsuitable data product are outlined and discussed accordingly.

Throughout the assessment, three distinct levels of data are considered and defined as follows:

- **Level-1 Data:** This comprises calibrated multispectral or hyperspectral satellite imagery projected to a coordinate reference system, provided as top of the atmosphere (TOA) radiance or reflectance.
- **Level-2 Data:** The calibrated image data is further processed to bottom of the atmosphere (BOA) reflectance, accounting for atmospheric contributions. Validation is performed by comparing the corrected imagery with field observations of water surface spectra, ensuring accuracy before subsequent processing steps.
- **Level-3 Data:** Parameters, such as water constituent concentrations, lakebed composition, and water depth, are derived through inverse modelling of reflectance of Level-2 data in the software WASI. The validity of these parameters can be confirmed through field observations taken at a corresponding location.

After a short introduction of the test sites in the following subchapter, the thesis is structured as follows: *Chapter 2* provides an overview of the challenges in aquatic remote sensing. These include sensor calibration, atmosphere, sun-glint, spectral ambiguities, and the bottom signal. *Chapter 3* outlines the material and methods used in this study. *Chapter 3.1* describes field measurements and their subsequent processing to obtain validation data. These include the spectra of the water surface, water depth and chlorophyll-a concentration. A spectral database for common bottom types was constructed in a second master thesis written as part of this project and associated field campaign (Schmid 2024). Technical details and recent applications of SuperDove imagery in aquatic remote sensing are outlined in *Chapter 3.2*. For atmospheric correction, an algorithm implemented in the software ACOLITE is used and described in *Chapter 3.3*. Characteristics based on which the data was evaluate is described in *Chapter 3.4*. Results are presented in *Chapter 4* and include validation data and its uncertainties, the image noise in a SuperDove scene and consistency of derived reflectance from parametrization for the atmospheric correction as well as between consecutive overpasses. Further, challenges for the initialization of the physics-based model with SuperDove imagery are presented. These challenges ultimately lead to the rejection of the data for the determination of Level-3 parameters. *Chapter 5* then discusses the results and outlines results from successful initialization with Sentinel-2B data.

1.2. Test sites

A field campaign was conducted between the 15th and 30th June 2023. Figure 2 shows the two sites that were visited by researchers from the DLR, accompanied by partners from the ANA, during this time:

A) Lake Junin (*Lago Cuspicocha* or *Lago Junín*)

B) Lake Lasuntay (*Laguna Lasuntay*)

Lake Junin is the second largest lake in Peru, located in a high plateau on the eastern slope of the Andes Mountains in central Peru, at 4080 m above sea level. It is surrounded by grassy plains used extensively for pastoral agriculture. Lake Lasuntay is located at 4663 m above sea level in the central mountain range of the Andes, 200 km east of the capital city Lima. Both lakes are within the Mantaro river basin where 35% of Peru´s electricity is generated from hydroelectric power stations. The basin is strongly affected by extreme weather, changing precipitation trends and an increase in water demand and thus became the project area of particular interest within ProGIRH (Zubieta et al., 2017).

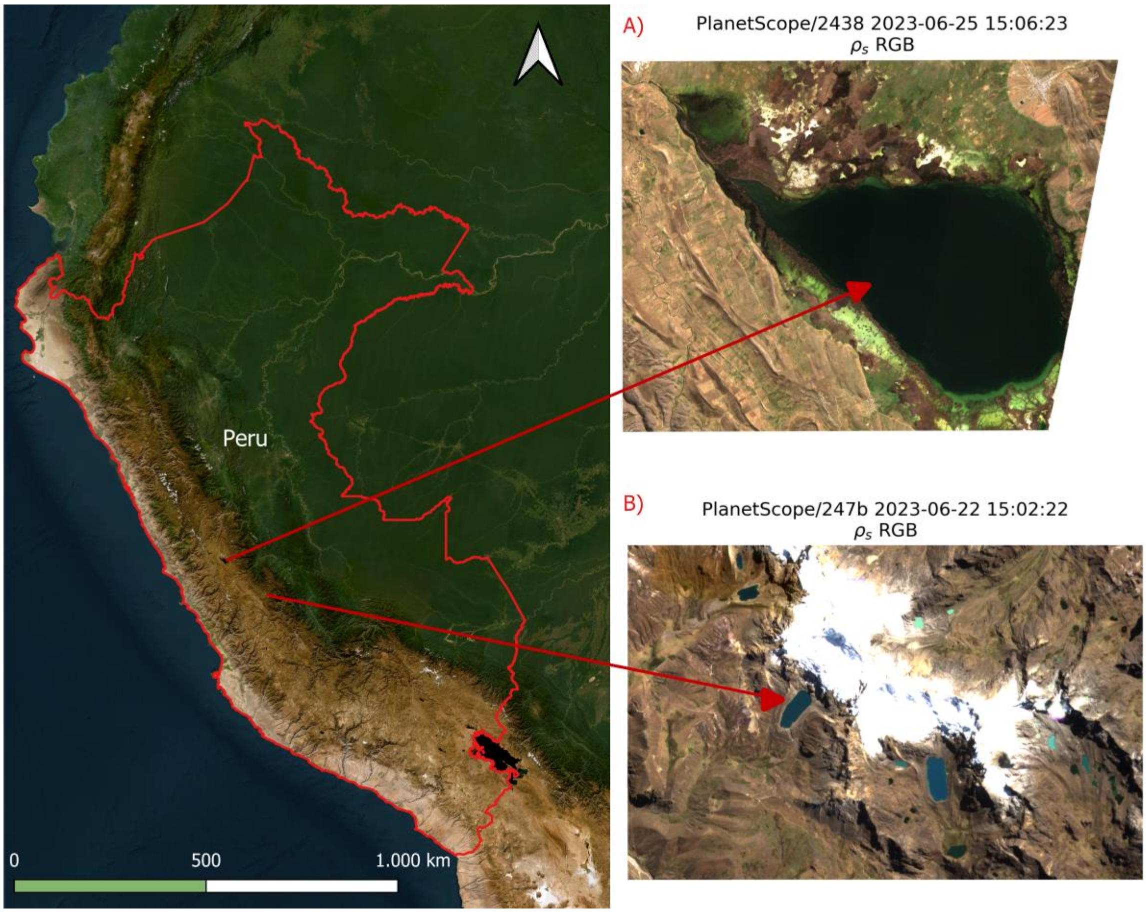

Figure 2: Map of Peru and High-Resolution Images of Test sites.
A) Lake Junin - B) Lake Lasuntay and the Huaytapallana glacier. Left image is ESRI base map imagery in QGIS, right images are RGB composites of surface reflectance from PlanetScope SuperDoves.

1.2.1. Lake Junin

Lake Junin, also known as Lago Chinchaycocha, is a high-altitude lake located in the Junin department in central Peru. It is the largest lake entirely within the country and holds cultural and ecological significance and is considered a Ramsar Wetland of International Importance (Romero-Mariscal et al., 2023). It has an estimated volume of 556 million m³ and an area of 175 km² for the main water body. Lake Junin is surrounded by a diverse ecosystem, including wetlands and high Andean grasslands, providing habitat for various bird species and serving as a crucial stopover for migratory birds (Dinesen et al., 2019). The lake also plays a vital role in the region's hydrology and is the source of fresh water for the nearby communities and their livestock. However, it faces environmental challenges such as pollution and water quality issues, highlighting the importance of conservation efforts (Custodio et al., 2019; Rodbell et al., 2014).

Lake Junin is the origin of the Mantaro river which provides water to large agricultural areas in the Mantaro Valley, thus having a great impact on agricultural production for Lima. Runoff is controlled by the Upamayo dam in the northwest managed by the ANA.

Figure 3: Drone shot of Lake Junin in North-West direction towards the village San Pedro de Pari. This community provided access to the lake during the field campaign and locals aided in the navigation through the extensive reed belts.

The main waterbody and the dam are connected through a channel which the main tributaries, the Colorado and San Juan rivers, feed into. Depending on water availability, this can create the unique situation where the stream flow is reversed and water is flowing into the lake from the channel, carrying sediments and water constituents into the main water body. Accessing the lake is difficult due to the surrounding wetlands, broad reed belts on the south shore and generally limited infrastructure. Figure 3 shows a view of the lake from a drone image acquired during the field campaign. The small community of San Pedro de Pari is visible on the shore. From there, the local community welcomed and assisted researchers from the DLR and partners from the ANA in the field campaign and shared their knowledge and experience with the lake and its changing dynamics. Figure 4 shows a picture of one of two boats from which field measurements were taken during the campaign, provided by the local communities.

Figure 4: Research boat during the field campaign in the shallow parts of Lake Junin. Researchers from the DLR, project partners from ANA and local guides on board. Glacial peak in the background at over 5.700m

1.2.2. Lake Lasuntay

With over 1600km² covered by ice, Peru is the country with the largest area of tropical glaciers Since the recession of these glaciers from the 19th century onwards, a large amount of glacial lakes have formed between moraines, ice dams and valleys due to the ongoing ice melt (Veettil and Kamp, 2019). The newest glacial lake inventory identified over 4550 glacial lakes in Peru, 373 of those located around the Huaytapallana glacier in the central Andean mountain range (Wood et al., 2021). During the field campaign in June 2023, validation data was collected for lake Lasuntay, directly south of the Huaytapallana glacier. The lake can be reached from the city of Huancayo through a long stretch of mountainous road only with the permission of the local communities as the glacier has deep spiritual significance for the indigenous people of this area. Huancayo relies on both surface and groundwater sources for its water supply, with the Shullcas River, a tributary to the Mantaro river, serving as the primary source for the city's human water consumption. The river's average flow during peak times reaches 5 cubic meters per second, dropping to 1.5 cubic meters per second during dry periods. The main runoff contributions come from Lasuntay and lake Cuspicocha (Loayza Ramos, 2017). The latter is only accessible through a long hike, which made accessing it during the field campaign impossible due to limited access hours. Figure 5 shows Lake Lasuntay from the south end looking toward the glacier and Figure 6 shows the water level on a gauge at the southern end of the lake. During the campaign, water levels were high and parts of a road along the western shore of the lake were flooded.

Figure 5: View of the Huaytapallana glacier and researchers on a small dinghy. This mobile boat was provided by the ANA in Huancayo. Small glacial avalanches occurred numerous times during the field campaign.

Figure 6: Lake Lasuntay with view of the Huaytapallana glacier. Water level on a gauge in the foreground. Photo taken from a small embankment where runoff to the Shullcas river originates.

2. Challenges of Aquatic Remote Sensing

Remote sensing is a discipline that entails the acquisition of information about Earth's surface and atmosphere using sensors onboard aerial or satellite platforms. Central to its principles is the measurement and interpretation of electromagnetic radiation interactions with materials. These sensors capture data across distinct spectral bands, enabling the generation of multispectral or hyperspectral imagery with band specific information. Fundamental to remote sensing is the analysis of this data to extract meaningful information pertaining to land cover, environmental dynamics, and human activities (Astha Gautam and Naina Mehta, 2015; Melesse et al., 2007). Figure 7 illustrates the relationship between a sun illuminated water surface and the electromagnetic signal that is received by a satellite sensor.

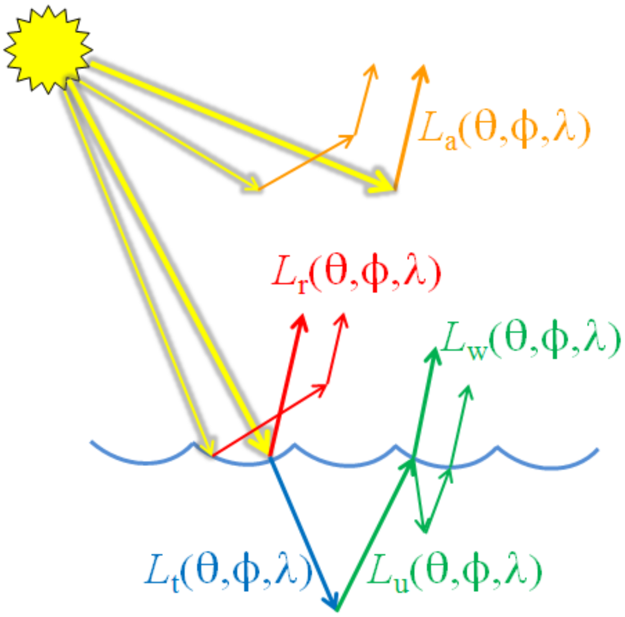

Figure 7: Contributions to the total upwelling radiance above the sea surface. Figure from the Ocean Optics Webbook by Mobley (Ocean Optics, 2024)

A passive sensor system viewing a land surface measures spectral radiance (in watts per square meter per steradian W m^{-2} nm^{-1} sr^{-1}) that includes contributions from the atmosphere and the surface. When viewing water, this signal is extended by the contribution of radiance originating from within the water column. The top of atmosphere (TOA) signal measured by a satellite sensor can therefore be described as:

$$L_u^{TOA} = L_a + L_r + (L_w * t_A)$$

Where L_u^{TOA} is the total upwelling radiance at the TOA, L_a is the atmospheric path radiance, L_r is the surface reflected radiance and L_w is the water leaving radiance after absorption and scattering in the water column and t_A is the atmospheric transmission. This originates from the radiance that is transmitted through the surface into the water body L_t (see blue arrows in Figure 7). L_r can further be divided into components from sky glint, sun glint and reflection from whitecaps on the water surface. A sensor cannot distinguish between the individual contributions of these components, presenting several challenges for aquatic remote sensing (Dörnhöfer and Oppelt, 2016).

2.1. Sensor Calibration

Radiometric calibration of a sensor aims to establish a relationship between the digital number (DN) that is measured by a satellite sensor and the actual radiance emitted from the Earth´s surface and the atmosphere. Some typical methods for radiometric calibration include the following:

1. Laboratory Calibration: Prior to launch, satellite instruments are calibrated in a laboratory. This includes relative radiometric calibration where inconsistencies in detector responses are corrected and absolute radiometric calibration which established a relationship between the DN and physical qualities like spectral radiance (Li et al., 2023).
2. Onboard-Calibration: Specially designed calibration devices mounted on the space-born platform allow for frequent and accurate correction of the calibration coefficients (Song et al., 2022).
3. Cross-Calibration: This method involves comparing the signal of a satellite sensor to that of an established and well-calibrated sensor on a different platform. This helps transfer calibration from one sensor to another while maintaining consistency between the platforms. However, this is usually limited to common spectral bands (Helder et al., 2020).
4. Vicarious Calibration: Ground-based spectral measurements of a well-known test site are directly used to compare ground-truth data to the satellite to then derive correction factors (Czapla-Myers et al., 2015).

No sensors are specifically designed for monitoring inland water bodies. Consequently, their radiometric calibration was derived for land applications, potentially leading to uncertainties when used for aquatic remote. Accuracy requirements for dark targets such as water are greater as the signal originating from the water leaving radiance may be less than 10% of the total signal measured by a space-born sensor at the TOA (Groom et al., 2019).

2.2. Atmosphere

Atmospheric correction in remote sensing is a critical preprocessing step aimed at mitigating the impact of atmospheric contributions on measurements from a sensor, with the goal of accurate retrieval of surface reflectance or radiance information. Key aspects in atmospheric correction include the characterization and removal of atmospheric effects such as the path radiance, composed of Rayleigh and aerosol scattering, as well as water vapor and ozone absorption. All of this impacts the at sensor signal and introduce distortions in remotely sensed data when not accounted for (Ilori et al., 2019). Uncertainties in atmospheric correction arise from challenges in accurately approximating these parameters, particularly in regions with dynamic atmospheric conditions or limited ancillary data. Additionally, inaccuracies in sensor calibration, imprecise knowledge of surface properties, and the presence of clouds may further complicate atmospheric correction methods. Addressing these uncertainties is crucial for obtaining reliable and meaningful data, necessary for robust subsequent analyses and applications (Feng et al., 2018).

Commonly employed methods for atmospheric correction involve radiative transfer models, empirical algorithms, or a combination of both, with the former simulating the interactions between electromagnetic radiation and atmospheric components. For aquatic applications, adjacency effects from the surrounding land, especially vegetation or bright soil, also effect the signal measured for a water pixel at the TOA. Radiance, as a variable directly measured by a sensor, is also not directly representative of surface properties as it will always include the atmospheric contributions. For most remote sensing applications, the radiance reflectance is preferred, either as the TOA reflectance or as the surface reflectance. The latter is defined as the ratio of the radiance leaving a target to the amount of irradiance striking a target (Mobley, 1999). Disregarding the adjacency effect, the TOA reflectance ρ_t, can be simplified with the wavelength (λ) dependent term:

$$\rho_t(\lambda) = t * \rho_w(\lambda) + [\rho_r(\lambda) + \rho_a(\lambda) + \rho_{ar}(\lambda)]$$

Where t is the diffuse transmittance and ρ_w the reflectance at the water surface. ρ_r is the reflectance from scattering by air molecules (Rayleigh scattering) in the absence of aerosols, and ρ_a is the reflectance from scattering by aerosols in the absence of air. ρ_{ar} is the radiance from Rayleigh-aerosol multiple scattering, accounting for the interaction between molecular and aerosol scattering (Pahlevan et al., 2021). The three components in brackets can be computed together, referred to as the path reflectance. The goal of atmospheric correction is thus to retrieve ρ_w from the equation above by the estimation of the path reflectance and the diffuse transmittance. While the Rayleigh scattering could be predicted a priori as it follows a generally consistent pattern, aerosols are highly variable and need to be approximated accurately (Gordon and Wang, 1994). For absolute correction, where atmospheric parameters are estimated for a defined spatial and temporal extent, information on the aerosol concentrations are usually obtained from look up tables (LUT) derived from robust and tested radiative transfer models like MODTRAN (Moderate resolution atmospheric transmission) or 6SV (Second Simulation of the Satellite Signal in the Solar Spectrum) (Basith et al., 2019; Schläpfer et al., 2018; Berk et al., 2014; Shi and Xiao, 2019, 2019).

While atmospheric correction methods for application at the open ocean are carried out adequately, correction methods for inland water bodies are still subject to large uncertainties, limiting the accurate analysis of water quality parameters (IOCCG 2010). As correction algorithms specifically developed for water focus on open ocean and less optically complex water, remote sensing analyses of inland water bodies have often relied on methods designed for land applications (Wang et al., 2019). For inland waters, it was shown that the performance of atmospheric correction methods was a function of the water type and optical properties and generally showed large uncertainties across sites and studies (Pan et al., 2022; Pereira-Sandoval et al., 2019; Palmer et al., 2015; Renosh et al., 2020). However, the robustness of atmospheric correction is especially important for multi-temporal studies and long term monitoring applications as images and derived parameters need to be comparable (Caballero and Stumpf, 2020).

2.3. Sun Glint

Often considered as part of the atmospheric correction process, surface reflection at the air-water interface poses another challenge in aquatic remote sensing and the equation for the TOA reflectance may be extended by including sun glint as the reflectance of the direct solar beam ρ_g (Gordon and Wang, 1994). Sun glint occurs when the water surface is oriented so that the sun is directly reflected towards a sensor, therefore depending on the viewing angle of the instrument and the sun and wave position. Radiance measured by a sensor can have a large component of specular reflection from sun glint, making the removal of those effects essential for the information retrieval of benthic features, water constituents or for bathymetry (Kay et al., 2009; Gabr et al., 2020). The radiance reflectance measured above the water surface is the sum of the glint, or surface reflection, and the contribution from the water column. The latter is referred to as the remote sensing reflectance (R_{rs}):

$$R_{rs} = \frac{L_w(\lambda)}{E_d(\lambda)}$$

With R_{rs} as the ratio of the water leaving radiance L_w to the downwelling radiance E_d at given wavelength λ. As R_{rs} is widely used for water color interpretation the correction of the surface reflection is necessary for avoiding large uncertainties (Mobley, 1999).

In principle, methods to remove sun glint from a satellite image determine the contribution of glint to the total radiance and then subtract that from the at sensor signal. For open ocean, this can be done statistically on a large scale through a model of the sea surface that consider wind speed, wave state as well as sun and sensor position. Based on this information, the orientation of the sea surface and the amount of glint that is received by the sensor can be predicted and moderate glint can be corrected (Wang and Bailey, 2001). For some sensors optimized for ocean color (e.g. CZCS, OCTS, SeaWiFS) direct sun glint is largely avoided by pointing the sensors viewing direction away from the sun. However, correction methods for residual glint still need to be considered and no such sensors are designed for inland lake monitoring (Curtis et al., 2016).

For a more spatially resolved approach, the assumption of a negligible signal in the near infrared (NIR) for an optically deep part of the waterbody is frequently used. It is presumed that any signal after atmospheric correction is due to glint at the water surface and the relationship between the radiance contribution from glint and the NIR can be applied to the entire scene (Hedley et al., 2005). As the reflectance of water exhibits minimal wavelength dependency, the intensities of the glint signal at visible and NIR wavelengths will show similar variations. Consequently, the NIR signal can serve as an indicator of the level of glint at visible wavelengths. It must be noted that his assumption is however not valid for turbid or shallow water, where the signal in the NIR relates to benthic properties or constituent concentrations in the water column and is therefore often not negligible.

Contributions to the at sensor radiance under no-glint conditions are largely due to atmospheric scattering, while the water leaving radiance remains the same under glint and no glint scenarios. When an image is affected by glint, the percentage of the received signal from the water surface decreases while the total reflected radiance measured at the sensor increases. Distinguishing the water leaving radiance from the atmospheric contribution therefore demands a high signal to noise ratio. For severely glint affected scenes, sensor saturation can make the retrieval of the water leaving radiance impossible (Kay et al., 2009).

2.4. Water constituents and Spectral Ambiguities

Inherent optical properties (IOP) of water constituents are another challenging variable in aquatic remote sensing. IOP are optical properties independent of illumination and are referred to as specific IOPS when normalized to a concentration or a value at a given wavelength (Gege and Dekker, 2020). IOP include scattering, backscattering, and absorption coefficients of Phytoplankton, Colored Dissolved Organic Matter (CDOM) and Non-Algal Particles (NAP) within the water column (Yang et al., 2022). The concentration of these particles directly influences the water leaving radiance and, consequently, the measured reflectance from a satellite sensor. Further, the different compositions of particles may lead to a similar spectrum and reflectance values at the same wavelength. The relationship between IOP and the measured reflectance can be approximated as follows:

$$R_{rs} = \frac{L_w}{E_d} = f \frac{b_{btot}}{a_{tot} + b_{btot}}$$

where b_{btot} is the total backscattering coefficient (in m^{-1}) for water, a_{tot} is the total absorption coefficient (in m^{-1}) for water, and f is a proportionality factor (sr^{-1}) (Gordon and Wang, 1994; Gordon et al., 1975). The total coefficients are a sum of the IOPs of pure water, Phytoplankton, CDOM and NAP:

$$a_{tot} = a_w + a_{phy} + a_{CDOM} + a_{NAP}$$
$$b_{btot} = b_{bw} + b_{bphy} + b_{bCDOM} + b_{bNAP}$$

For the absorption of phytoplankton a_{phy} another challenge must be noted due to different absorption coefficients for naturally occurring species. Thus, only the sum of the species-specific absorption coefficients and their concentration accurately describes a_{phy} for a respective water column. Figure 8 shows the specific absorptions coefficients of phytoplankton species that generally provided best results for inverse modelling with WASI for water spectra from both in-situ measurements and satellite imagery at Lake Junin. The transmission of light under water is greatly altered by the light absorbed by phytoplankton and the specific absorption m^2/mg essentially indicates the amount of absorbed energy per unit mass and unit area. It therefore considers both the geometric cross section and mass of the material. Therefore, the composition of total chlorophyll-a in water is dependent on the main type of phytoplankton or a function of the composition of different types and their concentration (Brewin et al., 2019). However, turbid or CDOM rich waters may also be confused with chlorophyll rich waters as both can cause higher reflectance in the visible green wavelength, while potentially decreasing reflectance in the blue bands. (Warren et al., 2021).

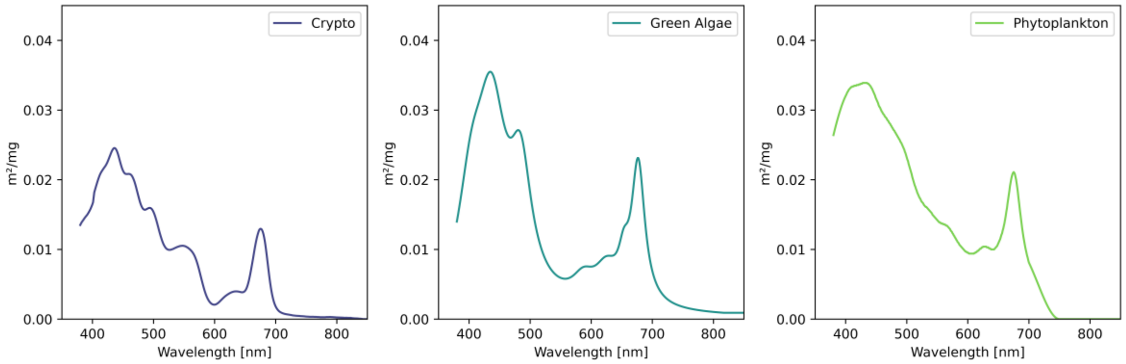

Figure 8: Wavelength dependent specific absorption of different phytoplankton species. Chlorophyll-a concentration from all three species can be set as a parameter in WASI

Examples of those spectral ambiguities due to different concentrations of water constituents and the accurate knowledge of the IOP from the composition within the water column are plentiful. Additionally, while this knowledge is essential for validation and further developments of algorithms for remote sensing applications, accurate in-situ measurements are a challenge in itself (Leymarie et al., 2010). The study by Defoin-Platel and Chami (2007) quantified challenges in watercolor analysis by investigating the ambiguity problem in coastal waters. Synthetic data representing real-world conditions was created to study the ambiguity issue and their research found a high ambiguity rate of around 90% in R_{rs} spectra. Further, the impact of ambiguities on inverse modeling was explored, revealing that the minimum error is related to the dispersion of plausible solutions. To minimize errors in Level-3 parameter derivation from satellite imagery with WASI, it is important to minimize unknown parameters in inverse modelling. In the example of different absorption coefficients for phytoplankton species in Figure 8, this can be done iteratively to first figure out the most likely dominant species, and then fitting only this species along other desired parameters like CDOM and NAP (Defoin-Platel and Chami, 2007; Niroumand-Jadidi and Bovolo, 2021).

2.5. Bottom Reflectance

The ambiguity problem is further amplified in optically shallow waters. Here, the reflectance is influenced by the bottom composition of the water body, namely the substrate and the benthos. Consequently, the depth and clarity of the water column and the distance the light travels until it reaches the bottom surface likewise impacts the reflectance through attenuation and backscattering (Hubert Loisel et al.; Loisel et al., 2013). Figure 9 shows the bottom reflectance of three bottom types that were measured at two different sites: Sand and silt from the sea floor of the Baltic Sea (Schnalzger, 2017) and green macrophytes from Lake Constance in Germany (Pinnel 2005). Similarities in the spectral shape between sand and silt can be seen with a local minimum at around 700 nm for sand and 680 nm for silt. Much larger adjustments must be considered when the lake bottom is overgrown with macrophytes as their albedo is more distinct. Errors for water quality estimations would therefore be larger for lakes with macrophytes when assuming a constant albedo than for water bodies where sand or silt is the common bottom substrate (Lyzenga et al., 2006).

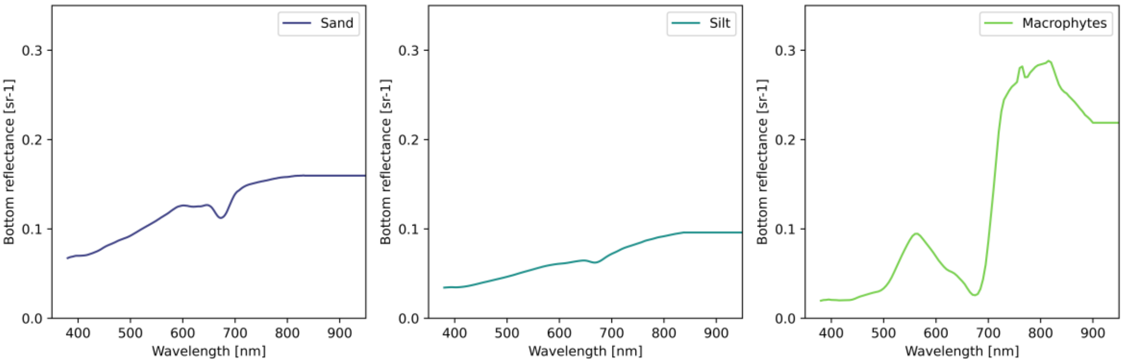

Figure 9: Reflectance of sand, silt and macrophytes. All three bottom types can be set as a parameter in WASI

Additionally, measuring bottom reflectance for regional optimization is not straight forward either. Figure 10 shows a selection of bottom substrates from Lake Junin collected during the field campaign. While their optical properties can be measured accurately with a field spectrometer, their composition and layering on the actual lake surface, which ultimately contributes to the measured at-sensor signal cannot be completely maintained after extraction. Underwater video footage has shown the unmixing of sediment layers during extraction of bottom material revealing darker heavier material than the top layer.

Figure 10: Bottom substrate from four in-situ points at Lake Junin. The sediments were extracted with an Ekmann-Birge sampler, stored in a wet container, and measured on land with a field spectrometer.

3. Materials and Methods

This chapter outlines the methods and techniques that were employed to create a validation dataset for water depth and chlorophyll-a concentration, and to establish a best practice workflow for the processing of satellite data. Ultimately, these environmental variables were to be determined through inverse modelling of the remote sensing reflectance using the software WASI. In addition, the SuperDove imagery from the PlanetScope constellation is outlined and recent applications of the data product for aquatic remote sensing are introduced.

3.1. WASI

In this study, the software WASI is used for the physics-based determination of Level-3 parameters. The software was developed to simulate and analyse spectral measurements above the water surface from both in-situ measurements and satellite images (Gege, 2014). Inverse modelling of a measurement involves iteratively determining unknown model parameters by calculating a simulated spectrum with initial parameter values and comparing it to the measurement using a weighted residual. Fit parameters need to be chosen and initialized carefully to ensure successful determination of the desired variables. Model initialization can also be adapted for specific regional applications by adjusting bottom albedo and IOPs in the database (Manuel et al., 2020). Both a deep water and a shallow water model are available, with 21 and 28 possible fit parameters respectively. When the shallow water model is used, the areal fraction of the bottom substrate and the water depth are additionally included. Gege 2014 provides a detailed overview of fit parameters and best practices for parameter selection and model initialization. For image data, both an artificial intelligence (AI) module (WASI-AI) and the physics-based inversion for each pixel (WASI-2D) are implemented in the software. Good results have been achieved with WASI-2D for the determination of water depth and water constituent concentrations (Niroumand-Jadidi et al. 2021, 2020; Manuel et al. 2020; Dörnhöfer et al. 2016). As computation times for high resolution images at large water bodies like Lake Junin are substantial, the recently developed WASI-AI was chosen to process Level-2 imagery after model initialization. For this, representative spectra within an AOI were selected in the image and the model parameters were adjusted to achieve a good initial fit between the simulated spectrum and the satellite derived spectrum. Training points are then selected in the image or a defined area and processed with the physics-based inversion to train the artificial intelligence. Based on this training data, the entire image is processed by predicting the set fit parameters and maps for the fitted components are created. Additionally, accuracy statistics for the agreement between WASI-AI and WASI-2D for the number of selected validation pixels are provided.

3.2. Field Measurements

In-situ data was collected at Lake Lasuntay and Lake Junin to fulfil the validation and optimization tasks illustrated in Figure 1. The measurements, either taken from land, boat or in shallow waters wearing waders are listed in Table 1. In total, 86 field stations points were covered. 25 of those at Lake Lasuntay, with 12 water stations and 13 stations on the shore. At Lake Junin, 49 in-situ stations were recorded, with 25 water stations and 24 on the western shore in the inundation zones.

Table 1: Overview of field measurements

Parameter	Equipment	Description
Remote sensing reflectance	Spectrometer	Reflectance spectra of different targets
Albedo of wet and dry bottom substrates		
Water Depth	Steel tape Measure	Water depth at fixed stations and along transects
	Echo Sounder	
	Fish finder sonar	
Secchi disk depth	Secchi Disk	Water clarity and turbidity
Chlorophyll-a concentration	Laboratory	Chlorophyll-a concentration at fixed stations
Photo documentation above water	Camera	Photos of targets and measurement set up
	Camera with fisheye lens	Photos of sky and water surface
	Drone	High resolution imagery of water surface
Photo documentation below water	Insta 360	Image and video captures of bottom substrate
GPS location	Campaign Smartphone	Coordinates of in-situ station

3.2.1. Spectrometer measurements

Field measurements for an object's reflectance were carried out with a handheld spectrometer configured to a 1 nm resolution for a wavelength range from 200 to 1100 nm. This constitutes as the validation data of the satellite derived R_{rs} and for parameter modelling from in-situ data with a high spectral resolution. Measurements for a single target (either water, sediment, macrophytes or land surface) included a reference measurement of a spectralon panel and the target itself under unchanged illumination conditions, as well as a measurement of the dark current (see Figure 11). Integration time of the spectrometer was adjusted to the light conditions and the reference panel so that the maximum signal had DN values between 30000 and 50000. Measurements were quality checked on the spot and if either the signal was too low or was saturated the measurement was redone.

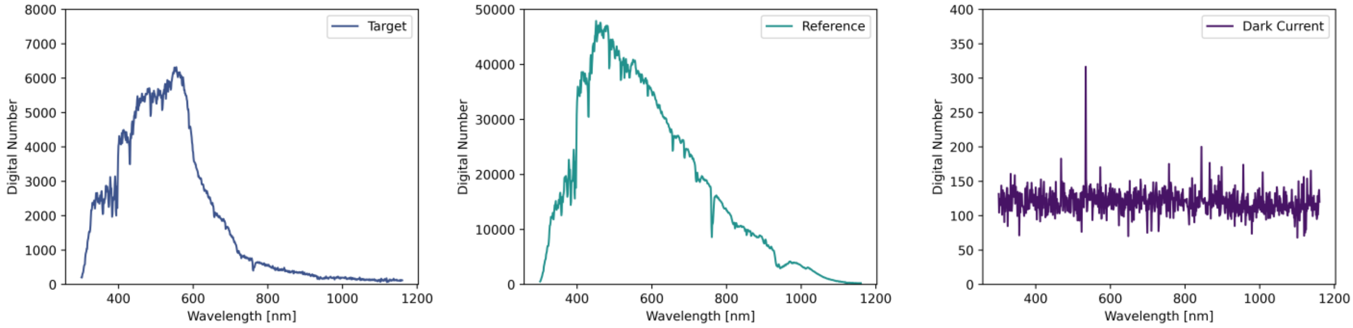

Figure 11: Example of measurements for target object (S_{target}), reference panel ($S_{reference}$) and dark current (S_{dark}). Taken from field measurement point JU_21 above optically deep water.

The three individual measurements were assigned to the corresponding field validation point and the reflectance ρ was calculated from the three components and the reflective properties of the spectralon as follows:

$$\rho = (S_{target} - S_{dark}) * \frac{Reflectance_{Spectralon}}{S_{reference} - S_{dark}}$$

The reflectance of the spectralon was previously measured in a lab with a Perkin-Elmer Lambda 1050 spectrophotometer for wavelengths between 300 and 1000 nm. On the first campaign day, only a single spectrum was logged as the average from 30 individual measurements. For subsequent days, the 30 individual measurements in rapid succession were saved, and outliers were removed based on the median absolute deviation. Then, the average reflectance was derived from all valid measurements. For water, R_{rs} can be derived from ρ by division through pi and subtraction of the surface reflection, which was derived in WASI. For this, reflectance spectra were modelled by fitting a simulated spectrum to the in-situ data from which the wavelength dependent surface reflection at the air-water interface was calculated (Gege, 2004) These are finally subtracted from the original radiance reflectance to retrieve R_{rs}. Figure 12 shows an overview of the water reflectance measurements. Higher reflectance is usually indicative of shallow water and a corresponding bottom signal, as can be seen for stations JU_01 to JU_04 in the plot below:

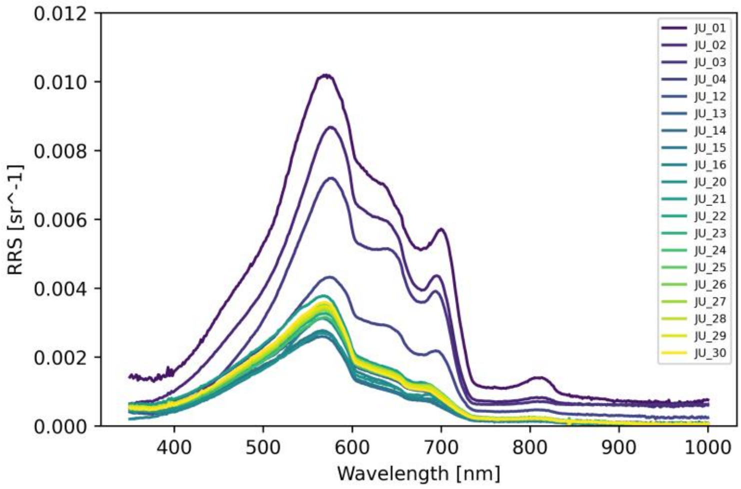

Figure 12: Remote sensing reflectance during field campaign for Lake Junin.

Sediments at water stations were collected by an Ekmann-Birge grab sampler (see Figure 13) and were stored in small plastic containers for measurement on land since measuring time on the boat was limited. On two days where no boat was available, measurements of common surfaces in the shallow regions at the southern shore were acquired to collect a regional spectral data base (Schmid, 2024).

Figure 13: Ekman-Birge sampler and extracted bottom substrate at Lake Junin. Equipment provided by the ANA Huancayo

3.2.2. Validation Parameters

The relevant Level-3 parameters that can be derived from the physics based inverse modelling in WASI, and for which validation data could be collected, are water depth, chlorophyll-a concentration, and the reflective properties of bottom substrate.

Water depth was measured in one out of three ways:

(1) Through a steel measuring tape with a heavy weight at the bottom. Depth was collected to the best possible efforts of the researcher trying to minimize tape drift and depth reading due to the wave state of the water surface.

(2) Through an echo-sounder with a dual beam sonar with 15-degree swath width, directly sending point specific water depth to an application on a smart device. This measurement was then logged manually in the field protocol.

(3) Through a remotely operated boat with an on-board echo-sounder for depth measurements and a flight controller for geolocation and navigation. Here after referred to as USV (Unmanned Surface Vehicle, see Figure 14).

Figure 14: Unmanned surface vehicle at Lake Lasuntay, Peru.

The USV can be used in different operating modes: Manual remote control, an automatic path mode through mission control as well as a route maintaining mode to ensure a course in a straight line. Here, the on-board GPS continuously corrects the path for waters current and wind drift based on the position. Bathymetry data was collected on all three field campaign days at Lasuntay. On the 19th of June and 21st of June, the boat was driving in automatic mode following a pre-set pattern of long paths in south to north direction towards the glacier with a 20-meter space in between each line. These two days covered most of the lake. On the 22nd of June, the USV was controlled manually to precisely measure water depth right up to the water line on the southern part of the lake. Time and safety reasons did not allow similar measurements on the north, west or eastern shore as they were too hard to reach due steep side slopes. Given that the preprogrammed paths for the automatic mission control were based on google earth satellite imagery, an adequate pattern for the high waterline at the point of the field campaign was also not available. Ideally, orthorectified drone imagery integrated into the mission control software could be used to plan the routes for most efficient and precise data collection.

Figure 15: Drone in starting position at Lake Junin. The drone was retrofitted with a foam frame to allow landing in water.

At lake Junin, water depths with the USV were collected opportunistically during measurement points on the first day and whenever time allowed on the second day. The main purpose of the USV at lake Junin was to log depth along the transects to derive a depth profile of the lake. For this, the USV mainly followed the path of the two research boats in the route maintaining mode. In total, three long stretches of continuous measurements were recorded, with distances of 1.42 km, 3.91 km, and 1.33 km respectively.

Additionally, a historical dataset of water depth from a technical report on bathymetry for Lake Junin from the CESEL engineering office was available. Measurements for almost 6000 points were available as the total elevation above sea level (Lazaro and Serpa, 2006; Cesel, 2022). These however only included points in the main water body and a shallow inundation zone in the northwest. The shallow water areas and inundation zones between the main reed belt on the southern shore that were accessible were not included in the study. A manual shoreline around the reed belts was then digitized based on high resolution satellite imagery. Points were interpolated within this delimitation and the water depth was calculated by subtracting the reference elevation from the geodetic control stations at the Upamayo dam.

From the boat, a Secchi Disk attached to the steel tape was lowered into the water. Secchi depth is a commonly used method to estimate water clarity and refers to the depth at which the black and white circular disk becomes invisible when lowered into the water. The visibility of the disk is influenced by the scattering and absorption of light in the water column. Secchi depth serves as an indicator of water transparency, with greater depths indicating clearer water (Alikas and Kratzer, 2017). This measurement is helpful for determining areas of the lake with optically shallow or deep water and consequently the necessary model selection in WASI.

Chlorophyll-a concentration was derived from water samples at selected field points, often overlapping with established monitoring points from the ANA. Responsibilities for water sample collection and transport to two laboratories in Lima was carried out by representatives from the ANA in Huancayo. As ANA has previously worked with the *Servicios Analiticos Generales* (SAG) laboratory, their results were compared with a second analysis from the *Instituto del Mar del Perú* (IMARPE). Details regarding their measuring principles and experiment setup are not available. Due to the limited capacity of containers and adequate cooling and transport logistics, water samples were collected at only 3 points at Lake Lasuntay and 16 points at Lake Junin. Chlorophyl-a concentrations were further derived from inverse modelling of the in-situ spectrometer measurements in WASI. The spectra were fitted for one dominant phytoplankton species (*C[1-5]*), CDOM (*C_X*) and its absorption exponent (*S*), NAP (*C_Y*) and parameters for the fraction of sky radiance (*g_dd*, *g_dsr*, *g_dsa*). Based on the derived concentrations from in-situ modelling and laboratory analysis, results from processing satellite images after model initialization in WASI could be assessed.

Finally, rigorous photo documentation ensured good traceability of the measurements and the environmental conditions. Each water measurement was accompanied by a photo of the water surface, a photo of the sky, a drone overflight (see setup in Figure 15), and an underwater video of the lake bottom. Measurements of substrate, vegetation or soil were also documented so that each measurement has a corresponding image of the target object.

Figure 16: Measurement of the spectralon reference panel. Photo taken in the shallow water areas at the south-western shore at Lake Junin.

3.3. SuperDove Instrument

As stated in the introduction to this thesis, the proposed workflow from Level-1 satellite data to Level-3 information about water constituents and water depth was evaluated with PlanetScope SuperDove imagery. This chapter provides an overview of the technical details, image availability, calibration, and recent applications of this novel data product. To avoid confusion regarding the specific product, the naming conventions are shortly laid out hereafter: PlanetLabs is a private Earth imaging company that specializes in providing satellite imagery and data. PlanetScope, operated by PlanetLabs, is a constellation of over 430 small satellites with three generations of sensors. The newest generation of sensors is referred to as the SuperDove Instrument and has the earliest imagery available from March 2020 (PlanetScope 2024). A study by Niroumand-Jadidi et al. (2020) has shown great potential for bathymetry and retrieval of total suspended matter (TSM) through physic-based inversion with WASI-2D from a previous generation of instruments in the PlanetScope constellation. This led to the assumption that the same workflow could also be applied successfully to SuperDove imagery. Consequently, this investigation solely focuses on the newest sensors as the old one generation is being systematically replaced by the new SuperDove instrument.

3.3.1. Technical Specifications

SuperDoves are equipped with an eight-band frame imager with a butcher block optical filter and eight spectral bands flying in sun-synchronous orbit at 475km height and a 98° orbit inclination. The design is based on the 3U+ CubeSat form factor carrying various processors and sensor for in-flight controls as well as communication with the ground stations (Gutierrez Ahumada et al., 2021; Poursanidis et al., 2019). Nadir ground sample distance varies between 3.7 meters to 4.2 meters depending on the altitude of the surface. The added *Coastal Blue, Green I*, *Yellow* and *Red-Edge* bands improved spectral resolution and added on to the four RGB + NIR bands of previous generations. This also means that they now share central wavelength with six Sentinel-2 MSI bands (see Table 2).

Table 2: Overview of SuperDove Spectral Bands. The shared bands with Sentinel-2B MSI are shaded in grey.

Band Number	Band Name	Central Wavelength (FWHM)
1	Coastal Blue	443 nm (20)
2	Blue	490 nm (50)
3	Green I	531 nm (36)
4	Green	565 nm (36)
5	Yellow	610 nm (20)
6	Red	665 nm (31)
7	Red Edge	705 nm (15)
8	NIR	865 nm (40)

Figure 17 shows the relative spectral response function (SRF) of the eight SuperDove bands, their central wavelength, and the full width at half maximum (FWHM). Variations in the SRF characterize the sensitivity of the spectral bands over a given wavelength range (Trishchenko et al., 2002). SuperDove satellites are launched to orbit in groups, referred to as flocks. The information on the spectral response is available through PlanetLabs, it is however not specific to individual sensors or a specific flock. Despite shared central wavelengths in the six bands, different relative sensitivity to the radiation of a certain wavelength and the band width itself sensors may introduce biases in the received signal between sensors (Gonsamo and Chen, 2013). While little information is available for unit specific SRF, Planet Labs states a consistent spectral performance across SuperDoves and a good alignment between measured SRF and designed SRF (Kington and Collison, 2022).

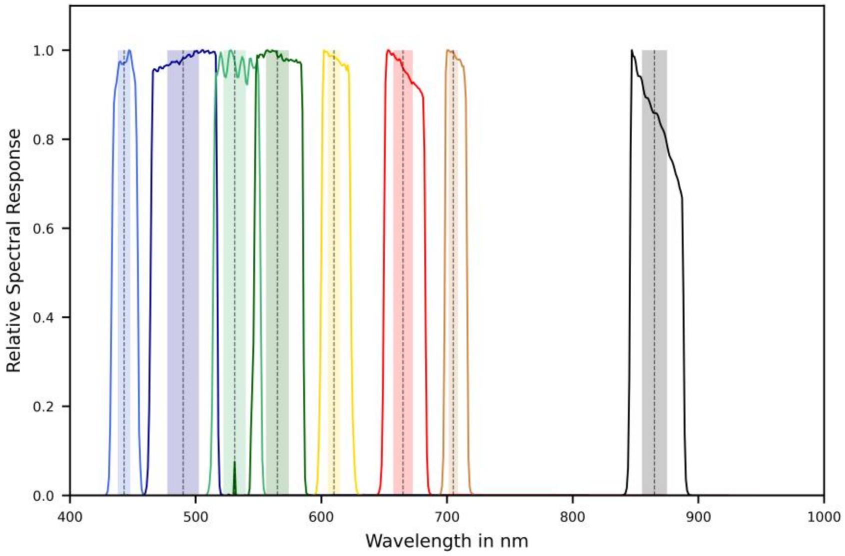

Figure 17: Relative spectral response functions for SuperDove. The central wavelengths are marked by dotted line and fwhm is shaded around this wavelength.

3.3.2. Data Availability and Data Selection

A major advantage of operating a constellation of small satellites is the temporal resolution of the image acquisition. With an image capture capacity of 200 million km² per day this means daily global coverage of all land surfaces within the minimum and maximum latitude coverage. In comparison, conventional multispectral sensors on board the Landsat or Sentinel platforms have significantly longer revisit times, with 16 days for the OLI-2 instrument on Landsat 9 and 10 days for the MSI instrument onboard Sentinel-2A or Senintel-2B. In regions with frequent cloud cover, this may lead to several overpasses without a usable image for the given application. In dynamic systems this will ultimately lead to loss of information and greatly reduce the operational monitoring potential.

Data from all PlanetScope generations can be either accessed through the Planet Explorer website or through the Planet API (Planet 2023) . As this is a commercial operation, imagery is not freely available and requires a registered account and an associated API key to download data. Imagery products are available as either a *Basic Scene* or *Ortho Scene*. *Basic Scenes* are not orthorectified and not projected to a cartographic projection and specifically designed for experienced users. *Ortho Scenes* are orthorectified and resampled to a three-meter sampling interval and are available as either the surface reflectance product or as a TOA radiance product. Figure 18 shows an overview of the time overpasses for all available image products from January to August 2023 obtained by an API search for a bounding box within Lake Junin. In total, 216 scenes from 88 unique SuperDove instrument acquired imagery. The average cloud cover was 42% for the entire tile that included the lake. All overpasses occurred between 09:00am and 10:30am local time (14:00pm to 15:30pm UTC). According to residents, cloud cover over the main water body usually dissipates later in the day, so the acquisition time severely limits useable scenes even from a constellation with daily revisit times.

For the analysis at hand, images were downloaded as a composite of multiple strips from one SuperDove as an *Ortho TOA radiance* product. Occasionally, scenes that would cover the selected area in the Planet Explorer could be stitched together from multiple SuperDoves from the same flock. However, calibration differences between individual satellites or changing light or viewing conditions may impact the consistency of the data for the scene and make the attribution of uncertainties difficult. While in most cases, where different sensor could be stitched together, the overpasses occurred within a few minutes, single sensor data was still preferred even if that meant a loss of spatial coverage on a given day.

For the preliminary suitability assessment of SuperDove imagery, three scenes closest to the field measurements were further investigated. These are images from the 24th, 25th and 26th of

June 2023, whereas validation data for water spectra were collected on the 26th, 27th and 28th of June 2023. Scenes on the same days as the in-situ measurements are available from multiple SuperDoves, the heavy cloud cover until early noon unfortunately however made these scenes inadequate. Therefore, validation of R_{rs} around an in-situ point are always subject to errors due to changes in the water column and atmosphere. Nonetheless, conditions during the week of the available images and the field measurements were stable and therefore still suitable for an initial comparison.

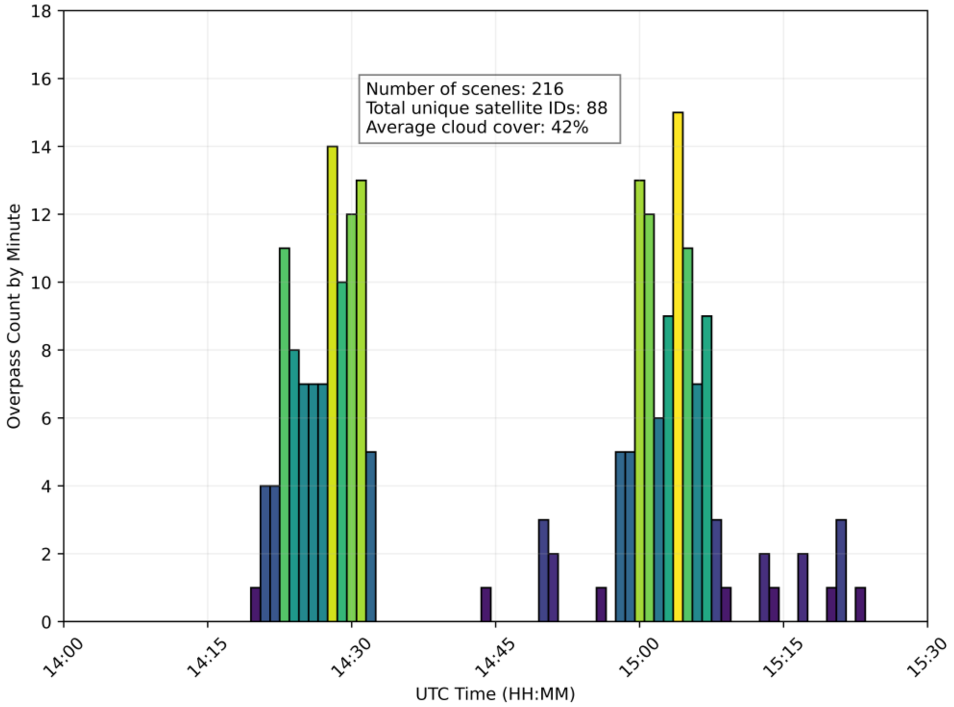

Figure 18: Time of SuperDove overpasses over lake Junin derived from the PlanetScope API and image metadata.

Figure 19 illustrates the benefit of multiple satellites in a larger constellation for earth observation purposes. From August 2022 to August 2023 the highest quality scene from visual inspection of the RGB surface reflectance composite for lake Junin is shown for each month. These were selected based on cloud coverage, visible glint effects on the water surface and noticeable sensor artifacts in the RGB previews from the Planet Explorer. For the winter months in the southern hemisphere, high quality images were available for most days. In February 2023, only one image was largely free of cloud cover and additionally showed sensor artifacts in the scene. However, even without further processing an interesting development in the water body can be observed, as a large sediment plume is entering the lake from the channel leading towards the dam. This plume is still observable 10 days later, although thinned and dispersed further into the lake.

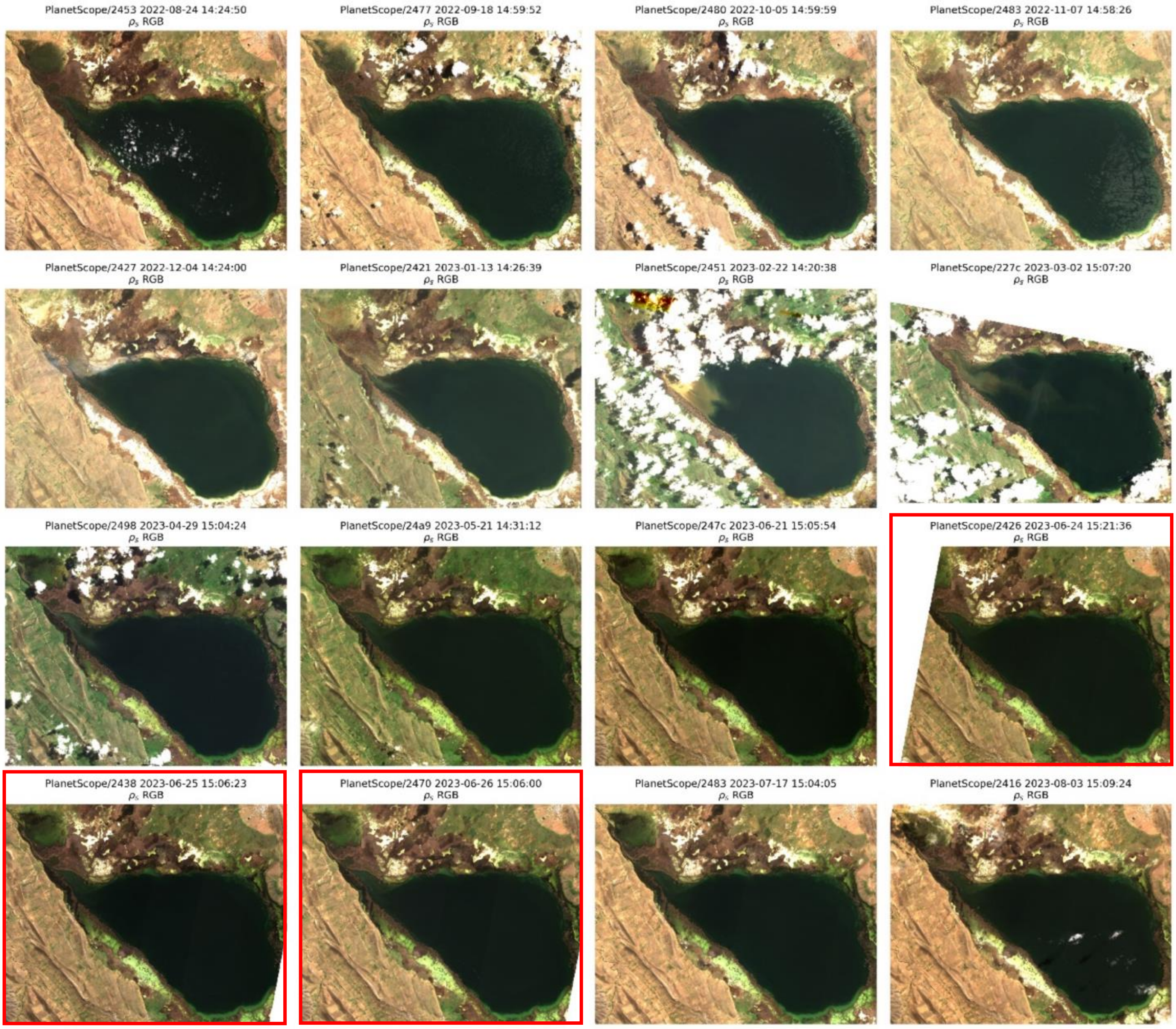

Figure 19: Monthly SuperDove Image from August 2022 to August 2023 as surface reflectance RGBs. Additionally, scenes from June that are analyzed in this thesis are included in the overview and marked by the red border.

3.3.3. Calibration

Calibration, sensor noise, bandwidth and slight differences in spectral response may lead to offsets in even the closest temporal matchups between sensos. For most remote sensing applications, changes in surface conditions therefore need to be distinguished from those due to sensor variations. Comparing imagery from diverse platforms poses challenges due to factors like calibration, spectral response function, atmospheric correction, and viewing or sun-zenith angle (Tu et al., 2022). Correction methods have been devised and applied to medium-resolution Landsat and Sentinel-2 data to address these challenges. For instance, through calculating temporally resolved calibration coefficients and solar irradiance estimates which are used to convert radiance to top-of-atmosphere reflectance, followed by correction for atmospheric and Bi-directional Reflectance Distribution Function (BRDF) effects. Lastly, spectral response function differences between sensors are compensated and the data from different sensors is made comparable. However, implementing these approaches systematically and reliably becomes challenging for large satellite constellations, particularly those lacking continuous onboard calibration (Huang and Roy, 2021; Helder et al., 2020; Roy et al., 2021; Roy et al., 2016).

According to PlanetLabs, SuperDoves go through a rigorous calibration process on the ground and, once in orbit, enter a commission phase where an initial on-orbit calibration is performed (Collison et al. 2022). These adjustments are generally small and further calibration is performed every six months based on the entire image data acquired during that time. While previous generations relied on well-known calibration sites, SuperDoves can directly be cross-calibrated to Sentinel-2 in the six matching bands for every temporal and spatial crossover. The *Green I* and *Yellow* band are additionally calibrated based on the TOA reflectance from the two closest Sentinel-2 bands. For the six months calibration time, each crossover between Sentinel-2 and a SuperDove within two hours is systematically retrieved. To combat biases and to include a full range of reflectance values this is done globally. All land surfaces are divided into a tiled grid where each tile is equally likely to be searched for crossovers. Scenes with a cloud cover over ten percent are filtered out and the maximum number of detected crossovers is set to 20.000. This dataset is subsequently divided into a group for the calibration update and a validation subset. The TOA reflectance for each crossover pair is resampled to a 20-meter grid with corresponding pixels from a SuperDove and Sentinel-2. The correction for the calibration coefficients is then determined by a linear fit of the joint mode between crossover pairs, since it is less sensitive to outliers caused by changing environments within the crossover period (Gollison et al. 2022). Figure shows the scatterplots for this method for a SuperDove with ID

2408 and the calculated calibration coefficients from the linear model from all Sentinel-2 matchups.

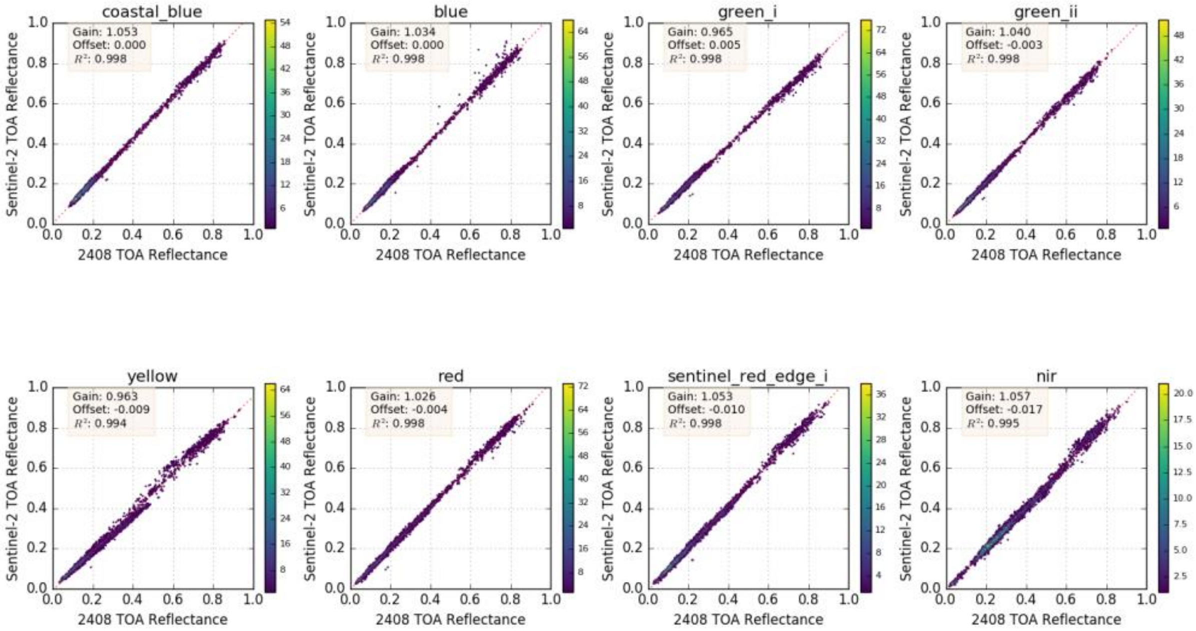

Figure 20: Comparison between SuperDove 2408 and Sentinel-2. Scatterplots for all match ups found during a 6-month calibration period (Gollison et al. 2022).

Planet Labs also states absolute radiometric uncertainties for the *Blue* band (7.5%), *Green II* band (3%), *Red* band (4.6%) and the NIR band (8%) (Saunier and Cocevar, 2022). A report on the assessment of radiometric calibration investigates these uncertainties via two methods:

1. RadCalNet Method
2. PICS Method

In the first method, RadCalNet (Bouvet et al., 2019) provided TOA reflectance is convoluted to the SuperDove spectral band passes, creating a simulated SuperDove reference data set. SuperDove imagery over a 30 m RadCalNet site are adjusted to the viewing geometry of the test site through the MODIS Albedo / BRDF product (MCD43) to derive corrected TOA reflectance from a satellite and the percent difference between the reference data and the adjusted SuperDove imagery is calculated.

The second method uses Sentinel-2 TOA data as a calibration reference over a pseudo-invariant calibration site (PICS) by transforming Sentinel-2 spectra to a simulated SuperDove spectra and calculating the percent difference as done in the first method. Both methods showed that the radiometric calibration error of SuperDove data was in line with the product specifications of a reflectance error within 5%, suggesting good consistency across the constellation.

3.3.4. State of the art research for aquatic applications

Remote sensing with traditional sensors onboard the Landsat and Sentinel platforms has been the preferred method for inland water bodies due to its consistency, radiometric quality, and spatial resolution with well-established calibration and validation and extensive research. While older generations from the PlanetScope constellation have been tested and evaluated in a wide range of remote sensing applications, literature on SuperDove imagery for aquatic applications remains sparse, especially regarding their suitability in a subsequent physics-based modelling approach.

In an empirical study, Sunar et al. (2023) have investigated the accuracy of water constituent retrieval with SuperDove and Sentinel-2 imagery using linear and exponential regression models for the Gulf of Izmir. For this, band combinations were explored to find the best performing model with 11 in-situ measurements for chlorophyll-a, turbidity, TSM and Secchi depth. Except for Secchi depth, Sentinel-2 data showed a higher accuracy score for the best fit model. Model accuracy was however only tested for five validation samples after thematic mapping of the satellite data based on the selected model equation and band combination. The thematic maps appeared to be smoother and more spatially resolved for the SuperDove scene, yet more prone to errors than the Sentinel-2 maps. The authors note that Sentinel-2 has proven to be sufficient for their application, with a higher spectral resolution and more dedicated bands for water quality measurements as the main advantage. However, SuperDove data may be more suited for the eastern part of the region where higher spatial and temporal resolution may help better understand the dynamics of pollutant entry (Sunar et al., 2023).

SuperDove bathymetry was explored by Collin et al. (2023) using a neural network and lidar data for water depth validation. The best model was determined by investigating the performance of either (1) all eight bands, (2) only the RGB + NIR bands identical with previous generations, and (3) the RGB + NIR in addition to each novel band. Out of those six total combinations, all eight bands as a model input into the neural network showed the best results for two of the three test sites, with the RGB + NIR + *Yellow* band selection being favored for the third. Model accuracy was validated with 30 test pixels for each site and the best performing model was used to map water depth for the entire scene extent. The accuracy statistics for all matchups are shown in Table 3. The greatest model gains from the novel bands were attributed to the *Coastal Blue* and *Yellow* band, highlighting improvement for bathymetry in clear waters through the *Coastal Blue* band and the improved CDOM information through the *Yellow* band. The authors remark good potential in SuperDove data for bathymetry and expect further improvements through more refined neural networks. The biggest uncertainties were attributed to the maximum water depth and the time between satellite and lidar data acquisition. For the latter, moving sand banks likely biased results in dynamic water bodies, once again emphasizing the need for accurate validation data (Collin et al., 2023).

Table 3: Accuracy statistics derived from N in-situ matchups for bathymetry
(Adapted from Collin et al. 2023)

Test site	**Best band combination from NN**	**R²**	**RMSE [m]**	**N**
Bréhat Island	All eight bands	0.78	1.19	2998
Saint Berthélemy Island	All eight bands	0.95	1.57	7585
Teti´aroa Islands	RGB + Yellow	0.69	1.58	3540

In a study Niroumand-Jadidi et al. (2022) the authors explore the potential of Landsat-9 for river bathymetry retrieval, comparing its depth retrieval capabilities with SuperDove and Sentinel-2. This is done through both a neural network and an optimal band ratio analysis (OBRA). Additionally, the study examines the influence of enhancing the signal-to-noise ratio (SNR) of SuperDove imagery through downsampling data to 15m spatial resolution and comparing results with resampled data from the other two sensor at hand. Improvements from the novel bands were additionally investigated by modelling bathymetry from SuperDove data with and without them. Figure 21 shows the results for a stretch of the Colorado River for both downsampling and band emission. Here, reduced noise in the coarser resolution data (right column) improved on model results, as did the novel bands (top row).

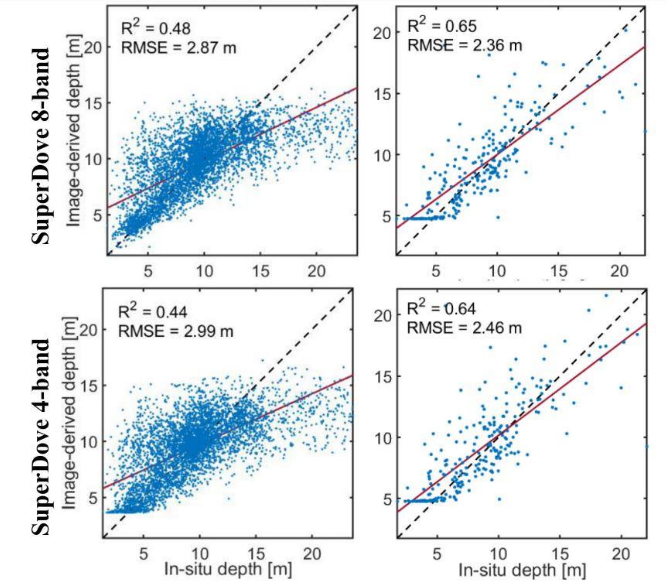

Figure 21: In-situ matchup validation of bathymetry retrieval with SuperDove imagery. Left: Original resolution. Right: 15-m resolution (Adapted from Niroumand-Jadidi et al. 2022).

Table 4: Accuracy statistics derived from in-situ matchups for bathymetry (Adapted from Niroumand-Jadidi et al. 2022)

Satellite Sensor	R^2	RMSE [m]	MAE [m]	Bias [m]
Landsat-9 (30m)	0.70	1.99	1.19	1.01
Landsat-9 (15m)	0.80	1.97	1.20	1.03
Sentinel-2 (10m)	0.69	2.21	1.18	0.99
Sentinel-2 (15m)	0.68	2.23	1.22	0.99
SuperDove 8-band (3m)	0.48	2.87	1.24	1.04
SuperDove 8-band (15m)	0.65	2.36	1.22	1.05
SuperDove 4-band (3m)	0.44	2.99	1.26	1.04
SuperDove 8-band (15m)	0.64	2.46	1.21	1.05

Between sensors, the best results were observed with pan-sharpened Landsat-9 images at the 15-meter spatial resolution. Table 4 shows RMSE, R^2, MAE and Bias for all data formats. For all sensors, the neural network approach significantly outperformed OBRA. The latter is therefore excluded in the overview. It is important to note that the authors relied on TOA reflectance products, stating a degradation of the results attributable to poor atmospheric correction. They emphasize the need for accurate atmospheric correction in studies that apply physics-based approaches for bathymetry or water-quality retrieval (Niroumand-Jadidi et al., 2022).

Lastly both SuperDove and older generations in the constellation have been shown to be a valuable resource for detecting and mapping water bodies, flood inundation or river connectivity (Mishra et al., 2020; Paulino et al., 2023; Qayyum et al., 2020) as well as extents of benthic habitats in optically shallow water (Wicaksono et al., 2023; Lee et al., 2023; van An et al., 2023; Wicaksono and Lazuardi, 2021).

3.4. Atmospheric Correction of Satellite Data

The studies outlined in the previous chapter either relied on TOA reflectance or the surface reflectance product available for download from PlanetLabs. The atmospheric correction for the basic products is done using the 6SV2.1 radiative transfer code, a widely used and validated method in the remote-sensing community. Developed to model the solar radiation reflection within a coupled atmosphere-surface system, 6SV2.1 accommodates a diverse set of atmospheric, spectral, and geometrical scenarios (Shi and Xiao, 2019). Aerosol optical depth, water vapor and ozone information are retrieved from MODIS near-real-time data. However, initial tests with SuperDove imagery as a Level-2 product directly from PlanetLabs have not led to satisfactory results for the subsequent inverse modelling of the high-altitude scenes in the Peruvian Andes. For this study, atmospheric correction was done in ACOLITE, a processor developed at the Royal Belgian Institute of Natural Sciences (RBINS).

3.4.1. ACOLITE

ACOLITE is freely available as either a binary version or as a generic GitHub module and has an active community with continuous development. It supports a wide range of sensors and is easy and fast to implement with minimal settings. The software uses the dark spectrum fitting (DSF) approach in its default processing, which has been applied to turbidity estimations, bathymetry and algal bloom monitoring in previous studies (Vanhellemont and Ruddick, 2021). The DSF correction inherently uses two assumptions: First, the atmosphere is homogenous over the entire scene that is to be processed. The path reflectance ρ_{path} is therefore constant. Second, the scene contains pixels where surface reflectance ρ_s is close to zero in at least one of the available bands for ρ_{path} estimation (Vanhellemont, 2019a).

From the lowest observed TOA reflectance ρ_t in each band, a dark spectrum ρ_{dark} is constructed. From the derived ρ_{dark}, the best fit band and model combination is selected to estimate ρ_{path}. This is done in three steps:

1) Based on the scene specific illumination and viewing geometry ρ_{path} is calculated with 6SV for two different aerosol models and the aerosol optical thickness τ_a at 550 nm. For each band, assigned with a band weighted wavelength λ, and each aerosol type from LUTs of the aerosol model, the $\rho_{dark}(\lambda)$ is limited by two ρ_{path} (λ) values. These values correspond to the steps of τ_a in the LUT. Then, the final τ_a is estimated from the bounding values by linear interpolation to the $\rho_{dark}(\lambda)$.
2) For each aerosol model, the band giving the lowest non-zero estimation of τ_a is selected since higher values in other bands will lead to negative values for the dark pixels in the lowest band.

3) Finally, one aerosol model is selected from the lowest *Root Mean Squared Difference* (RMSD) between the ρ_{dark} and ρ_{path} for each band pair with the fitted band from the previous step. The aerosol models include either a continental (MOD1) or maritime (MOD2) composition of aerosols from 6SV and their respective characteristics.

Finally, having selected the best fitting band and aerosol model, parameters that are required for atmospheric correction can be retrieved from the LUT for all bands. These are ρ_{path}, the two-way total atmospheric transmittance t_{tot} and the spherical albedo of the atmosphere s_a.
Surface reflectance of a pixel can then be calculated as:

$$\rho_s = \frac{\rho_{pc}}{t_{tot} + s_a * \rho_{pc}}$$

And:

$$\rho_{pc} = \frac{\rho_t}{t_{gas}} - \rho_{path} - \rho_{sky}$$

Where ρ_t is the TOA reflectance, ρ_{pc} is the path corrected reflectance, t_{gas} the total gas transmittance and ρ_{sky} is an approximation for the air-water sky interface. For water pixels this is determined analytically while land pixels are set to 0. Surface reflectance is retrieved both over water and land, assuming the water surface is fully treated (Vanhellemont, 2019a).
To evaluate the performance of atmospheric correction, satellite derived data needs to be compared to in situ measurements, ideally taken with minimal time deviation from the satellite overpass, to eliminate changing conditions in irradiance or atmospheric composition. In a study by Vanhellemont (2020), PlanetScope data from the older four-band dove generation processed with ACOLITE was validated at two different sites in the Belgian coastal zone with matchups from an autonomous measuring PANTHYR system. Its performance was then compared to the Landsat OLI and Sentinel-2 MSI sensor. For the in-situ measurements, water leaving radiance L_W was computed from the average of a series of measurements for upwelling radiance L_u and sky radiance L_d in time intervals between one and seven minutes (Vanhellemont, 2020). Out of 88 matchups found between the in-situ PANTHYR measurements and Dove imagery, the RMSD error was over 0.01 for the water reflectance, performing worse than Sentinel and Landsat. Reflectance in the NIR was systematically overestimated indicating a poor performance of the NIR band (Vanhellemont, 2020). Nonetheless, ACOLITE has shown to provide good results for aquatic applications across water bodies and satellite sensors (Maciel and Pedocchi, 2022; Pereira-Sandoval et al., 2019; Vanhellemont, 2019b; Braga et al., 2022).

3.4.2. Parameter Settings in ACOLITE

ACOLITE provides the user with a large array of processing options that can be specified in a settings file. This file can be directly imported in the GUI or through a command in a suitable python environment. Minimal parameter settings can be set in the GUI of the binary version in ACOLITE (see Figure 39 in the Appendix). Here, only the input Level-1 data bundles and the desired output parameter are necessary for initial processing.

For this study, individual setting files are written and processed in batch in a dedicated Python 3 environment for the analysis of the satellite derived spectra. This was done separately for each parameter to deduct its effect on the spectrum for water pixels. Results are output across individual bands as R_{rs}, defined in ACOLITE as the surface reflectance for water pixels divided by pi. The bands are then stacked together to a multi-band raster in a geographic information system (GIS). No pixels are masked in the processing, as this is done later in WASI through setting reflectance thresholds when processing the Level-2 image data. The elevation was set to the altitude of the lake to account for changes in atmospheric pressure in a high-altitude environment. This is achieved even more precisely by providing access to a NASA *EarthData* account which will compute atmospheric pressure from available digital elevation model (DEM) data (Vanhellemont, 2020).

Information on the best practices of user settings, scripting and visualization can be found in the ACOLITE manual (latest version from August 2021) or the user forum (ACOLITE, 2024). To investigate performance under different parametrization and to define best practices for the processing of the Level-1 data from SuperDoves, following settings were tested:

- Wavelength limitation for the band selection with lowest ρ_t
- Fixed τ_a at 550nm
- Fixed aerosol model and associated LUT.
- Glint correction with two available models
- Auxiliary data for atmospheric pressure (DEM) and gas transmittance (ozone and water vapor concentration)
- ROI size for initialization

As it was later shown, different regions of interest (ROI) that were set during initialization had a significant impact on the chosen band and aerosol model and therefore the derived signal. Figure 22 shows the four ROIs which were ultimately compared. These polygon envelopes crop the raw Level-1 data to the set extent before further processing in ACOLITE. Each region size considered potential use cases that advocate for the given extent: The *Fullscene* covers the entire extent of Lake Junin, including the inaccessible shallow water area in the northwest of the lake. The *Subset* covers all field measurement points and include both the deepest areas of the lake and the more pronounced shallow areas, demarcated by the reed belts in the south. The area labelled as *Common* is the largest area that the three scenes from subsequent days shared with each other in their respective overpasses. Since the SuperDove unit on the 24th of June did not capture the northwestern area of the *Fullscene* extent, this was included to find the maximum area where each sensor had the same available extent. Lastly, the *Deep Water* ROI was included as an area with significantly more water pixels than land pixels, and covering an in-situ transect over the deepest area in the lake. Deviations in satellite derived R_{rs} from SuperDove instruments due to different ROI initialization are quantified as the percent difference from the mean reflectance between the different settings.

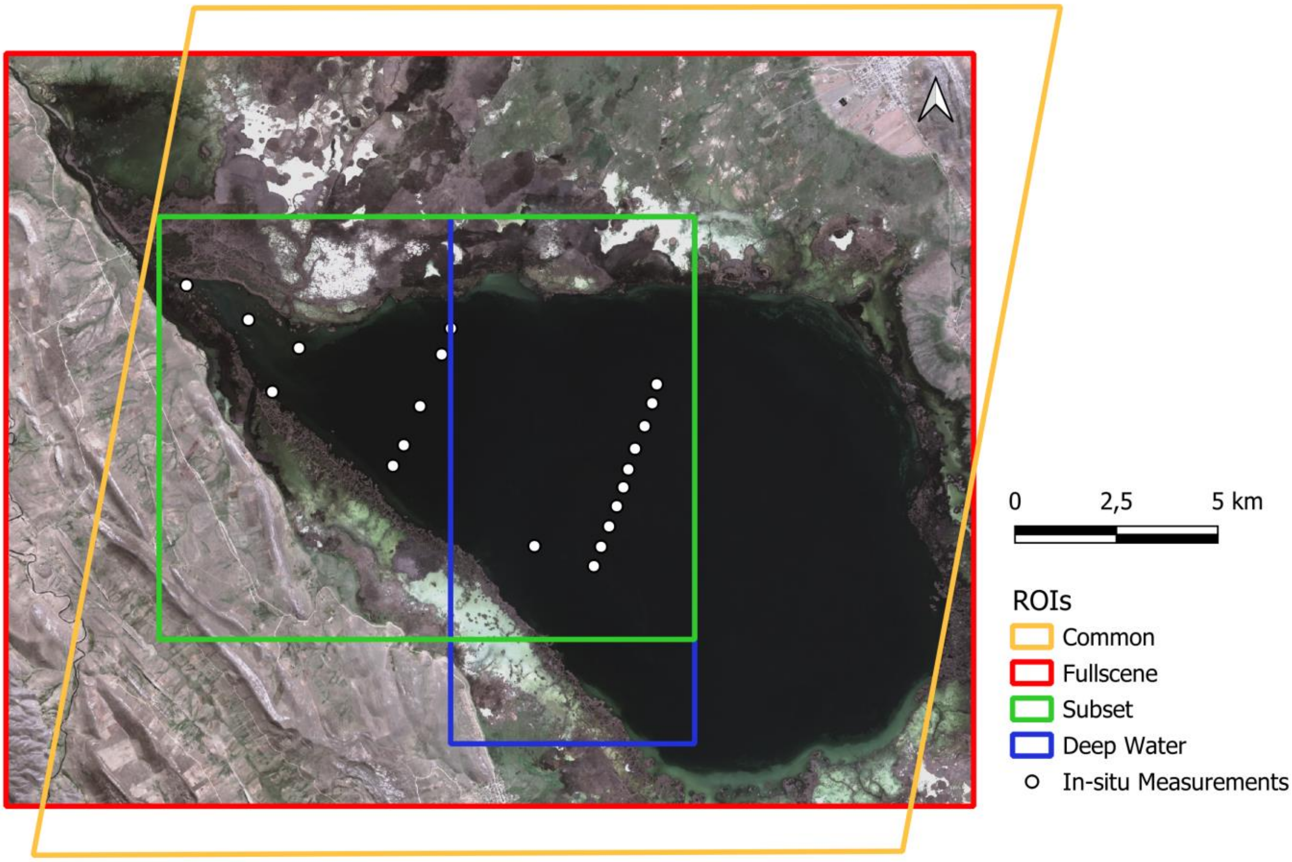

Figure 22: Bounding Boxes for ROIs processed in ACOLITE. Fullscene covers the entire lake, Subset all field stations points, Deep Water the transect in the deepest part and Common the largest overlap between three consecutive images. The Image extent was cropped to the Fullscene.

3.5. Assessment of Level-2 Data Quality

To assess the accuracy of the atmospheric correction, R_{rs} output from minimal user settings were validated with the in-situ measurements from the field campaign. Therefore, no bands were excluded, no fixed AOT was set, no glint correction was applied and the default DSF algorithm was used in ACOLITE. To combat the noise in the SuperDove images, a 30-by-30-meter buffer was set around each validation point, and pixel values within that buffer area were averaged from the Level-2 image. Consequently, one in-situ measurement was compared to the mean of 100 pixels with 3-meter spatial resolution from a SuperDove. To compare the performance of atmospheric correction between sensors, a Sentinel-2 scene from the 24th of June was also investigated and validated for the same buffer size as the average of nine 10-meter pixels as this was the set output size for the Sentinel-2B image. As the ground truth data, the R_{rs} from the in-situ water spectra corrected for surface reflection were used. For this, a total of 20 points were available:

- **JU_01** – **JU_04** (Collected on the 26th of June)
- **JU_12** – **JU_16** (Collected on the 27th of June)
- **JU_20** – **JU_30** (Collected on the 28th of June)

The major challenge for satellite validation is the temporal overlap with the image acquisition and the in-situ measurement (Leigh et al., 2023). In-situ data in shallow and deep-water areas from the boat were collected on three days and on these three days, only one SuperDove image on the 26th of June is available. On the following days clouds covered almost the entire lake during the overpass. Here, even the high temporal resolution could unfortunately not guarantee a close temporal matchup. A Landsat-9 scene on the 28th was also heavily obstructed by clouds and could therefore not be used for additional validation. SuperDove scenes with no clouds over the water body and no apparent glint were also available on the 24th and 25th of June. As the conditions of both the water body, the weather and the atmosphere were stable, images from those days were used to compare in-situ R_{rs} data and satellite derived R_{rs}.

In high spatial-resolution image noise can be large, especially given that the signal over deep water is inherently low. Even small noise can make up a large fraction of the total signal measured by a sensor. The signal-to-noise ratio (SNR) can be used to assess image quality and to identify potential limitations of further analysis with the data at hand (Niroumand-Jadidi et al., 2022; Jorge et al., 2017). The SNR can be calculated as the mean signal within an array of pixels divided by the standard deviation of the signal within the same extent.

$$SNR = \frac{mean}{std}$$

While visual interpretation of an image does not depend as strongly on a high SNR, uncertainties in image processing for multispectral applications are often strongly affected by the noise in remote sensing data. To inspect the spatial distribution of the noise in both the Level-1 TOA radiance data and the atmospherically corrected raster images with R_{rs} values, maps for the SNR in each of the eight bands of a SuperDove image were created. In adaptation to the SNR methodology from a report on the quality assessment for SuperDove data, a sliding window with a set kernel size computes the local statistics within the window and writes the SNR value for the pixel at the pixel position in the iteration (Saunier and Cocevar, 2022). The results are thus images where each pixel represents the SNR value for the set window size around it. A water mask based on a threshold value in the NIR band where the TOA reflectance ρ_t was above 0.035 was applied to the image for visualization of only water pixels, as land surface showed to have a significantly higher SNR. Based on these images, areas within the lake with high homogeneity were identified and subsequently used to define areas of interest (AOIs) within the lake to compare Level-2 data between scenes and different processing options. The same methodology was applied to the Sentinel-2B scene and SNR improvement (SNRI) for an AOI was quantified as follows:

$$\mathrm{SNRI} = 10 \cdot log_{10}(\frac{SNR_{Sentinel}}{SNR_{SuperDove}})$$

The AOIs also defined areas for which model initialization in WASI were carried out. The inverse modelling of the representative spectra within these are subsequently indicative of the data quality. When a satellite derived spectrum cannot be inversely modelled within realistic parameter ranges, the input data is assumed to be unsuited for this application.

Finally, consistency between consecutive images were compared regarding their spectral shape. With daily imaging capacities, it is important that data from the PlanetScope constellations is consistent between individual sensors, flocks and ideally generations. The high temporal resolution enables comparative analysis of the spectra measured for single pixels or AOIs and large differences can be detected simply by visual interpretation of the spectral profiles or quantified by differences in band ratios or indices. This must however be done under the assumption that differences from the at sensor signal are directly related to the sensor itself and not to changing environmental conditions. This can be reliably done for PICS sites where temporal stability of the observed surface area is expected to be extremely high, especially so when images can be acquired daily (Khadka et al., 2021). In more dynamic aquatic systems, attributing changes to either sensor or environment may be challenging. Nonetheless, for the analysis at hand the three consecutive images from the 24th, 25th and 26th of June 2023 are compared. This is done for the defined AOIs and deviations between sensors are quantified as the percentage difference from the mean signal between them. For the results, four AOIs were considered and are henceforth referred to as:

- Deep Water Transect 1
- Deep Water Transect 2
- Shallows North
- Shallows South

Band ratios that can be used as proxies for water extent and constituent concentrations are also investigated and absolute differences between the ratios from different days are calculated. This was done for the *Subset* extend without masking land to visualize differences in changing signal between water and land. Although not optimized to the water body and sensors at hand, following band indices or band ratios are included for visualization purposes:
First, the Normalized Difference Chlorophyll Index (NDCI) developed to use the reflectance peak with maximum sensitivity at 700 nm in the *Red-Edge* band and the strong absorption of chlorophyll-a pigments between 665 nm and 675 nm (Mishra and Mishra, 2012).

$$NDCI = \frac{Rrs(705) - Rrs(665)}{Rrs(705) + Rrs(665)}$$

Second, the Normalized Difference Water Index (NDWI) used to detect and highlight water coverage from satellite imagery using the *Green* and NIR band for water targets (Yoon and Choi, 2018).

$$NDWI = \frac{Rrs(556) - Rrs(865)}{Rrs(556) + Rrs(865)}$$

Finally, the same maps were created for all possible combinations of band ratios to provide an overview of differences between the consecutive SuperDove images which directly related to the band-to-band performance of the individual sensor (Shybanov et al., 2023). These images were created to show the spatial distribution of band-to-band differences between individual scenes. While these can be derived from the spectral profiles plotted for a single AOI from all sensors, the spatial distribution of differences between band ratios may help identifying areas of the water body where calibration differences were more pronounced.

4. Results

Results for this thesis are the collection of validation data for the Level-3 parameters and the evaluation of SuperDove images as a suitable data product for the modelling of these parameters. The location of the field stations and AOIs are shown in Figure 23 and results for all in-situ measurements are provided in Appendix I. These include the water depths from tape and sonar measurements, chlorophyll-a concentration from inverse modelling of the in-situ water spectra, Secchi depth as well as date of collection and coordinates. *Chapter 4.1* summarizes the chlorophyll-a concentration results from two laboratories in Peru and the concentrations derived from field spectrometer data for all water stations. *Chapter 4.2* outlines the collected validation data for water depth determination and the validation raster data from the bathymetry report from 2006. *Chapter 4.3* summarizes and visualizes the image noise of the SuperDove scene from the 24th of June 2023 and a Sentinel-2B image from the same day. The spectral signatures of the AOIs for three consecutive days from SuperDove imagery are presented in *Chapter 4.3* and *Chapter 4.4* and their differences due to ROI initialization and day of acquisition are outlined. Satellite derived R_{rs} validation is shown in *Chapter 4.5* for SuperDove and Sentinel-2B. Finally, challenges of initializing these reflectance spectra in WASI for deep water are summarized in *Chapter 4.6*.

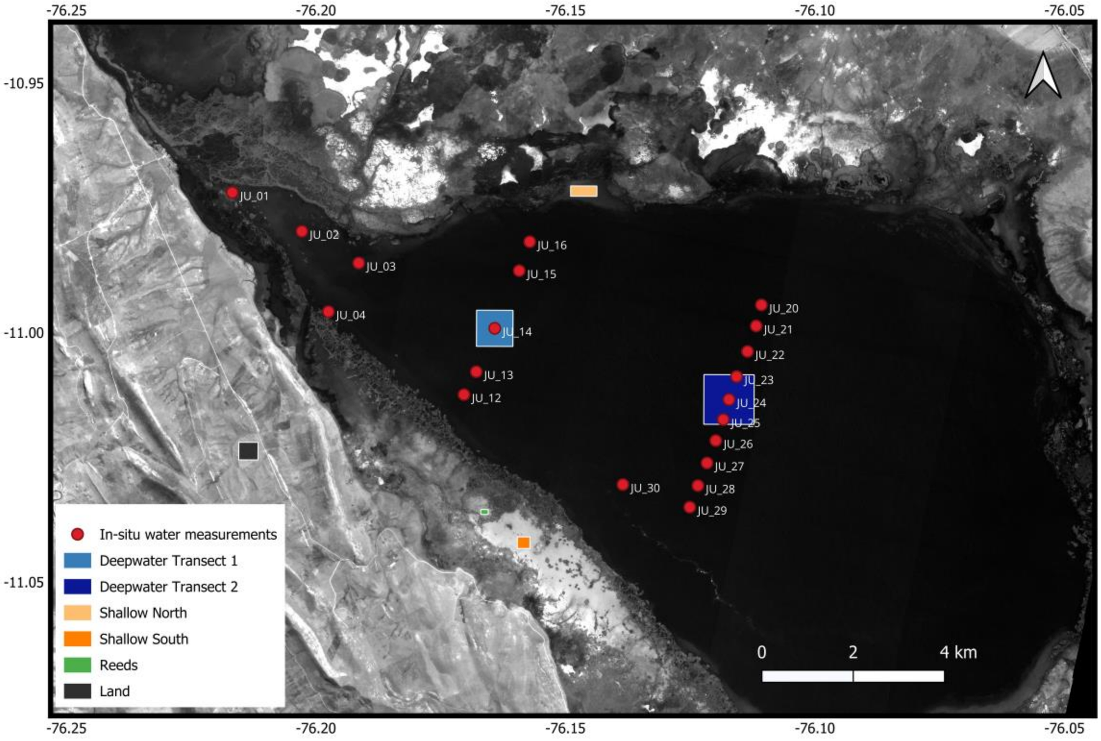

Figure 23: Overview of AOIs and field-measurement points for water at Lake Junin.

4.1. Uncertainty of Chlorophyll-a in-situ Data

Table 5 shows the chlorophyll-a concentrations that were measured in the two laboratories in Lima and the concentration derived from inverse modelling of the field spectrometer data. The SAG laboratory in Lima did not provide precise values as every water sample was considered below their limit of concentration detection. Concentrations from the ocean institute laboratory IMARPE agreed with SAG with values below 3 µg/l for all points and provided precise values with an average concentration at 1.08 µg/l. The concentrations derived from WASI were significantly higher for points JU_01 to JU_04 where water depth was below two meters. While the correspondence between the spectrum fitted for a dominant phytoplankton group, decisive for the chlorophyll-a concentration, and the measurement was good (mean residuals of 1.47E-04), the agreement between the laboratory and WASI is poor. Here, the model overestimates chlorophyll concentration. This can likely be attributed to the spectral ambiguities in optically shallow water where the bottom signal and other water constituents strongly influence the measured reflectance. The MAE between IMARPE and WASI for all stations is 2.76 µg/l, with an MAE of 0.8 µg/l when the stations in the water below 2 m are excluded. For each of these four shallow points, bottom substrate was also extracted and measured. Their spectral characteristics were however not yet included for the results in Table 5 and the inverse modelling of the field measurements. The chlorophyll concentration could potentially be improved through regional adaptation where the measured albedo of the bottom substrate is used in the inverse modelling of the field spectrometer data. Figure 24 shows the correspondence between the IMARPE concentrations and WASI. The four points in the shallow water are marked in the plot, as well as JU_22 where the largest absolute error measurements in deep water was observed. The linear regression and accuracy statistics for the model are included after the removal of these outliers. The RMSE here is 0.31 µg/l with an R^2 of 0.62.

Table 5: Comparison of results for Chl-a concentrations in µg/l from two laboratories in Lima and the inverse modelling of field spectrometer data in WASI

	JU_01	JU_02	JU_03	JU_04	JU_12	JU_13	JU_15	JU_16	JU_20	JU_22	JU_24	JU_27	JU_29	JU_30
IMARPE	0.08	0.35	0.27	0.70	1.07	0.61	1.20	1.86	1.02	0.41	2.07	2.24	1.66	1.24
SAG	<3.0	<3.0	<3.0	<3.0	<3.0	<3.0	<3.0	>3.0	<3.0	<3.0	<3.0	<3.0	<3.0	<3.0
WASI	13.65	4.89	7.27	6.27	0.78	0.65	1.34	1.38	2.06	2.90	2.91	3.24	2.77	1.83

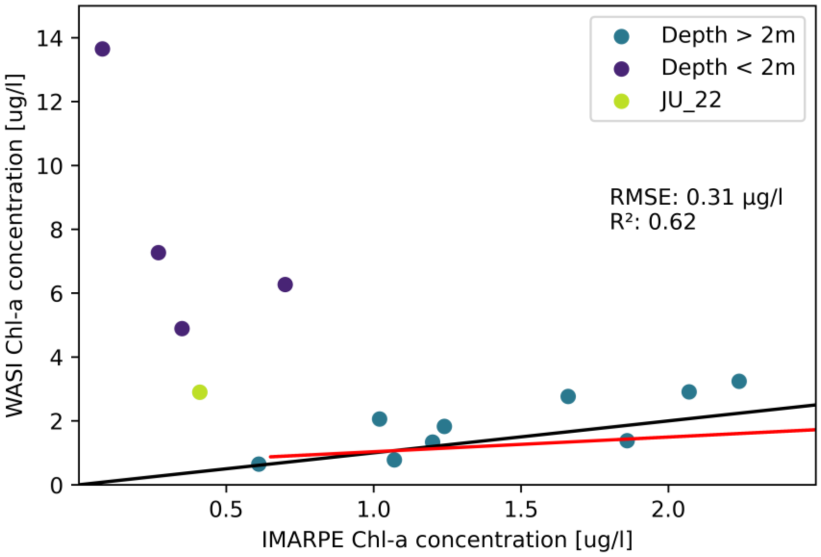

Figure 24: Comparison between chlorophyll-a concentration from laboratory analysis by IMARPE and inverse modelling with WASI from spectrometer data. Red line: Linear regression. Black line: 1-1 line through origin

4.2. Uncertainty of water depth

Figure 27 shows the North-South profile of a transect between field station JU_03 to JU_04, as well as a transect between field station JU_10 to JU_17. The stations along the transects are marked on the graph at the depth corresponding to measurements with the steel tape. In the first transect, the distinct increase in depth to over three meters is due to a channel that was dug to guarantee a lane of passage for boats. The profile of the second transect shows the general deepening of the lake, however, outliers in the data collection from the ping sonar can be seen. It is assumed that these points are underwater features that return the echo sounder signal before it can reach a point that accurately represents the depth of the lakebed. It is also notable that the water depth at each point from the validation measurement with the steel tape measure, except for JU_15, is lower than the water depth logged from the ping sonar. This is likely due to the deeper penetration depth of the echo sounder in the bottom substrate. Figure 26 compares the depth measurements between sonar and tape measurements in the left subplot. The MAE between the measurements was 0.28 m, with an RMSE of 0.15 m. Field observations with the same USV and steel measure tape at Lake Starnberg in Germany have shown an RMSE of 0.10 m at 62 field observation points between ping sonar and manual measurements. The error also increased with depth due to curvature of the tape, underwater currents, and varying lake beds, increasing the offset due to the conic characteristic of the emitted signal.

Figure 25 shows the interpolated water depth map from 2006 corrected for a 0.78 m offset based on the intercept of the linear regression between field measurements and pixels from the uncorrected. The area in light green in the northern inundation zone are now dry areas, assuming water level deviations are identical in that area as they are for the entire lake. The MAE between the corrected reference raster and depth measurements from the steel tape is 0.39 meters as shown in the right subplot in Figure 26. This updated map of water depth is a valuable resource for the validation of bathymetry through inverse modelling of satellite data. It was further used in model initialization in WASI as a masking band by appending the raster to the satellite image in a dedicated band.

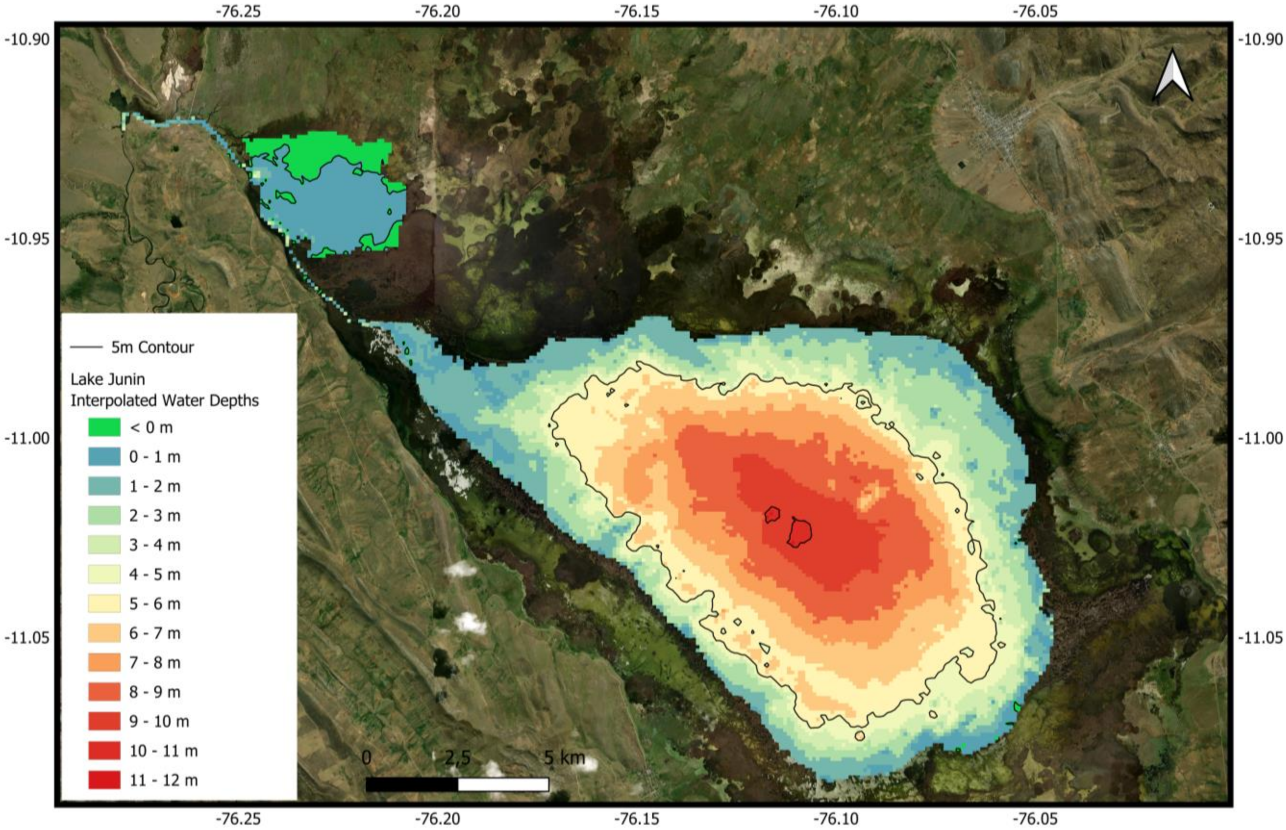

Figure 25: Water depth map based on interpolated data from a topographic survey. The light green areas are assumed to not be inundated. Five-meter contour line to delimit deep water in the middle of the Lake.

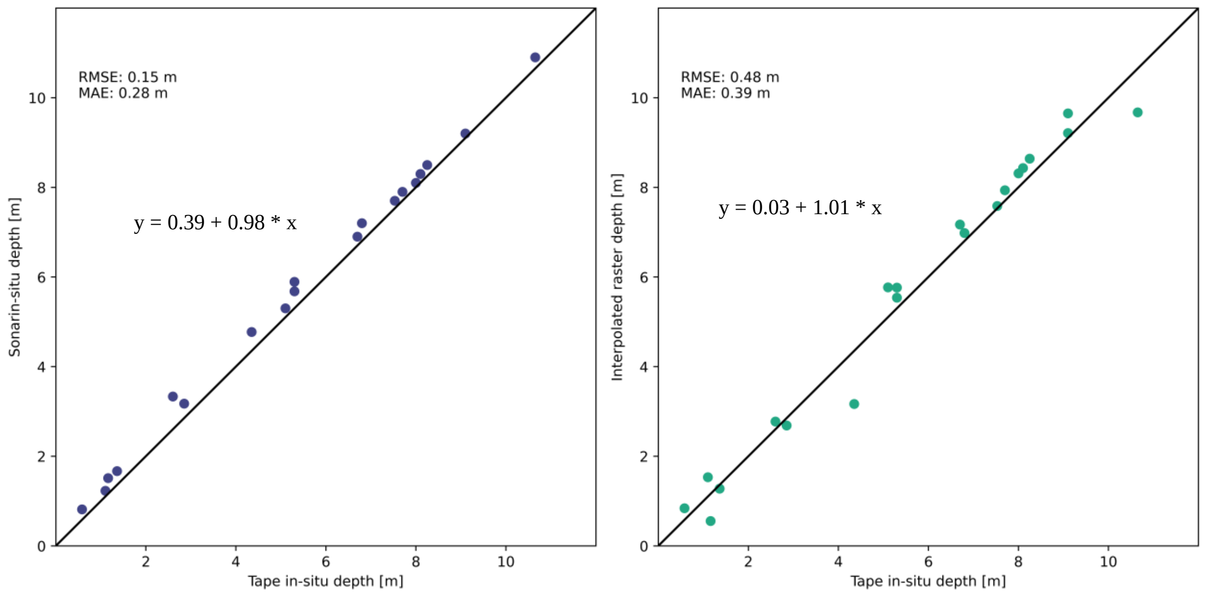

Figure 26: Comparison between in-situ measurements from steel tape and sonar (Left) and between in-situ tape measurement and the depth raster (Right). The MAE is calculated for the true values and therefore larger than RMSE on the right subplot.

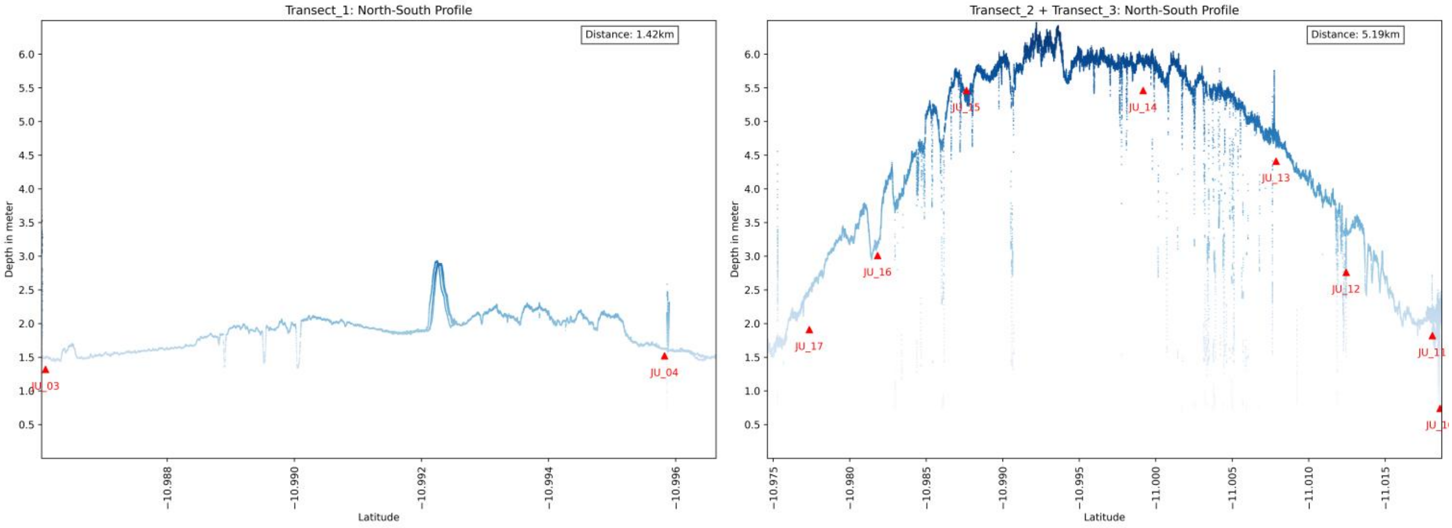

Figure 27: Water depth profiles from USV transects between field stations JU_03 and JU_04 (Left) and between field stations JU_10 and JU_17 (Right)

4.3. Image Noise

Figure 28 shows the SNR for water pixels for the *Subset* extent. Filter size is set to 3, so that for every ratio, a total of 9 pixels were averaged. The TOA radiance of the SuperDove from the 24th of June 2023 shows the highest mean SNR of 107:1 in the second band at 490 nm and the lowest SNR of 10:1 in the NIR band at 865 nm. The SNR for the bottom of atmosphere in Figure 29 is noticeably lower in all bands and the highest SNR for all water pixels is found in the fourth band at 565 nm central wavelength. A reduction in SNR is attributed to a reduction in the inherent signal when comparing outputs for the same filter size. This is consequently most notable in the shorter wavelength bands that are affected the most by the atmosphere and the subtraction of the path radiance. SNR in the NIR is low due to the high noise in deep water and low due to the small signal in shallow water. Considering the spatial distribution of the SNR, two AOIs stand out: The south-western shallow water area, separated from the main water body by a thick reed belt and an optically shallow lagoon in the north of the lake. Especially in the shallow southern AOI, the SNR is high compared to the rest of the lake.

Sensor artefacts along stripes in the individual image frames are visible in all bands and generally pause through all further data analysis if no spatial smoothing is applied to the data. Identical images have been created for larger filter sizes where generally a lower SNR was observed. This was most pronounced in the shallow areas as a larger filter would additionally introduce noise from the heterogeneity of the lake bottom and the adjacent vegetation. Spatial patterns and SNR were consistent between the three consecutive images in June.

Figure 30 shows the same method applied to the Sentinel-2B scene from the same day. Output was set to 20 m pixel size in ACOLITE, and the first band with 60-meter spatial resolution is not included as the down and consequent up sampling would distort the results. A higher SNR for Sentinel-2B can be observed in the shared bands from the visual interpretation of the images below. For the Sentinel-2B image sensor artifacts in the NIR bands can be observed. Here, large areas in the lake along detector orientation showed highly invariable reflectance, saturating the scale in the images.

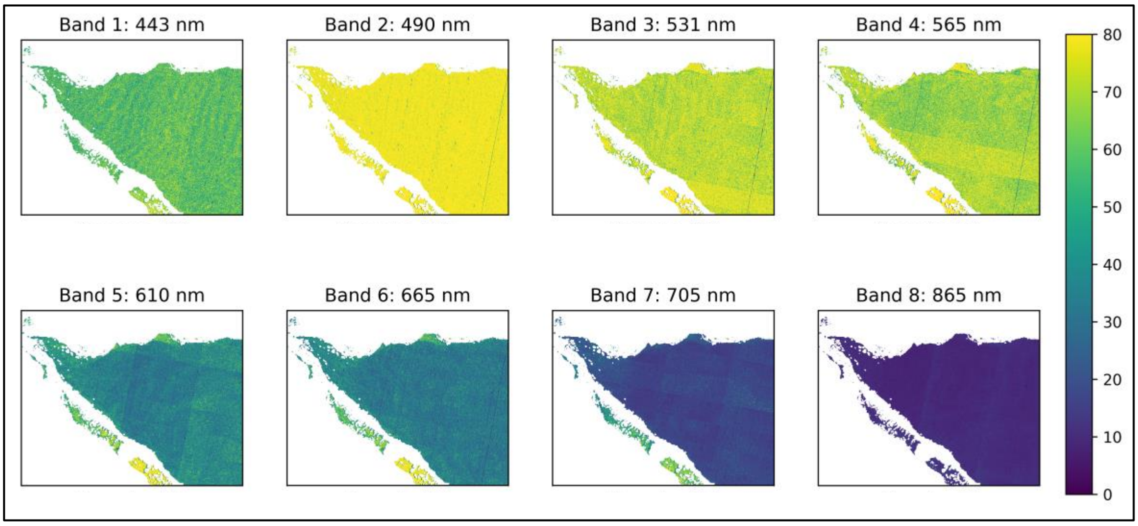

Figure 28: SNR for TOA Radiance from SuperDove image on the 24.06.2023

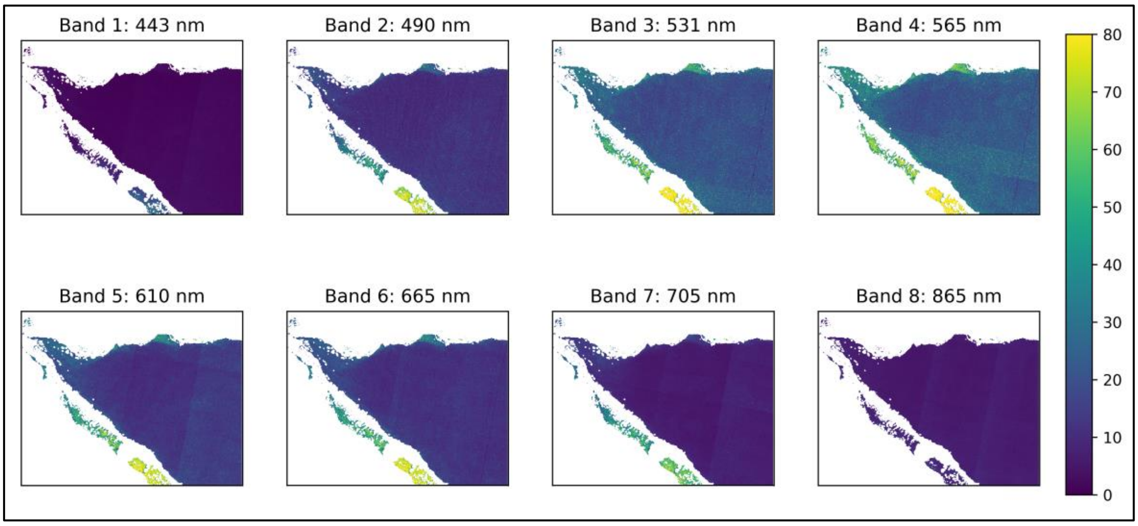

Figure 29: SNR for R_{rs} from SuperDove image on the 24.06.2023

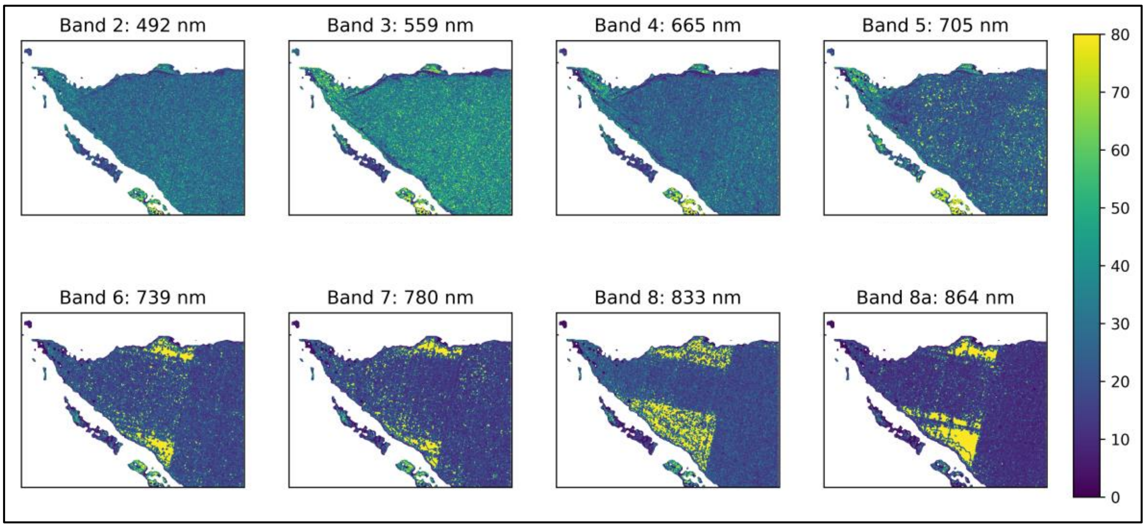

Figure 30: SNR for R_{rs} from Sentinel-2B on the 24.06.2023

Table 6 and Table 7 show the mean SNR for each pixel within the two deep water AOIs and the optically shallow areas in the north and south of the lake. For the SuperDove scene from the 24th of June, the signal in the Coastal Blue at 443 nm cannot be differentiated from the noise. For the deep-water inversion in WASI, model initialization should therefore be carried out without fitting for this wavelength. The SNR improvement from Sentinel-2B of the same day to the SuperDove image is summarized in Table 8 for the five shared bands. Positive numbers indicate higher SNR within the AOI for the Sentinel-2B image. The Sentinel-2B image showed higher SNR for both AOIs in the deep water, but lower SNR for the shallow AOIs at ~565 nm. The highest SNR deterioration was observed for the shallow AOI in the south with a bright bottom for the RGB bands (SNRI: -2.41).

Table 6: Band specific SNR for AOIs from a SuperDove image on the 24th of June 2023

AOI	Band 1 443 nm	Band 2 490 nm	Band 3 531 nm	Band 4 565 nm	Band 5 610 nm	Band 6 665 nm	Band 7 705 nm	Band 8 865 nm
Deep Water Transect 1	1	11	19	20	11	11	6	6
Deep Water Transect 2	2	13	20	24	14	12	7	6
Shallow North	3	29	50	62	40	37	15	6
Shallow South	24	94	133	136	99	101	70	11

Table 7: Band specific SNR for AOIs from a Sentinel-2B image on the 24th of June 2023

AOI	Band 2 492 nm	Band 3 559 nm	Band 4 665 nm	Band 5 704 nm	Band 6 739 nm	Band 7 780 nm	Band 8 833 nm	Band 8a 865 nm
Deep Water Transect 1	29	39	25	607	98	70	21	15
Deep Water Transect 2	29	40	30	29	19	16	18	12
Shallow North	38	51	45	46	>1000	>1000	>1000	>1000
Shallow South	64	78	88	99	62	61	48	45

Table 8: SNR Improvement (SNRI) from Sentinel-2B to SuperDove in shared bands

AOI	~490 nm	~565 nm	~665 nm	~705 nm	~865 nm
Deep Water Transect 1	4.21	2.9	3.6	20.0	4.0
Deep Water Transect 2	3.48	2.3	4.0	6.2	3
Shallow North	1.17	-0.8	0.86	4.7	-
Shallow South	-1.67	-2.41	-0.6	1.5	6.1

4.4. ACOLITE Initialization

Figure 31 shows the R_{rs} spectra as the mean values within selected AOIs and offsets caused by the selection of a different ROI size for the initialization in ACOLITE. A change of ROI will mainly lead to a change in estimated AOT, but it does not drastically change the shape of the spectrum. Instead, it just leads to a shift up or down. The construction of the DSF tends to bias the aerosol optical thickness low and the resulting water reflectance high, especially for a noisy sensor. For the image acquired on the 26th of June, ROI selection had no effect, implying that the DSF algorithm always selected the same fitting band and aerosol model. However, for the scenes on the 24th and 25th June, this made a noticeable impact on the magnitude of derived R_{rs}. While the larger ROIs (*Common* and *Fullscene*) always led to the same model selection, values deviated from those derived by the *Subset*. Values derived from the *Subset* are lower on the 24th, but higher on the 25th.

From the *Deep Water* ROI that only covered points along the second transect, a difference in reflectance compared to the other ROIs can also be observed. Here, values were slightly lower for both days compared to the *Subset* as a higher AOT was estimated. Table 9 gives an overview of the AOT at 550 nm as well as the selected aerosol model and fitting band for minimal settings in ACOLITE. Only difference in parametrization is the bounding box within the raw data was processed. For best comparability, a fixed AOT should be set for the SuperDove images with the aerosol model and AOT estimate. This was tested by processing the Sentinel-2B image with minimal settings for the extraction of an AOT that is not biased to an individual SuperDove. However, high sensitivity to ROI selection of the DSF was likewise present as shown in the table below.

Table 9: Overview of best fit Aerosol Model and Fitting Band from the DSF algorithm. Rows are model parameters for SuperDoves on three consecutive days and Sentinel-2B on the 24th.

Date	**Subset**			**Deepwater**			**Fullscene**		
	AOT	**Aerosol Model**	**Fitting Band**	**AOT**	**Aerosol Model**	**Fitting Band**	**AOT**	**Aerosol Model**	**Fitting Band**
SD 24.06	0.0683	MOD1	*Blue*	0.0287	MOD2	*Yellow*	0.0793	MOD2	*Blue*
SD 25.06	0.0276	MOD2	*Yellow*	0.0656	MOD2	*Red*	0.0331	MOD2	*Yellow*
SD 26.06.	0.0313	MOD1	*Red*	0.0313	MOD1	*Red*	0.0313	MOD1	*Red*
S2B 24.06	0.0392	MOD1	8A	0.0016	MOD1	8A	0.0449	MOD1	8A

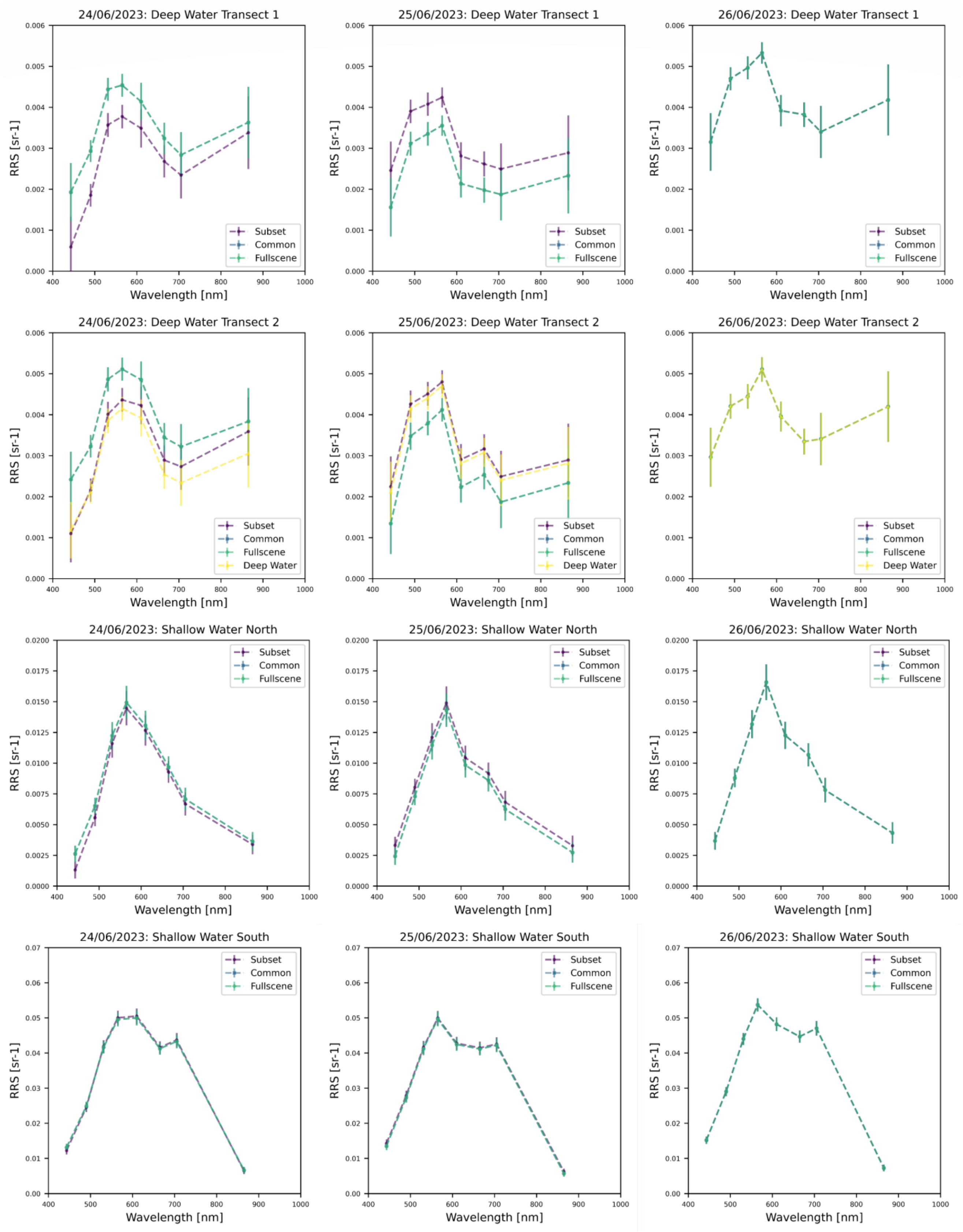

Figure 31: Influence of initial ROI selection for processing in ACOLITE. Columns show spectra for AOIs, rows show spectra for each of the images from three consecutive days. Vertical bars show standard deviation of pixel values within AOI.

Table 10 summarizes the differences in R_{rs} as the percentage deviation from the mean reflectance from the ROI selection during initialization. Highest variability was determined for the *Coastal Blue* band with a 54% increase in R_{rs} respective to the mean reflectance in the band. This further suggests disregarding the band for inverse-modelling. Generally, errors above 10% were observed for all bands in the deep water. Since the direction of the percent deviation depended on the day, no recommendation can be made for initial ROI selection. Uncertainties in the strength of the signal for each band due to different approximation of atmospheric parameters need to be considered further.

Table 10: Percent differences of Rrs when ACOLITE was initialized with a different ROI. Rows split for date and AOIs

AOI	Day	ROI	Band 1	Band 2	Band 3	Band 4	Band 5	Band 6	Band 7	Band 8
Deep Water Transect 2	24.06	Mean R_{rs} [sr^{-1}]	0.0016	0.0025	0.0042	0.0045	0.0043	0.0030	0.0028	0.0035
		Fullscene	**54.3**	**29**	**14.7**	**12.6**	12	**16.4**	16.5	10
		Subset	-29.7	-13.7	-5.5	-3.9	-2.5	2.3	-1.1	2.8
		DeepWater	-24.6	-15.4	-9.2	-8.6	-9.5	-14	-15.4	-12.4
	25.06	Mean R_{rs} [sr^{-1}]	0.0019	0.004	0.0042	0.0045	0.0027	0.0029	0.0023	0.0027
		Fullscene	-29.3	-12.2	-10.5	-9.3	**-15.7**	-13.4	**-17.1**	**-12.9**
		Subset	18	7.5	6.5	5.7	9.7	8.2	10.5	7.9
		DeepWater	11.2	4.7	4.0	3.6	6	5.1	6.6	4.9
Deep Water Transect 1	24.06	Mean R_{rs} [sr^{-1}]	0.0013	0.0024	0.0040	0.0042	0.0038	0.0030	0.0026	0.0035
		Fullscene	53.1	22.6	10.9	9.2	8.5	9.4	9.5	3.6
		Subset	-53.1	-22.6	-10.9	-9.2	-8.5	-9.4	-9.5	-3.6
	25.06	Mean R_{rs} [sr^{-1}]	0.0020	0.0035	0.0037	0.0039	0.0025	0.0023	0.0022	0.0026
		Fullscene	-22.3	-11.2	-9.7	-8.8	-13.6	-13.9	-14.3	-10.7
		Subset	22.3	11.2	9.7	8.8	13.6	13.9	14.3	10.7
Shallow Water North	24.06	Mean R_{rs} [sr^{-1}]	0.0020	0.0061	0.0119	0.0147	0.0129	0.0095	0.0069	0.0035
		Fullscene	33.18	7.90	2.62	1.57	1.59	2.10	2.86	3.58
		Subset	-33.18	-7.90	-2.62	-1.57	-1.59	-2.10	-2.86	-3.58
	25.06	Mean R_{rs} [sr^{-1}]	0.0029	0.0077	0.0118	0.0146	0.0102	0.0089	0.0066	0.0030
		Fullscene	-15.40	-4.83	-2.71	-1.98	-2.95	-3.23	-4.43	-9.19
		Subset	15.40	4.83	2.71	1.98	2.95	3.23	4.43	9.19
Shallow Water South	24.06	Mean R_{rs} [sr^{-1}]	0.0127	0.0331	0.0417	0.0498	0.0503	0.0414	0.0435	0.0066
		Fullscene	3.6	25.9	-0.3	-0.5	-0.5	-0.4	-0.5	1.5
		Subset	-3.6	-25.9	0.3	0.5	0.5	0.4	0.5	-1.5
	25.06	Mean R_{rs} [sr^{-1}]	0.0139	0.0276	0.0414	0.0498	0.0426	0.0413	0.424	0.0060
		Fullscene	-2.7	-1	-0.4	-0.3	-0.4	-0.4	-0.4	-4.4
		Subset	2.7	1	0.4	0.3	0.4	0.4	0.4	4.4

4.5. Consistency between spectral profiles from SuperDove instruments

Figure 32 shows the mean R_{rs} spectrum around in-situ point JU_14 for the monthly scenes from August 2022 to August 2023. The low general signal is indicative for optical deep water where the signal in the NIR is often considered as negligible (Kutser et al., 2009). Nonetheless, reflectance in the NIR systematically increase, with the exception for the scenes in February and March. Here, the sediment plume entering the lake from the channel tributaries led to a more distinct spectrum. This illustrates that composition of the water body and seasonality can have a large effect on the spectrum measured by a satellite sensor and the benefit of the spectral analysis of the water leaving signal.

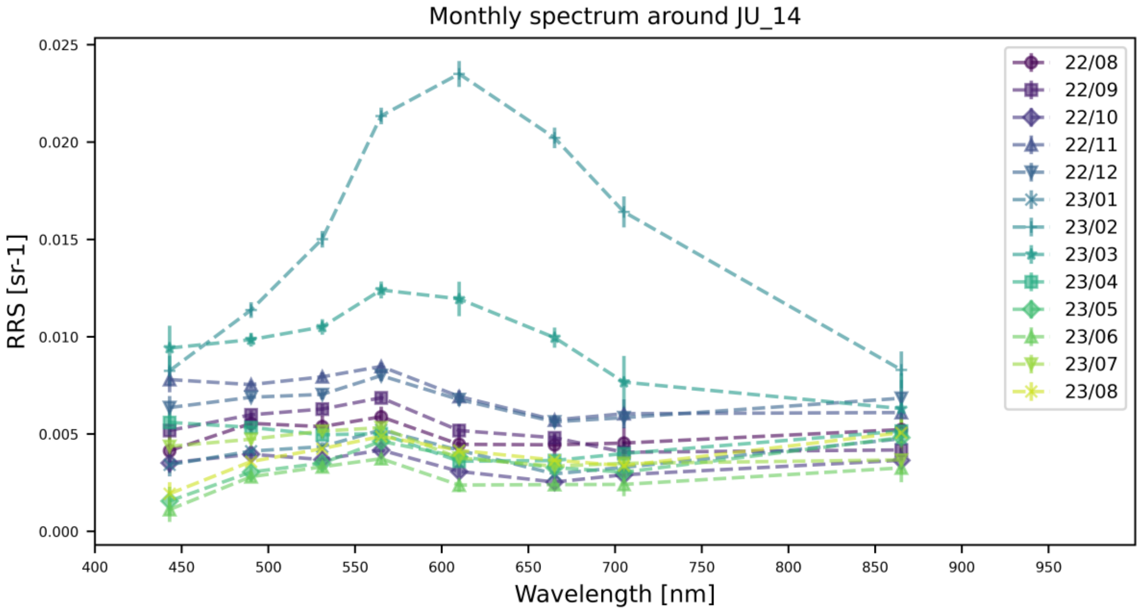

Figure 32: Spectral profiles around JU_14 from for each month between August 2022 to August 2023 for a 30 by 30 m area around the in-situ station.

Figure 33 shows the spectral profiles of the three consecutive days for the four defined AOIs. The comparison is carried out under the assumption that differences due to the atmosphere or a change in the water body at the time of the image acquisition are negligible. Therefore, deviations in the derived R_{rs} from the satellite data are attributed to calibration or sensitivity of the respective instrument on board a SuperDove. While the spectral profiles for a land area and a patch of reeds at the western shore follow a similar trajectory, the signatures measured over water are more distinct.

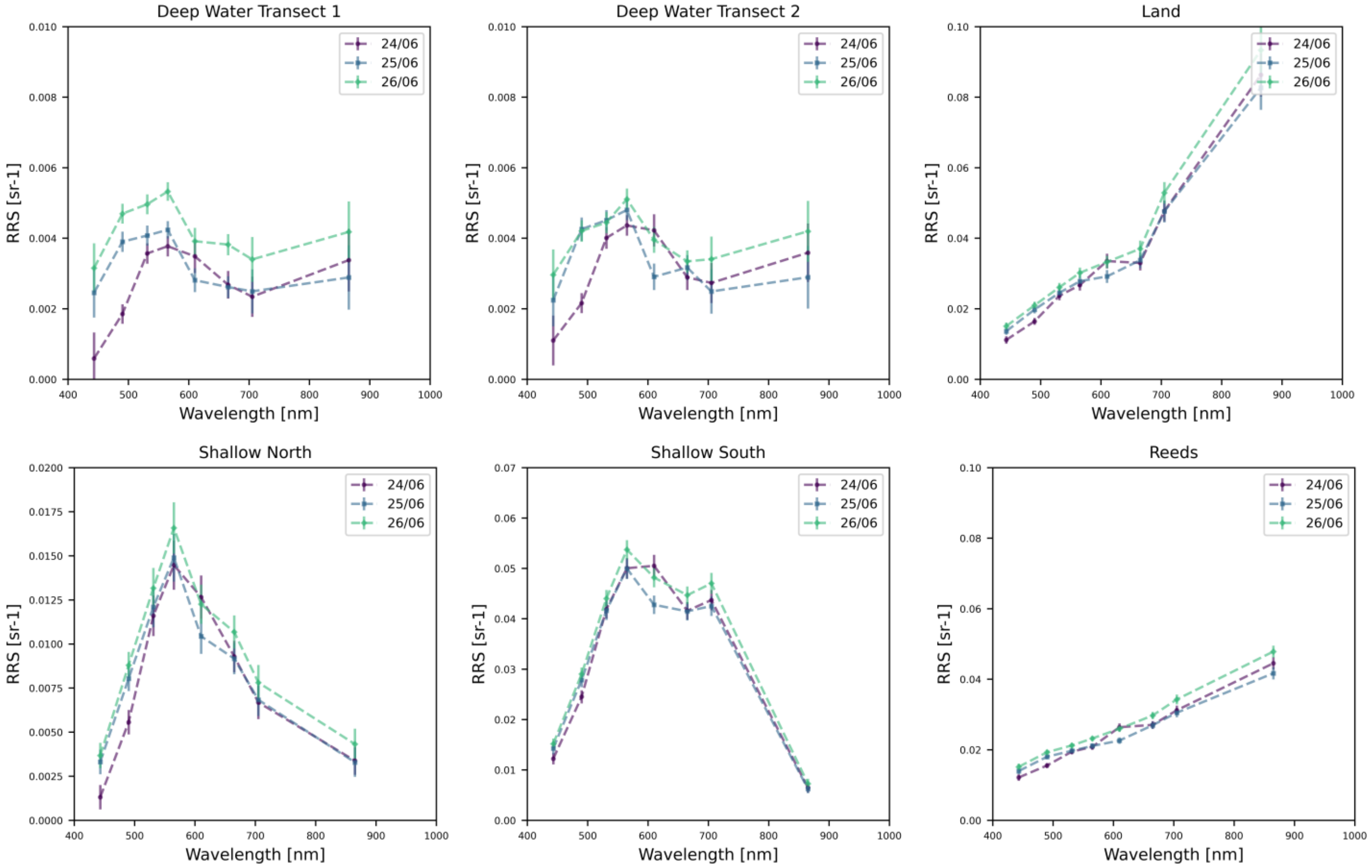

Figure 33: Spectral Profiles from SuperDove imagery on the 24th, 25th and 36th of June 2023. Vertical bars show standard deviation of pixel values within the AOI.

This difference in spectral signatures between images on different days is further illustrated through images of the calculated band indices and ratios. Figure 34 shows the NDCI and Figure 35 the NDWI. Water areas in Lake Junin are clearly distinguished from the surrounding land with negative values for the NDCI and positive values for the NDWI. Patterns on the water surface due to striping artifacts from the sensors are visible for all three days. The absolute difference between each image pairs is also oriented on these patterns over the Lake, while land surfaces show very little deviations. The rather flat peak in the spectrum shown in the profiles for the individual AOIs becomes even more apparent in Figure 36. Here, the ratio of the *Blue* to the *Yellow* band visualizes the diverging proportions of the signal between the three scenes. On the 24th, the *Yellow* band shows systematically greater R_{rs} than in the *Blue*. Images on the following two days show a similar signal in both bands (image from the 26th) or larger reflectance in the *Blue* (image from the 25th), which agrees with the spectra from the individual AOIs from Figure 33. These images suggest a more general problem with the consistency between images from consecutive overpasses as differences between band ratios are less sensitive to a change in atmosphere. While uncertainties are difficult to attribute to a single sensor, it is apparent that the instrument on the SuperDove (Unit ID 2426) from the 24th seems to be subject to calibration issues. This was investigated for a PICS site for the salt flats in Bonneville, Utah. From five SuperDove overpasses within nine days, unit 2426 also showed reflectance peaks in the *Yellow* band, deviating from the general spectral profile. This supports the assumption that the general performance or calibration of that instrument is deteriorated. The same analysis for the salt flats was also investigated for Sentinel-2A and Sentinel-2B over 20 days where the salt flats are assumed to be constant in time. Here, much less variability was observed between the four images and the spectral profile seemed to only be impacted by atmospheric condition on one day (see Figure 42 and Figure 43 in the Appendix).

Table 11 summarizes the percent differences between the three scenes from the mean reflectance in each band. These uncertainties are indicative of the relative performance for satellite derived R_{rs} at Lake Junin for data that is assumed to be acquired under stable environmental conditions between satellite overpasses. The errors do not yet imply calibration differences. For this, differences in band ratios are more conclusive as shown in Figure 36 for the *Blue* and *Yellow* band.

Table 11: Band wise percentage differences from mean Rrs between days for a respective AOI.

AOI	Date	Band 1	Band 2	Band 3	Band 4	Band 5	Band 6	Band 7	Band 8
Deep Water 1	Mean R_{rs} [sr^{-1}]	0.002	0.003	0.004	0.004	0.003	0.003	0.003	0.003
	24.06.23	**-71.4**	**-46.8**	**-15.1**	-15.1	2.4	-11.8	-14.7	-3.0
	25.06.23	18.9	12.0	-3.0	-4.6	-17.4	-13.9	-9.2	-17.1
	26.06.23	52.5	34.8	18.1	**19.8**	15.0	**25.7**	**23.8**	**20.0**
Deep Water 2	Mean R_{rs} [sr^{-1}]	0.002	0.004	0.004	0.005	0.004	0.003	0.003	0.004
	24.06.23	-47.6	-39.0	-7.2	-8.3	14.3	-7.8	-5.0	0.8
	25.06.23	6.7	20.3	4.4	0.9	**-21.3**	1.1	-13.4	-18.7
	26.06.23	40.9	18.8	2.9	7.4	7.0	6.7	18.4	17.9
Shallow North	Mean R_{rs} [sr^{-1}]	0.003	0.007	0.012	0.015	0.012	0.010	0.007	0.004
	24.06.23	-52.4	-25.4	-5.6	-5.5	7.4	-4.3	-6.0	-7.8
	25.06.23	19.7	7.6	-1.5	-2.7	-11.4	-5.6	-3.9	-10.2
	26.06.23	32.7	17.8	7.1	8.3	4.0	9.9	9.9	18.0
Shallow South	Mean R_{rs} [sr^{-1}]	0.014	0.027	0.042	0.051	0.047	0.043	0.044	0.007
	24.06.23	-12.1	-9.7	-1.5	-2.4	7.1	-2.3	-1.6	-2.8
	25.06.23	2.8	2.7	-2.1	-2.5	-9.3	-2.6	-4.3	-6.4
	26.06.23	9.3	6.9	3.6	4.9	2.2	4.9	5.9	9.2

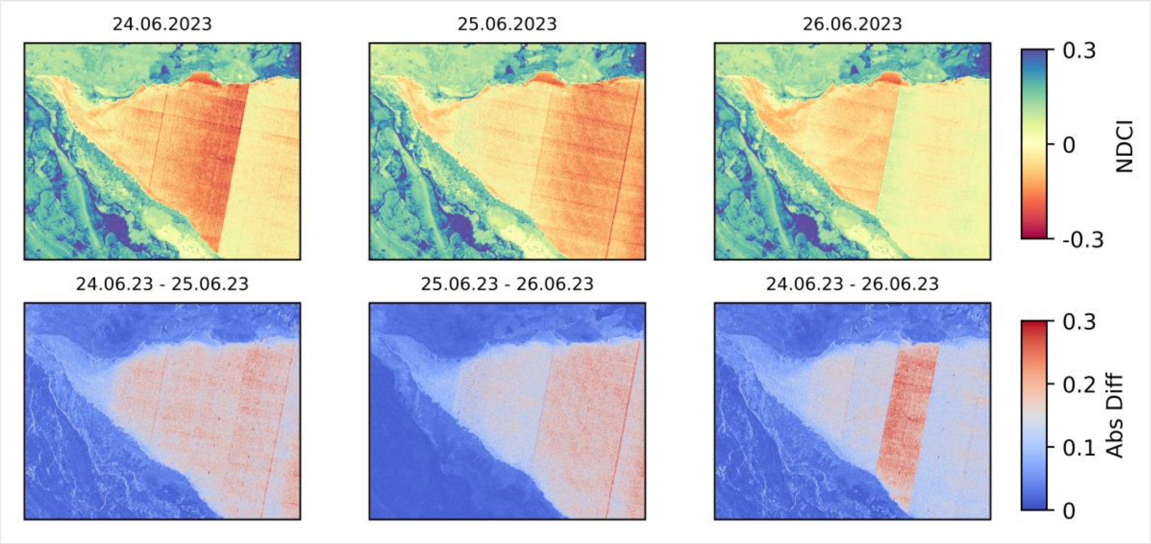

Figure 34: NDCI and absolute differences of the index between SuperDove images

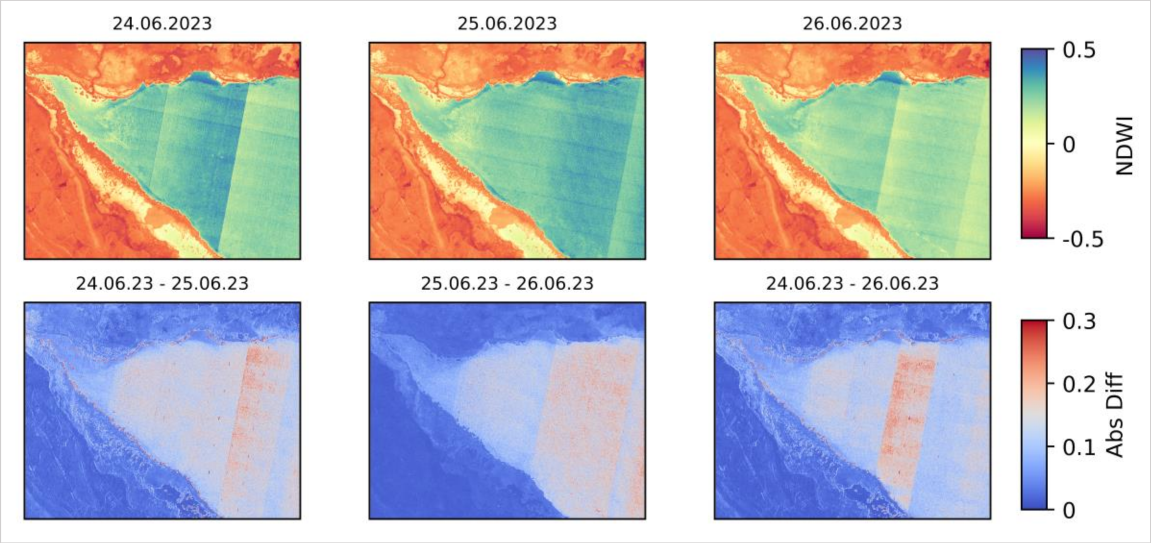

Figure 35: NDWI and absolute differences of the index between SuperDove images.

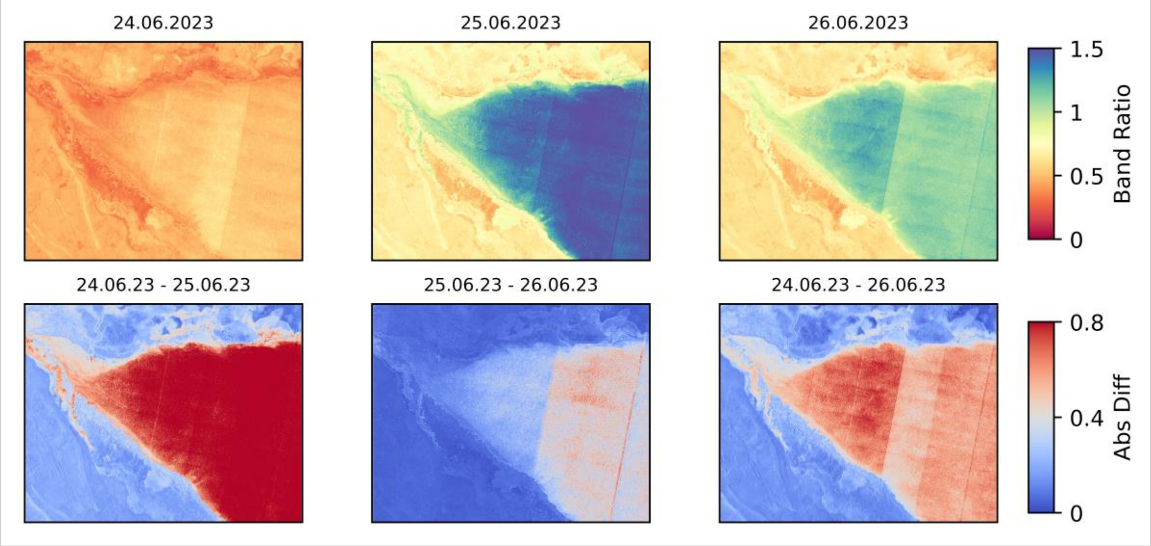

Figure 36: Blue to Yellow Band Ratio and absolute differences of the ratio between SuperDove images

4.6. Uncertainties of satellite derived R_{rs}

Figure 36 shows the scatter plots of satellite derived R_{rs} after minimal user settings in ACOLITE and in-situ measured R_{rs} after glint correction in WASI. Regression line, R^2 as the measure of the linear regression fit and RMSE are included in the plot, however calculated without the NIR band for the SuperDove images. Points are colour coded according to the individual bands. The optically shallow points are generally more dispersed and dependent on the bottom reflectance and show higher R_{rs}, while the points along the transects show lower variability in R_{rs}. Best results between in-situ data and satellite derived R_{rs} were observed for the Sentinel-2B scene from the 24th of June with an R^2 value of 0.96 and a RMSE of 0.00026 sr^{-1} for all bands. The SuperDove image from the same day had high agreement in the *Coastal Blue* and *Blue* band, but the instrument specific performance errors are highlighted once again. While the scenes on the 25th and 26th align well with the in-situ measurements by applying an offset for all bands, the distribution of the band specific points on the 24th suggest a better explanation through two linear models. This leads to the largest RMSE for the first scene (0.0092 sr^{-1}), with lower errors on the following days (around 0.0005 sr^{-1}).

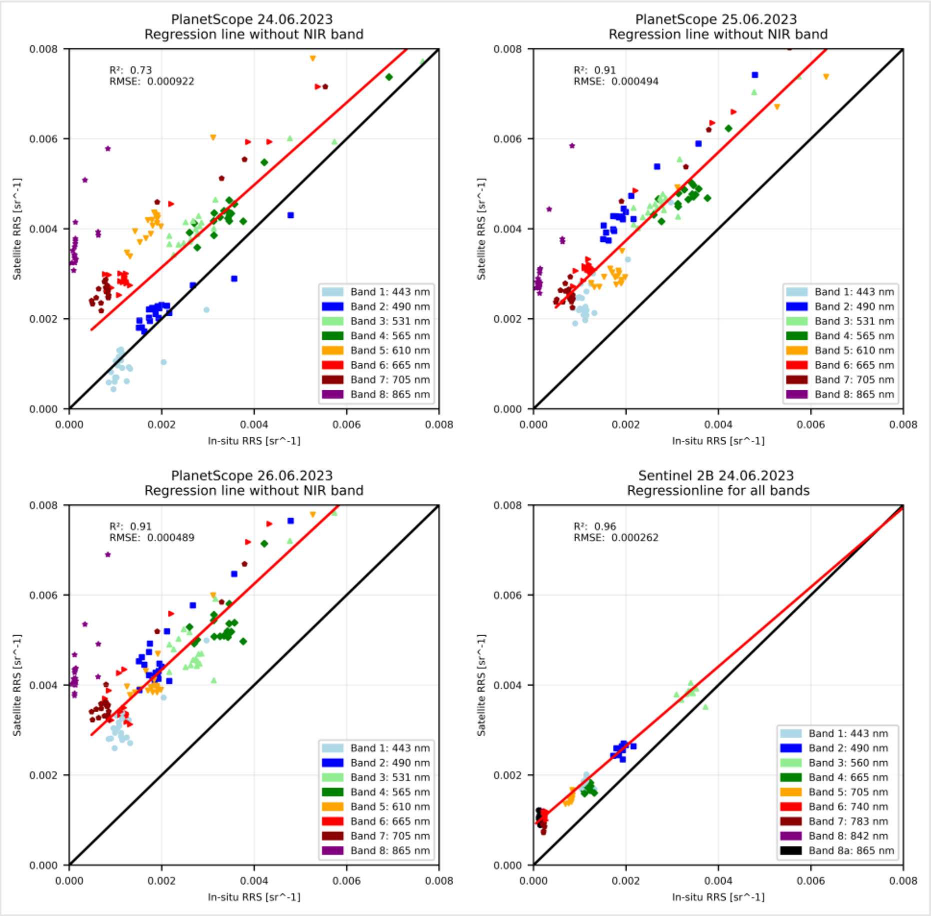

Figure 37: Scatter Plot for all in-situ water spectra. Three consecutive overpasses for PlanetScope with the regression line as well as R² and RMSE for points JU_20 - JU_30 and without the NIR band.

Accuracy statistics for band specific errors are provided in Table 12. The accuracy for the linear regression improves with lower temporal offset between the in-situ measurement and the satellite overpass.

Further, the satellite derived reflectance in the NIR from the SuperDoves were not representative of a typical water spectrum in which NIR is absorbed stronger than visible light and the signal is approaching zero in optically deep water. While this is accurate for the Sentinel-2B image, NIR R_{rs} for SuperDoves was systematically higher than in the *Red-Edge*, as can be seen in Figure 36. The percentage error in Table 12 between in-situ and satellite derived R_{rs} is therefore also the highest in the NIR band. Given the weak performance of the NIR band from all three SuperDove instruments, the fit range in WASI is proposed to be set to exclude this band in addition to the *Coastal Blue* band.

Table 12: Accuracy statistics for the band wise linear regression model between In-situ Rrs and satellite derived Rrs. Mean percentage as directional error between measurement and satellite for actual values

Date	Error	Band 1	Band 2	Band 3	Band 4	Band 5	Band 6	Band 7	Band 8
24.06.23	RMSE [sr-1]	0.00026	0.00015	0.00022	0.00025	0.00022	0.00024	0.00025	0.00043
	R^2	0.53	0.92	0.95	0.97	0.98	0.97	0.96	0.55
	MPE [%]	-17	11	44	25	119	144	219	>2000
25.06.23	RMSE [sr-1]	0.00027	0.00016	0.00026	0.00027	0.00025	0.00019	0.00025	0.00036
	R^2	0.79	0.96	0.96	0.98	0.98	0.98	0.97	0.77
	MPE [%]	112	122	66	40	64	157	220	>2000
26.06.23	RMSE [sr-1]	0.00023	0.00035	0.00046	0.00040	0.00028	0.00044	0.00023	0.00044
	R^2	0.80	0.85	0.89	0.95	0.97	0.93	0.97	0.58
	MPE [%]	170	135	74	56	119	203	327	>3000

4.7. Accuracy of fits for representative spectra from SuperDove

Processing SuperDove imagery in WASI, both for the deep water and shallow water model, did not lead to satisfactory results. During initialization of fit parameters for the deep-water inversion, large differences between the measurement and the simulated spectrum could be observed: For example, the flat peak composed of the *Green I* and *Green II* bands and the *Yellow* band in the deep water AOIs could not be replicated with sensible model initialization. Figure 38 shows measurements from a deep water AOI and their respective fits for all bands. Additionally, improvements from a fit set for wavelengths between 450 nm and 750 nm, to avoid fitting the *Coastal Blue* and *NIR* band are shown on the right subplot. The deep-water inversion was fitted for CDOM, NAP and chlorophyll-a concentration with green algae as the dominant species as well as the fraction of sky radiance due to direct solar radiation. When a fit is set for the full wavelength range of a SuperDove sensor, residuals between fit curve and measurement were 5.199E-4. Chlorophyll-a concentration was determined at 68 µg/l and outside plausible concentrations based on the in-situ measurements. When the fit range was set to 450 – 750 nm, the residual between the curves reduced to 2.498E-4 and chlorophyll-a concentration was determined at 20 µg/l.

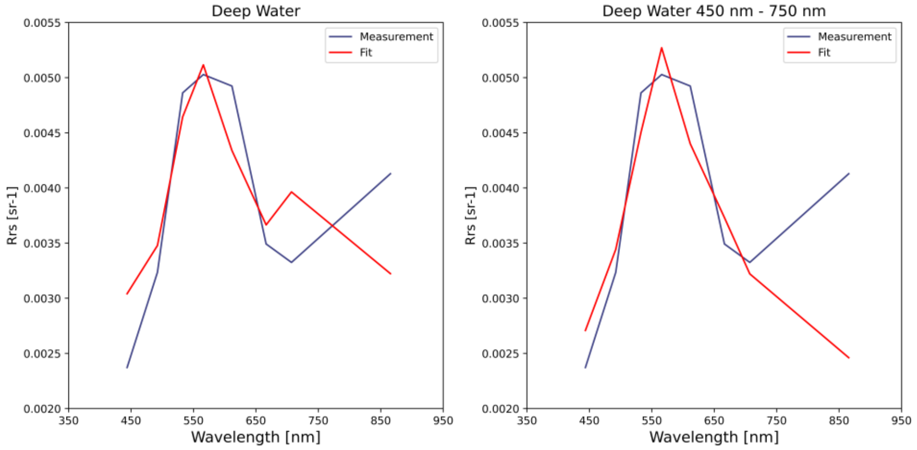

Figure 38: Rrs spectrum from SuperDove and fit curve from WASI for all eight bands (Left) and a wavelength range between 450 nm and 750 nm (Right)

Pre-fit analysis of the deep-water areas at Lake Junin with all three SuperDove images available during the field campaign ultimately determined model initialization with the data as inadequate for the deep-water inversion. Shallow water spectra could be fitted with satisfactory residuals between simulated and satellite derived R_{rs} for the AOI in the north and the south. However, the determination of chlorophyll-a concentration and water depth for the entire image were not plausible regardless of a good initial fit and were biased towards the training area. The spectral ambiguities could not be resolved accurately, and very heterogeneous shallow water areas found at Lake Junin likely require individual model initialization.

5. Discussion

Different parametrization in ACOLITE had no significant impact on spectral profiles for satellite derived R_{rs} and accompanying challenges to derive Level-3 parameters at Lake Junin. However, the initialization with a different ROI size was shown to possibly alter the derived R_{rs}. Yet no decisive conclusion about the ROI selection can be made, as larger or smaller ROIs shifted the signal in different directions for imagery from different SuperDoves or had no impact at all. Change in spectral signatures through the use of ancillary data for gas transmittance and atmospheric pressure resulted in only minimal differences in reflectance and is in accordance with results from studies at other test sites (Vanhellemont, 2023). Images did not seem to be strongly affected by glint effects. Tests with both glint correction methods implemented in ACOLITE resulted in a worse determination of R_{rs} with negative values for the alternative correction method and slightly higher R_{rs} for the default glint correction method, increasing the error to in-situ spectra. As users are recommended to define minimal settings in ACOLITE, results in this thesis were thus presented for settings where only the ROI and the elevation was defined. For the latter, it is essential to consider changes in atmospheric pressure at high altitude lakes, as both the surface reflectance product from PlanetLabs and atmospheric correction with ACOLITE for normal pressure overestimate the path radiance and led to larger errors in derived R_{rs},

In this study, differences in satellite derived R_{rs} from SuperDove instruments assumed a stable atmosphere and no change in the composition of the water body that impact the measured signal. While this provided a first overview of the uncertainties between them, comparisons should always be done with identical atmospheric parameters for all scenes. By visualizing differences between band ratios, as was done with the *Blue and Yellow* ratio, band specific performance becomes more apparent. Ultimately, calibration issues for a SuperDove instrument are assumed based on the performance from consecutive overpasses both at Lake Junin and a PICS site. No method was employed to correct for instrument specific performance and uncertainties were quantified as percentage differences from the mean reflectance of only the three satellite images. This showed the variation in the signal for each band, but not yet the accuracy of the measured R_{rs} itself. For this, the validation of the satellite derived R_{rs} with in-situ measurements was presented. Here, relative performance was best for the image taken on the 24th as the reflectance values were closer to the ground-truth data yet deviated more from the assumptions of a linear model. R_{rs} on the following days showed more linearity to the in-situ measurements and could be improved by an adequate offset.

Drawing conclusions based on a small subset of three images is also only partially representative of possible applications. Future investigations of SuperDove imagery should ideally evaluate the performance systematically across the constellation. For this, time series analysis of all sensors and between overpasses of the same satellite could be analysed and compared for water bodies with different optical properties. This may further help identifying uncertainties and limitations for aquatic remote sensing.

Finally, the difficulties in simulating deep water spectra from SuperDove imagery led to the rejection of the data for the deep-water model implemented in WASI. When water constituents and water depth were modelled with the AI module in WASI for shallow water, the resulting maps for the fit parameters were within unrealistic ranges, biased to sensor artifacts and training area and showed low agreement between the AI module and the physics-based inversion for validation pixels. Improvements could be achieved by processing distinct shallow water areas with specific model initializations and respective bottom types separately. Individual results with the best accuracy to map depth and constituent concentration could then be combined to provide a full coverage of Lake Junin.

Since the four band Dove imagery from the Planet constellation has shown good results for water depth and water constituent retrieval in the study by Niroumand-Jadidi et al. (2020), another adjustment to the SuperDove imagery could be the exclusion of the novel bands or bands that are not directly calibrated with Sentinel-2, as well as the NIR band. This can be implemented rather easy since single band raster can be output from ACOLITE in *geotiff* format and then be stacked in the GIS with only the desired bands. A reduction in available bands however also demands a reduction in fit parameters to avoid overfitting. A first approach with the five shared bands with Sentinel-2, disregarding the NIR band, showed very good agreement for representative spectra during the model initialization. However, only within unplausible parameter ranges and the determination of water depth and chlorophyll-a concentration based on the image data continued to show very low agreement with in-situ data.

Figure 39 shows results from WASI-AI for water depths above two meters and five meters through the inverse modelling of the Sentinel-2B scene. For this, the validation raster for the water depth, adjusted for field measurements, was added to the image as a masking band. The image was processed with the deep-water module, not accounting for any bottom signal, and fit for chlorophyll-a, with phytoplankton as the dominant species, as well as NAP, CDOM and sky glint. The parameters derived from the satellite image are compared to the parameters that were derived from the inverse-modelling of the field spectrometer data. Low agreement in the concentration of chlorophyll-a can be observed (RMSE: 2.66 ug/l, RMSE between IMARPE and modelled in-situ concentration: 0.31 ug/l). Better agreement is found for the concentrations of NAP (C_X) and CDOM (C_Y), with lower RMSE (0.25 mg/l and 0.10 1/m) for both when the image is processed for depths with 2 meter and below. Figure 40 and Figure 41 show the results from WASI-AI for the Sentinel-2B image as a thematic map for the areas at Lake Junin where water is deeper than 2-meter. Further, regional adaptation through the implementation of regional bottom types have been tested by Schmid 2024 for the satellite data and in-situ R_{rs} measurements from the field campaign. Here, first improvements for water depth determination with the spectrometer measurements have been demonstrated. However, scaling the methodology to the satellite image has not yet been optimized. This once again confirms the complexity of the challenges for accurate water depth retrieval, even when including a thoroughly developed spectral database for a region.

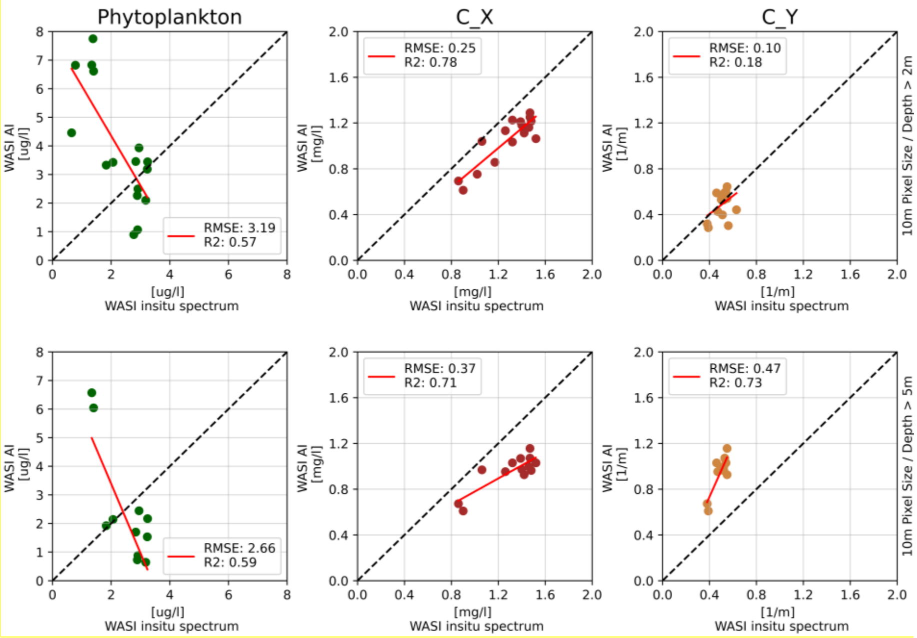

Figure 39: Modell comparison between inversion of in-situ measurement and inversion of the satellite image. Image best resutls were derived from WASI-AI and empirically set starting parameter and ranges

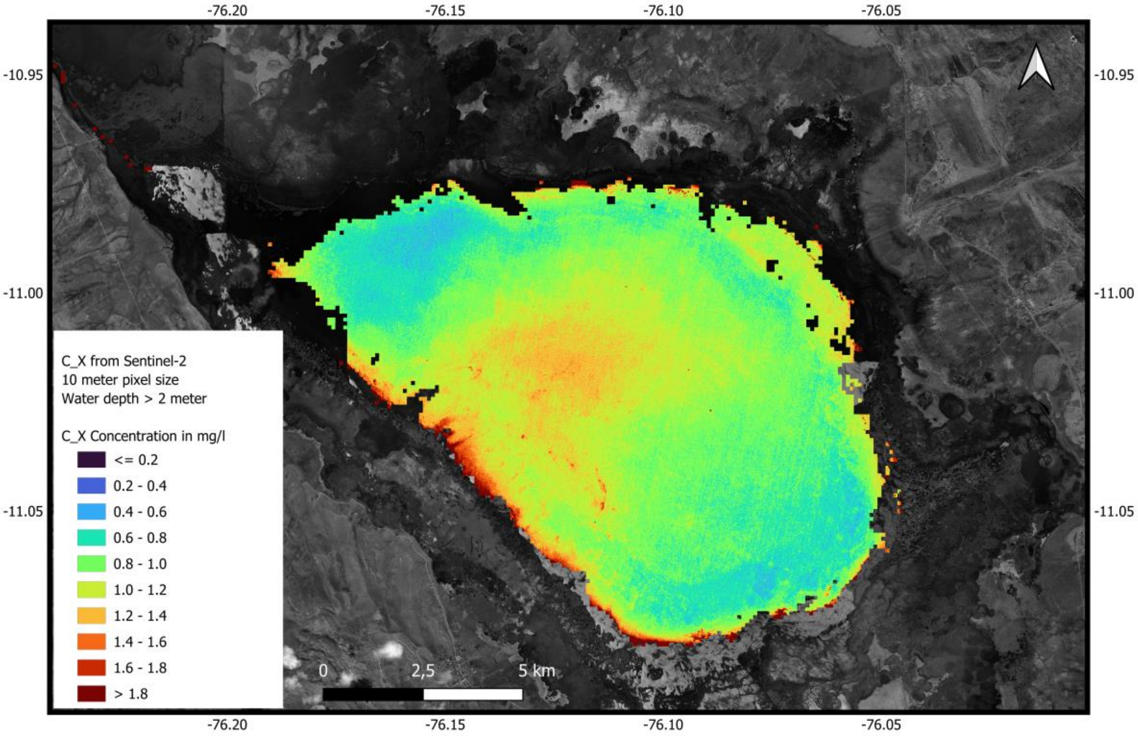

Figure 40: Thematic map of NAP concentration from a Sentinel-2B image. Image results derived from WASI-AI

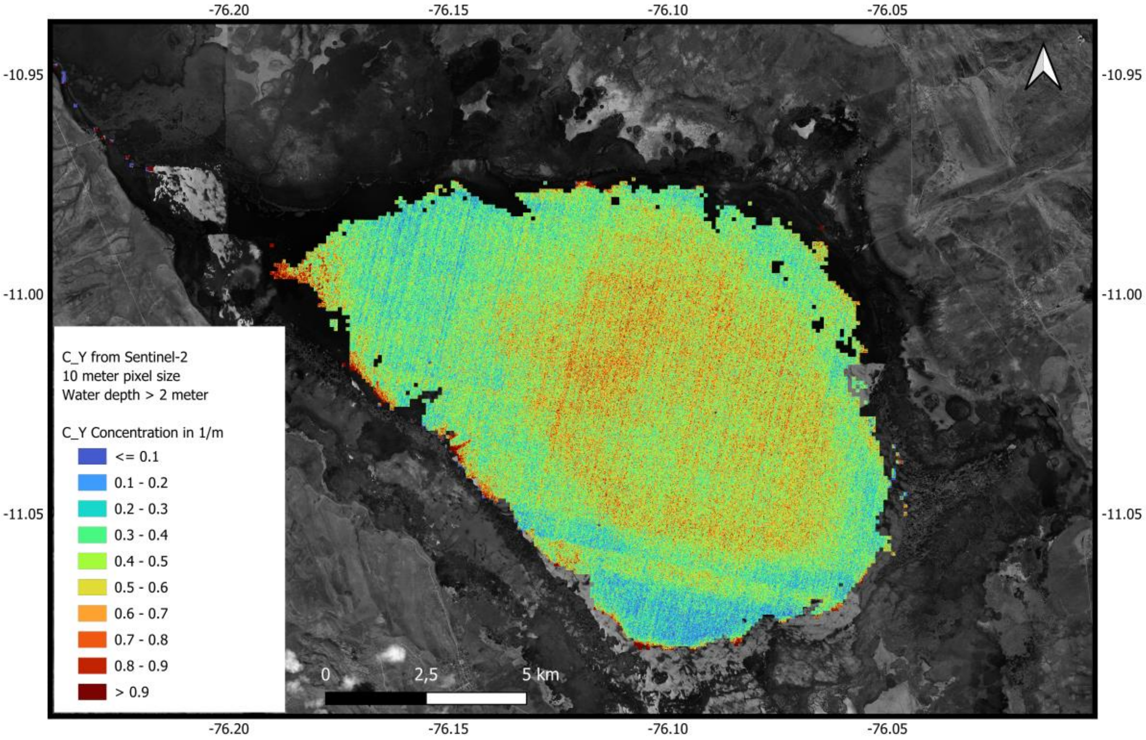

Figure 41: Thematic map of CDOM concentration from a Sentinel-2B image. Image results derived from WASI-AI.

6. Conclusion

In this thesis, the suitability of PlanetScope SuperDove satellite data has been explored for bathymetry and determination of chlorophyll-a concentration at Lake Junin. For this, the collection of validation data from in-situ measurements during a field campaign in June 2023 is documented and validation datasets for water depth, chlorophyll-a concentration and remote sensing reflectance have been obtained. These datasets are essential for assessing the accuracy of the reflectance derived from a satellite image and the inversely modelled Level-3 parameters in the software WASI. During the field campaign, three cloud-free images from different SuperDove satellites from the PlanetScope constellation were available. The imagery was assessed based on the band specific signal-to-noise ratio, sensitivity to parametrization in the atmospheric correction algorithm implemented in ACOLITE, and the consistency between consecutive overpasses. Despite the promising features of high temporal and spatial resolution, challenges outlined in this thesis made reliable image results in WASI difficult to obtain. Above all, these difficulties are attributed to the strong distortion of water spectra when these were derived from a SuperDove image. Additionally, inconsistencies in measured reflectance between SuperDove sensors showed low comparability between the satellite data and accuracy of the derived R_{rs} was lower than for a Sentinel-2B scene from the same day. Here, a database of unit-specific issues from the providers would be of great benefit to the scientific community. If available, this would allow researchers to either only consider well calibrated instruments for their applications or develop correction methods for potential calibration issues. Ultimately, SuperDove imagery has been rated as inadequate for bathymetry and the determination of chlorophyll-a concentration with the methodology proposed in this analysis. To further assess the potential of SuperDove imagery for aquatic remote sensing, future research should investigate the suitability of the presented methodology over brighter waters with a homogenous bottom. Regional adaptation in WASI through the inclusion of a spectral database for common bottom types showed promising results for field spectrometer measurements and should be maintained for all further analysis. The analysis highlights the complexity of the signal originating from a water surface and the variability that must be considered for the retrieval of specific parameters.

Appendix

Table 13: Overview of all In-situ measurements at Lake Junin

Date	Station	Latitude [deg°]	Longitude [deg°]	Chl-a IMARPE [ug/l]	Sediment Sample	Depth Tape [m]	Depth Sonar [m]	Secchi depth [m]	Cloud Cover
26.06.2023	JU_01	-10.9719	-76.2167	0.8	Yes	1.3	1.1	> depth	1
26.06.2023	JU_02	-10.9797	-76.2028	0.4	Yes	1.1	-	> depth	1
26.06.2023	JU_03	-10.9860	-76.1914	0.3	Yes	1.2	1.5	> depth	1
26.06.2023	JU_04	-10.9950	-76.1974	0.7	Yes	1.4	1.7	> depth	1
27.06.2023	JU_10	-11.0185	-76.173	1.9	Yes	0.6	0.8	> depth	4
27.06.2023	JU_11	-11.0180	-76.1730	1.9	Yes	1.6	2.2	> depth	0
27.06.2023	JU_12	-11.0124	-76.170	1.2	No	2.6	3.3	> depth	0
27.06.2023	JU_13	-11.0078	-76.1678	-	Yes	4.3	4.7	> depth	0
27.06.2023	JU_14	-10.9991	-76.1641	-	No	5.3	5.9	> depth	0
27.06.2023	JU_15	-10.9876	-76.1592	0.9	Yes	5.3	5.7	> depth	0
27.06.2023	JU_16	-10.9818	-76.157	-	No	2.8	3.2	> depth	0
27.06.2023	JU_17	-10.9773	-76.1563	0.6	No	1.8	2.4	> depth	0
27.06.2023	JU_18	-10.9809	-76.1738	0.9	No	1.7	-	> depth	0
27.06.2023	JU_19	-10.9647	-76.2276	1.0	Yes	-	2.5	1.4	2
28.06.2023	JU_20	-10.9944	-76.110	1.0	No	6.7	6.9	4.0	7
28.06.2023	JU_21	-10.9987	-76.1117	-	No	7.5	7.7	4.6	4
28.06.2023	JU_22	-11.0038	-76.1135	2.0	No	8.1	8.3	4.1	3
28.06.2023	JU_23	-11.0088	-76.1157	-	No	9.1	9.2	4.2	3
28.06.2023	JU_24	-11.0134	-76.117	2.2	No	9.1	9.2	4	1
28.06.2023	JU_25	-11.0174	-76.1183	-	No	10.7	10.9	4.4	1
28.06.2023	JU_26	-11.0216	-76.1198	-	No	8.3	8.5	4.4	1
28.06.2023	JU_27	-11.0261	-76.1216	1.6	No	8	8.1	4.4	1
28.06.2023	JU_28	-11.0306	-76.1234	-	No	7.7	7.9	3.9	0
28.06.2023	JU_29	-11.0350	-76.1250	1.2	No	6.8	7.2	3.7	0
28.06.2023	JU_30	-11.0304	-76.1384	0.4	No	5.1	5.3	4.6	0

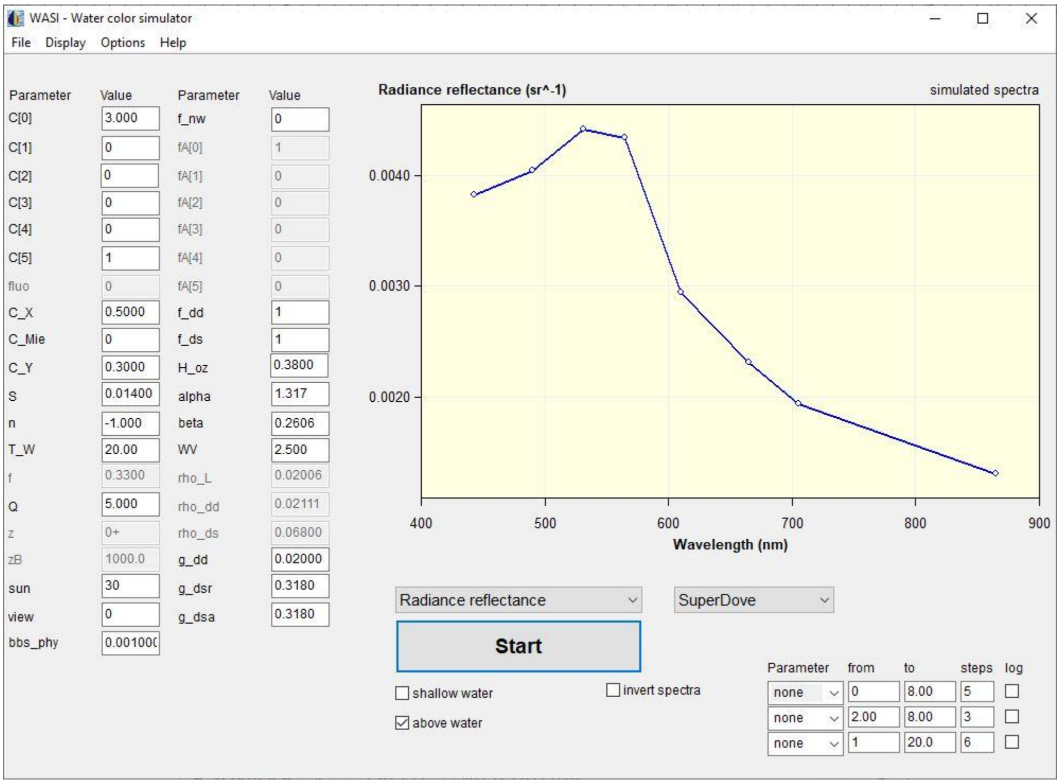

Parameter	Value	Parameter	Value
C[0]	3.000	f_nw	0
C[1]	0	fA[0]	1
C[2]	0	fA[1]	0
C[3]	0	fA[2]	0
C[4]	0	fA[3]	0
C[5]	1	fA[4]	0
fluo	0	fA[5]	0
C_X	0.5000	f_dd	1
C_Mie	0	f_ds	1
C_Y	0.3000	H_oz	0.3800
S	0.01400	alpha	1.317
n	-1.000	beta	0.2606
T_W	20.00	WV	2.500
f	0.3300	rho_L	0.02006
Q	5.000	rho_dd	0.02111
z	0+	rho_ds	0.06800
zB	1000.0	g_dd	0.02000
sun	30	g_dsr	0.3180
view	0	g_dsa	0.3180
bbs_phy	0.00100(		

Radiance reflectance

SuperDove

☐ shallow water
☑ above water
☐ invert spectra

Parameter	from	to	steps	log
none	0	8.00	5	☐
none	2.00	8.00	3	☐
none	1	20.0	6	☐

Figure 42: GUI of WASI with forward simulation of a spectra in optically shallow water convoluted to SuperDove central wavelength.

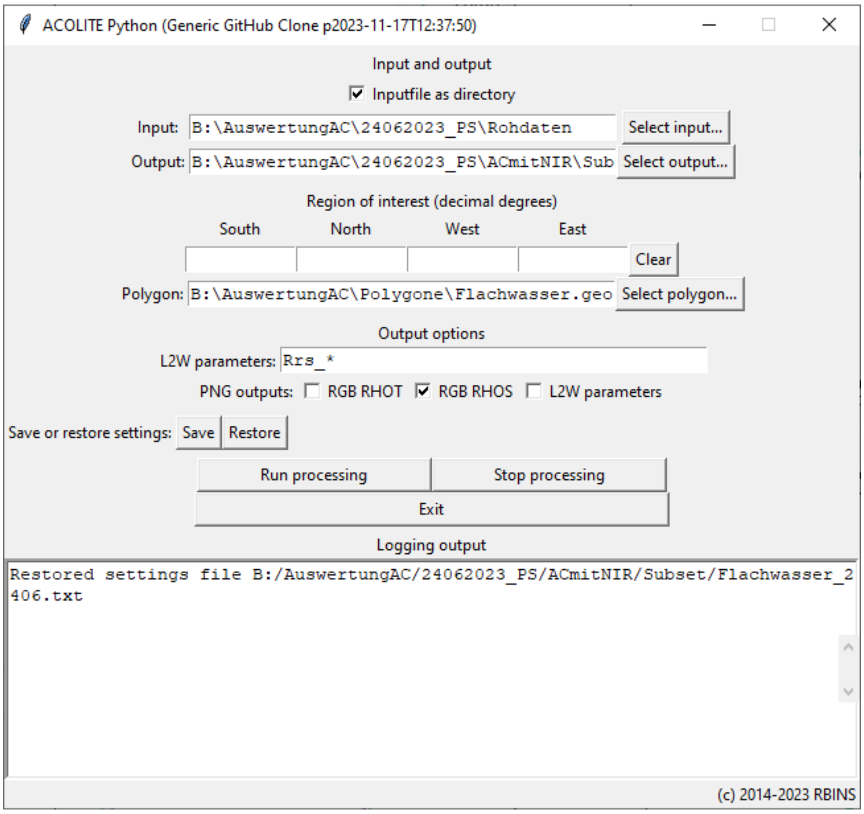

☑ Inputfile as directory

Input: B:\AuswertungAC\24062023_PS\Rohdaten

Output: B:\AuswertungAC\24062023_PS\ACmitNIR\Sub

Polygon: B:\AuswertungAC\Polygone\Flachwasser.geo

L2W parameters: Rrs_*

PNG outputs: ☐ RGB RHOT ☑ RGB RHOS ☐ L2W parameters

```
Restored settings file B:/AuswertungAC/24062023_PS/ACmitNIR/Subset/Flachwasser_2
406.txt
```

Figure 43: GUI of ACOLITE with a selected ROI in the Polygon tab and remote sensing reflectance selected as a mappable output.

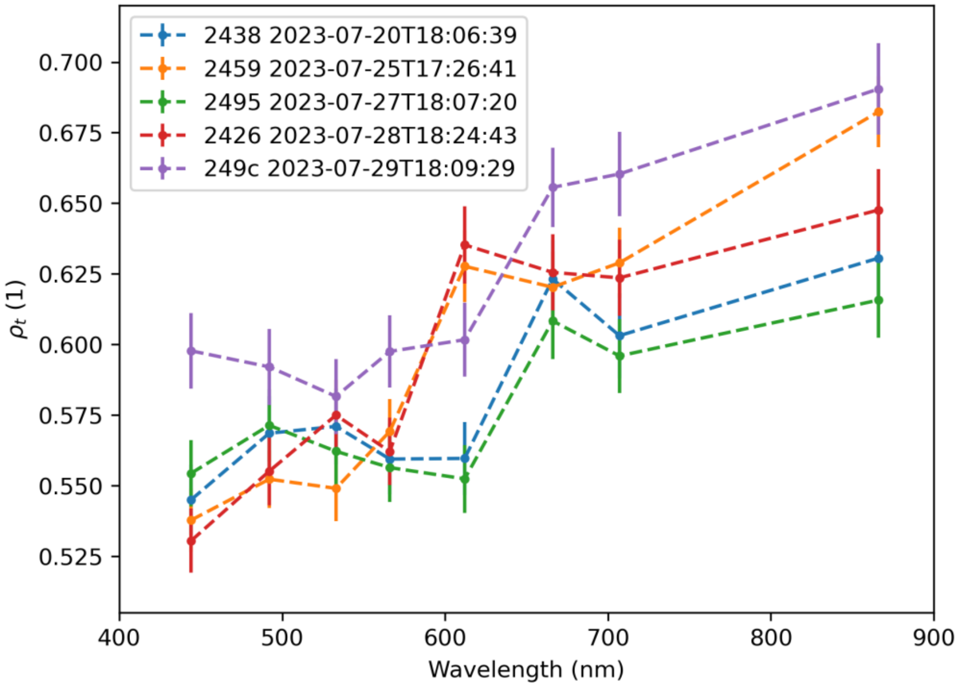

Figure 44: Comparison of spectral profiles from SuperDove overpasses over salt flats

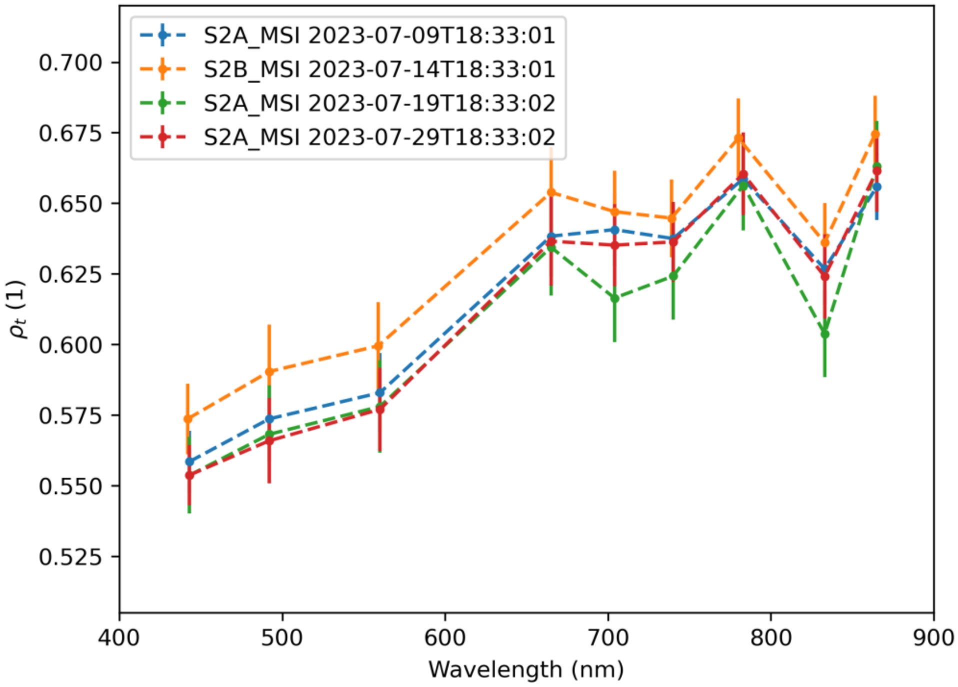

Figure 45: Comparison of spectral profiles from Sentinel-2 overpasses over salt flats

References

ACOLITE (2024). ACOLITE Forum. https://odnature.naturalsciences.be/remsem/acolite-forum/app.php/help/faq.

Alikas, K., & Kratzer, S. (2017). Improved retrieval of Secchi depth for optically-complex waters using remote sensing data. *Ecological Indicators*, *77*, 218–227.

Apostolaki, S., Koundouri, P., & Pittis, N. (2019). Using a systemic approach to address the requirement for Integrated Water Resource Management within the Water Framework Directive. *The Science of the total environment*, *679*, 70–79.

Astha Gautam, & Naina Mehta (2015). *A Review on Remote Sensing Technique: Concept and Principles*.

Basith, A., Nuha, M.U., Prastyani, R., & Winarso, G. (2019). Aerosol optical depth (AOD) retrieval for atmospheric correction in Landsat-8 imagery using second simulation of a satellite signal in the solar spectrum-vector (6SV). *Communications in Science and Technology*, *4*, 68–73.

Berk, A., Conforti, P., Kennett, R., Perkins, T., Hawes, F., & van den Bosch, J. (2014). MODTRAN6: a major upgrade of the MODTRAN radiative transfer code. In M. Velez-Reyes, & F.A. Kruse (Eds.), *Algorithms and Technologies for Multispectral, Hyperspectral, and Ultraspectral Imagery XX* (90880H): SPIE.

Berkes, F. (2010). Devolution of environment and resources governance: trends and future. *Environmental Conservation*, *37*, 489–500.

Bouvet, M., Thome, K., Berthelot, B., Bialek, A., Czapla-Myers, J., Fox, N., Goryl, P., Henry, P., Ma, L., Marcq, S., Meygret, A., Wenny, B., & Woolliams, E. (2019). RadCalNet: A Radiometric Calibration Network for Earth Observing Imagers Operating in the Visible to Shortwave Infrared Spectral Range. *Remote Sensing*, *11*, 2401.

Braga, F., Fabbretto, A., Vanhellemont, Q., Bresciani, M., Giardino, C., Scarpa, G.M., Manfè, G., Concha, J.A., & Brando, V.E. (2022). Assessment of PRISMA water reflectance using autonomous hyperspectral radiometry. *ISPRS Journal of Photogrammetry and Remote Sensing*, *192*, 99–114.

Brewin, R., Ciavatta, S., Sathyendranath, S., Skákala, J., Bruggeman, J., Ford, D., & Platt, T. (2019). The Influence of Temperature and Community Structure on Light Absorption by Phytoplankton in the North Atlantic. *Sensors*, *19*, 4182.

Caballero, I., & Stumpf, R.P. (2020). Atmospheric correction for satellite-derived bathymetry in the Caribbean waters: from a single image to multi-temporal approaches using Sentinel-2A/B. *Optics express, 28*, 11742–11766.

Cesel (2022). Cesel. https://www.cesel.com.pe/.

Collin, A., Palola, P., James, D., Pastol, Y., Monpert, C., Loyer, S., Stoll, B., Feunteun, E., & Wedding, L. (2023). Superdove-modelled bathymetry using neural networks along a turbidity gradient: brehat, saint-barthelemy and tetiaroa islands. *The International Archives of the Photogrammetry, Remote Sensing and Spatial Information Sciences*, *XLVIII-1/W2-2023*, 1351–1356.

Correa, S.W., Mello, C.R., Chou, S.C., Curi, N., & Norton, L.D. (2016). Soil erosion risk associated with climate change at Mantaro River basin, Peruvian Andes. *CATENA*, *147*, 110–124.

Curtis, M., Jeremy, W., Bryan, F., Ziauddin, A., & Sean, B. (2016). *Atmospheric Correction for Satellite Ocean Color Radiometry:* Technical Report.

Custodio, M., Huaraca, F., Espinoza, C., & Cuadrado, W. (2019). Distribution and Accumulation of Heavy Metals in Surface Sediment of Lake Junín National Reserve, Peru. *Open Journal of Marine Science*, *09*, 33–48.

Czapla-Myers, J., McCorkel, J., Anderson, N., Thome, K., Biggar, S., Helder, D., Aaron, D., Leigh, L., & Mishra, N. (2015). The Ground-Based Absolute Radiometric Calibration of Landsat 8 OLI. *Remote Sensing*, *7*, 600–626.

Defoin-Platel, M., & Chami, M. (2007). How ambiguous is the inverse problem of ocean color in coastal waters? *Journal of Geophysical Research: Oceans*, *112*.

Dinesen, L., Chamorroa A, Fjeldsa, J., & AUCCA, C. (2019). Long-term declines in waterbirds abundance at Lake Junín, Andean Peru. *Bird Conservation International*, *29*, 83–99.

Dörnhöfer, K., & Oppelt, N. (2016). Remote sensing for lake research and monitoring – Recent advances. *Ecological Indicators*, *64*, 105–122.

Feng, L., Hou, X., Li, J., & Zheng, Y. (2018). Exploring the potential of Rayleigh-corrected reflectance in coastal and inland water applications: A simple aerosol correction method and its merits. *ISPRS Journal of Photogrammetry and Remote Sensing*, *146*, 52–64.

Gabr, B., Ahmed, M., & Marmoush, Y. (2020). PlanetScope and Landsat 8 Imageries for Bathymetry Mapping. *Journal of Marine Science and Engineering*, *8*, 143.

Gege, P. (2004). The water color simulator WASI: an integrating software tool for analysis and simulation of optical in situ spectra. *Computers & Geosciences*, *30*, 523–532.

Gege, P. (2014). WASI-2D: A software tool for regionally optimized analysis of imaging spectrometer data from deep and shallow waters. *Computers & Geosciences*, *62*, 208–215.

Gege, P., & Dekker, A.G. (2020). Spectral and Radiometric Measurement Requirements for Inland, Coastal and Reef Waters. *Remote Sensing*, *12*, 2247.

German, L., Mansoor, H., Alemu, G., Mazengia, W., Amede, T., & Stroud, A. (2007). Participatory integrated watershed management: Evolution of concepts and methods in an ecoregional program of the eastern African highlands. *Agricultural Systems*, *94*, 189–204.

Giz (2023). Climate-sensitive water resource management. https://www.giz.de/en/worldwide/110797.html.

Gonsamo, A., & Chen, J.M. (2013). Spectral Response Function Comparability Among 21 Satellite Sensors for Vegetation Monitoring. *IEEE Transactions on Geoscience and Remote Sensing*, *51*, 1319–1335.

Gordon, H.R., Brown, O.B., & Jacobs, M.M. (1975). Computed relationships between the inherent and apparent optical properties of a flat homogeneous ocean. *Applied optics*, *14*, 417–427.

Gordon, H.R., & Wang, M. (1994). Retrieval of water-leaving radiance and aerosol optical thickness over the oceans with SeaWiFS: a preliminary algorithm. *Applied optics*, *33*, 443–452.

Groom, S., Sathyendranath, S., Ban, Y., Bernard, S., Brewin, R., Brotas, V., Brockmann, C., Chauhan, P., Choi, J., Chuprin, A., Ciavatta, S., Cipollini, P., Donlon, C., Franz, B., He, X., Hirata, T., Jackson, T., Kampel, M., Krasemann, H., Lavender, S., Pardo-Martinez, S., Mélin, F., Platt, T., Santoleri, R., Skakala, J., Schaeffer, B., Smith, M., Steinmetz, F., Valente, A., & Wang, M. (2019). Satellite Ocean Colour: Current Status and Future Perspective. *Frontiers in Marine Science*, *6*, 1–30.

Gutierrez Ahumada, J., Doerksen, K., & Zeller, S. (2021). Automated Fleet Commissioning Workflows at Planet. *Small Satellite Conference*.

Hedley, J.D., Harborne, A.R., & Mumby, P.J. (2005). Technical note: Simple and robust removal of sun glint for mapping shallow-water benthos. *International Journal of Remote Sensing*, *26*, 2107–2112.

Helder, D., Anderson, C., Beckett, K., Houborg, R., Zuleta, I., Boccia, V., Clerc, S., Kuester, M., Markham, B., & Pagnutti, M. (2020). Observations and Recommendations for Coordinated Calibration Activities of Government and Commercial Optical Satellite Systems. *Remote Sensing*, *12*, 2468.

Huang, H., & Roy, D.P. (2021). Characterization of Planetscope-0 Planetscope-1 surface reflectance and normalized difference vegetation index continuity. *Science of Remote Sensing*, *3*, 100014.

Hubert Loisel, Vincent Vantrepotte, & Cédric Jamet and Dinh Ngoc Dat. Challenges and New Advances in Ocean Color Remote Sensing of Coastal Waters.

Ilori, C., Pahlevan, N., & Knudby, A. (2019). Analyzing Performances of Different Atmospheric Correction Techniques for Landsat 8: Application for Coastal Remote Sensing. *Remote Sensing*, *11*. https://www.mdpi.com/2072-4292/11/4/469.

Jorge, D., Barbosa, C., Carvalho, L. de, Affonso, A., Lobo, F., & Novo, E. (2017). SNR (Signal-To-Noise Ratio) Impact on Water Constituent Retrieval from Simulated Images of Optically Complex Amazon Lakes. *Remote Sensing*, *9*, 644.

Kay, S., Hedley, J., & Lavender, S. (2009). Sun Glint Correction of High and Low Spatial Resolution Images of Aquatic Scenes: a Review of Methods for Visible and Near-Infrared Wavelengths. *Remote Sensing*, *1*, 697–730.

Khadka, N., Teixeira Pinto, C., & Leigh, L. (2021). Detection of Change Points in Pseudo-Invariant Calibration Sites Time Series Using Multi-Sensor Satellite Imagery. *Remote Sensing*, *13*, 2079.

Kington, J., & Collison, A. (2022). Scene Level Normalization and Harmonization of Planet Dove Imagery. PlanetLabs.

Kutser, T., Vahtmäe, E., & Praks, J. (2009). A sun glint correction method for hyperspectral imagery containing areas with non-negligible water leaving NIR signal. *Remote Sensing of Environment*, *113*, 2267–2274.

Lazaro, M., & Serpa, C. (2006). Estudio de Plan de Manejo Ambiental de las Operaciones de Embalse y Desembalse del Lago Chinchycocha. CESEL Ingenieros.

Lee, C.B., Martin, L., Traganos, D., Antat, S., Baez, S.K., Cupidon, A., Faure, A., Harlay, J., Morgan, M., Mortimer, J.A., Reinartz, P., & Rowlands, G. (2023). Mapping the National Seagrass Extent in Seychelles Using PlanetScope NICFI Data. *Remote Sensing*, *15*, 4500.

Leigh, L., Pinto, C.T., & Kaewmanee, M. (2023). Method of Validating Satellite Surface Reflectance Product Using Empirical Line Method. *Remote Sensing*, *15*, 2240.

Leymarie, E., Doxaran, D., & Babin, M. (2010). Uncertainties associated to measurements of inherent optical properties in natural waters. *Applied optics*, *49*, 5415–5436.

Li, Z., Wei, J., Huang, X., & Xu, F. (2023). Laboratory Radiometric Calibration Technique of an Imaging System with Pixel-Level Adaptive Gain. *Sensors*, *23*, 2083.

Loayza Ramos, A. (2017). *Análisis de la dosificación de coagulantes por efectos de la turbidez en el tratamiento de agua potable de la Planta de SEDAM Huancayo:* Universidad Continental; PE.

Loisel, H., Vantrepotte, V., Jamet, C., & Dinh, g.D. (2013). Challenges and New Advances in Ocean Color Remote Sensing of Coastal Waters. In *Topics in Oceanography:* InTech.

Lyzenga, D.R., Malinas, N.P., & Tanis, F.J. (2006). Multispectral bathymetry using a simple physically based algorithm. *IEEE Transactions on Geoscience and Remote Sensing*, *44*, 2251–2259.

Maciel, F.P., & Pedocchi, F. (2022). Evaluation of ACOLITE atmospheric correction methods for Landsat-8 and Sentinel-2 in the Río de la Plata turbid coastal waters. *International Journal of Remote Sensing*, *43*, 215–240.

Manuel, A., Blanco, A.C., Tamondong, A.M., Jalbuena, R., Cabrera, O., & Gege, P. (2020). Optmization of bio-optical model parameters for turbid lake water quality estimation using Landsat 8 and WASI-2d. *The International Archives of the Photogrammetry, Remote Sensing and Spatial Information Sciences*, *XLII-3/W11*, 67–72.

Mark, B.G., French, A., Baraer, M., Carey, M., Bury, J., Young, K.R., Polk, M.H., Wigmore, O., Lagos, P., Crumley, R., McKenzie, J.M., & Lautz, L. (2017). Glacier loss and hydro-social risks in the Peruvian Andes. *Global and Planetary Change*, *159*, 61–76.

Melesse, A.M., Weng, Q., Thenkabail, P.S., & Senay, G.B. (2007). Remote Sensing Sensors and Applications in Environmental Resources Mapping and Modelling. *Sensors*, *7*, 3209–3241.

Mishra, S., & Mishra, D.R. (2012). Normalized difference chlorophyll index: A novel model for remote estimation of chlorophyll-a concentration in turbid productive waters. *Remote Sensing of Environment*, *117*, 394–406.

Mishra, V., Limaye, A.S., Muench, R.E., Cherrington, E.A., & Markert, K.N. (2020). Evaluating the performance of high-resolution satellite imagery in detecting ephemeral water bodies over West Africa. *International Journal of Applied Earth Observation and Geoinformation*, *93*, 102218.

Mobley, C.D. (1999). Estimation of the remote-sensing reflectance from above-surface measurements. *Applied optics*, *38*, 7442–7455.

Niroumand-Jadidi, M., & Bovolo, F. (2021). Water quality retrieval and algal bloom detection using high-resolution cubesat imagery. *ISPRS Annals of the Photogrammetry, Remote Sensing and Spatial Information Sciences*, *V-3-2021*, 191–195.

Niroumand-Jadidi, M., Legleiter, C.J., & Bovolo, F. (2022). River Bathymetry Retrieval From Landsat-9 Images Based on Neural Networks and Comparison to SuperDove and Sentinel-2. *IEEE Journal of Selected Topics in Applied Earth Observations and Remote Sensing*, *15*, 5250–5260.

Ocean Optics (2024). Ocean Optics Web Book. https://www.oceanopticsbook.info/view/atmospheric-correction/the-atmospheric-correction-problem.

Pahlevan, N., Mangin, A., Balasubramanian, S.V., Smith, B., Alikas, K., Arai, K., Barbosa, C., Bélanger, S., Binding, C., Bresciani, M., Giardino, C., Gurlin, D., Fan, Y., Harmel, T., Hunter, P., Ishikaza, J., Kratzer, S., Lehmann, M.K., Ligi, M., Ma, R., Martin-Lauzer, F.-R., Olmanson, L., Oppelt, N., Pan, Y., Peters, S., Reynaud, N., Sander de Carvalho, Lino A., Simis, S., Spyrakos, E., Steinmetz, F., Stelzer, K., Sterckx, S., Tormos, T., Tyler, A., Vanhellemont, Q., & Warren, M. (2021). ACIX-Aqua: A global assessment of atmospheric correction methods for Landsat-8 and Sentinel-2 over lakes, rivers, and coastal waters. *Remote Sensing of Environment*, *258*, 112366.

Palmer, S.C., Kutser, T., & Hunter, P.D. (2015). Remote sensing of inland waters: Challenges, progress and future directions. *Remote Sensing of Environment*, *157*, 1–8.

Pan, Y., Bélanger, S., & Huot, Y. (2022). Evaluation of Atmospheric Correction Algorithms over Lakes for High-Resolution Multispectral Imagery: Implications of Adjacency Effect. *Remote Sensing*, *14*, 2979.

Paulino, R.S., Martins, V.S., Novo, E.M., Maciel, D.A., Correia-Lima, D.L., Barbosa, C.C., Bonnet, M.P., & Uhde, A. (2023). A framework based on spectral similarity to estimate hydrological connectivity in Juruá River floodplain lakes using 3-m PlanetScope data. *Journal of Hydrology*, *625*, 130156.

Pereira-Sandoval, M., Ruescas, A., Urrego, P., Ruiz-Verdú, A., Delegido, J., Tenjo, C., Soria-Perpinyà, X., Vicente, E., Soria, J., & Moreno, J. (2019). Evaluation of Atmospheric Correction Algorithms over Spanish Inland Waters for Sentinel-2 Multi Spectral Imagery Data. *Remote Sensing*, *11*, 1469.

Popovici, R., Erwin, A., Ma, Z., Prokopy, L.S., Zanotti, L., Bocardo Delgado, E.F., Pinto Cáceres, J.P., Zeballos Zeballos, E., Salas O'Brien, E.P., Bowling, L.C., & Arce Larrea, G.R. (2021). Outsourcing governance in Peru's integrated water resources management. *Land Use Policy*, *101*, 105105.

Poursanidis, D., Traganos, D., Chrysoulakis, N., & Reinartz, P. (2019). Cubesats Allow High Spatiotemporal Estimates of Satellite-Derived Bathymetry. *Remote Sensing*, *11*, 1299.

Qayyum, N., Ghuffar, S., Ahmad, H., Yousaf, A., & Shahid, I. (2020). Glacial Lakes Mapping Using Multi Satellite PlanetScope Imagery and Deep Learning. *ISPRS International Journal of Geo-Information, 9,* 560.

Renosh, P.R., Doxaran, D., Keukelaere, L. de, & Gossn, J.I. (2020). Evaluation of Atmospheric Correction Algorithms for Sentinel-2-MSI and Sentinel-3-OLCI in Highly Turbid Estuarine Waters. *Remote Sensing, 12,* 1285.

Rodbell, D.T., Delman, E.M., Abbott, M.B., Besonen, M.T., & Tapia, P.M. (2014). The heavy metal contamination of Lake Junín National Reserve, Peru: An unintended consequence of the juxtaposition of hydroelectricity and mining. *GSA Today*, 4–10.

Romero-Mariscal, G., Garcia-Chevesich, P.A., Morales-Paredes, L., Arenazas-Rodriguez, A., Ticona-Quea, J., Vanzin, G., & Sharp, J.O. (2023). Peruvian Wetlands: National Survey, Diagnosis, and Further Steps toward Their Protection. *Sustainability, 15,* 8255.

Roy, D.P., Huang, H., Houborg, R., & Martins, V.S. (2021). A global analysis of the temporal availability of PlanetScope high spatial resolution multi-spectral imagery. *Remote Sensing of Environment*, *264*, 112586.

Roy, D.P., Zhang, H.K., Ju, J., Gomez-Dans, J.L., Lewis, P.E., Schaaf, C.B., Sun, Q., Li, J., Huang, H., & Kovalskyy, V. (2016). A general method to normalize Landsat reflectance data to nadir BRDF adjusted reflectance. *Remote Sensing of Environment*, *176*, 255–271.

Saunier, & Cocevar (2022). Technical Note on Quality Assessment for SuperDove. EDAP.

Schläpfer, D., Hueni, A., & Richter, R. (2018). Cast Shadow Detection to Quantify the Aerosol Optical Thickness for Atmospheric Correction of High Spatial Resolution Optical Imagery. *Remote Sensing*, *10*, 200.

Schmid, S. (2024). Bathymetrie im Flachwasser mittles optischer Modellierung. Master Thesis Universität Eichstätt.

Schnalzger, K. (2017). Spektrale Datenbank für den Untergrund der Ostsee sowie Einfluss auf die Bestimmung der Wassertiefe. *Master Thesis University of Augsburg,*

Shi, H., & Xiao, Z. (2019). Updates of the 6S Radiative Transfer Model: A Case Study of 6S+Prosail. In *IGARSS 2019 - 2019 IEEE International Geoscience and Remote Sensing Symposium:* IEEE.

Shybanov, E., Papkova, A., Korchemkina, E., & Suslin, V. (2023). Blue Color Indices as a Reference for Remote Sensing of Black Sea Water. *Remote Sensing*, *15,* 3658.

Song, Q., Ma, C., Liu, J., Wang, X., Huang, Y., Lin, G., & Li, Z. (2022). Time Series Analysis-Based Long-Term Onboard Radiometric Calibration Coefficient Correction and Validation for the HY-1C Satellite Calibration Spectrometer. *Remote Sensing*, *14,* 4811.

Sunar, F., Dervisoglu, A., Yagmur, N., Aslan, E., & Ozguven, M. (2023). Analyzing the retrieval accuracy of optically active water components from satellite data under varying image resolutions. *The International Archives of the Photogrammetry, Remote Sensing and Spatial Information Sciences, XLVIII-M-1-2023*, 595–600.

Trishchenko, A., Cihlar, J., & Li, Z. (2002). *Effects of spectral response function on surface reflectance and NDVI measured with moderate resolution satellite sensors:* Natural Resources Canada/CMSS/Information Management.

Tu, Y.-H., Johansen, K., Aragon, B., El Hajj, M.M., & McCabe, M.F. (2022). The radiometric accuracy of the 8-band multi-spectral surface reflectance from the planet SuperDove constellation. *International Journal of Applied Earth Observation and Geoinformation, 114*, 103035.

van An, N., Quang, N.H., Son, T.P.H., & An, T.T. (2023). High-resolution benthic habitat mapping from machine learning on PlanetScope imagery and ICESat-2 data. *Geocarto International, 38*.

Vanhellemont, Q. (2019a). Adaptation of the dark spectrum fitting atmospheric correction for aquatic applications of the Landsat and Sentinel-2 archives. *Remote Sensing of Environment*, *225*, 175–192.

Vanhellemont, Q. (2019b). Daily metre-scale mapping of water turbidity using CubeSat imagery. *Optics Express*, *27*, A1372-A1399.

Vanhellemont, Q. (2020). Sensitivity analysis of the dark spectrum fitting atmospheric correction for metre- and decametre-scale satellite imagery using autonomous hyperspectral radiometry. *Optics Express*, *28*, 29948–29965.

Vanhellemont, Q. (2023). Evaluation of eight band SuperDove imagery for aquatic applications. *Optics express*, *31*, 13851–13874.

Vanhellemont, Q., & Ruddick, K. (2021). Atmospheric correction of Sentinel-3/OLCI data for mapping of suspended particulate matter and chlorophyll-a concentration in Belgian turbid coastal waters. *Remote Sensing of Environment*, *256*, 112284.

Veettil, & Kamp (2019). Global Disappearance of Tropical Mountain Glaciers: Observations, Causes, and Challenges. *Geosciences*, *9*, 196.

Wang, D., Ma, R., Xue, K., & Loiselle, S. (2019). The Assessment of Landsat-8 OLI Atmospheric Correction Algorithms for Inland Waters. *Remote Sensing, 11*, 169.

Wang, M., & Bailey, S.W. (2001). Correction of Sun glint Contamination on the SeaWiFS Ocean and Atmosphere Products. *Applied optics*, *40*, 4790–4798.

Warren, M.A., Simis, S.G.H., & Selmes, N. (2021). Complementary water quality observations from high and medium resolution Sentinel sensors by aligning chlorophyll-a and turbidity algorithms. *Remote Sensing of Environment*, *265*, 112651.

Wicaksono, P., Harahap, S.D., Hafizt, M., Maishella, A., & Yuwono, D.M. (2023). Seagrass ecosystem biodiversity mapping in part of Rote Island using multi-generation PlanetScope imagery. *Carbon Footprints*, *2*.

Wicaksono, P., & Lazuardi, W. (2021). Assessment of PlanetScope images for benthic habitat and seagrass species mapping in a complex optically shallow water environment. In *Fine Resolution Remote Sensing of Species in Terrestrial and Coastal Ecosystems* (pp. 143–169): Routledge.

Wood, J.L., Harrison, S., Wilson, R., Emmer, A., Yarleque, C., Glasser, N.F., Torres, J.C., Caballero, A., Araujo, J., Bennett, G.L., Diaz-Moreno, A., Garay, D., Jara, H., Poma, C., Reynolds, J.M., Riveros, C.A., Romero, E., Shannon, S., Tinoco, T., Turpo, E., & Villafane, H. (2021). Contemporary glacial lakes in the Peruvian Andes. *Global and Planetary Change*, *204*, 103574.

Yang, H., Kong, J., Hu, H., Du, Y., Gao, M., & Chen, F. (2022). A Review of Remote Sensing for Water Quality Retrieval: Progress and Challenges. *Remote Sensing*, *14*, 1770.

Yoon, B., & Choi, J. (2018). Analysis of Land Cover Changes Based on Classification Result Using PlanetScope Satellite Imagery. *Korean Journal of Remote Sensing*, *34*, 671–680.

Zubieta, R., Saavedra, M., Silva, Y., & Giráldez, L. (2017). Spatial analysis and temporal trends of daily precipitation concentration in the Mantaro River basin: central Andes of Peru. *Stochastic Environmental Research and Risk Assessment*, *31*, 1305–1318.

I hereby confirm that I have written the accompanying thesis by myself, without contributions from any sources other than those cited in the text and acknowledgements. This applies also to all graphics, drawings, maps and images included in the thesis.

Munich, 22.01.2024

Klotz P